# Finite element analysis of nanoindentation across bone interfaces and effects on the measured mechanical properties

**Auteur :** Qalaj, Puhia
**Promoteur(s) :** Ruffoni, Davide
**Faculté :** Faculté des Sciences appliquées
**Diplôme :** Master en ingénieur civil biomédical, à finalité spécialisée
**Année académique :** 2023-2024
**URI/URL :** http://hdl.handle.net/2268.2/20434

UNIVERSITY OF LIEGE
FACULTY OF APPLIED SCIENCES

# FINITE ELEMENT ANALYSIS OF NANOINDENTATION ACROSS BONE INTERFACES AND EFFECTS ON THE MEASURED MECHANICAL PROPERTIES

MASTER THESIS CONDUCTED BY

**PUHIA QALAJ**

WITH THE AIM OF OBTAINING THE DEGREE OF MASTER

IN BIOMEDICAL ENGINEERING

**Supervisor:**
DAVIDE RUFFONI

**PhD Student supervisor:**
ASTRID CANTAMESSA

**Academic year 2023-2024**

# Abstract

The microscopic structure of cortical bone reveals a complex architecture composed of osteons that contributes to bone fracture resistance. Osteons are formed from concentric lamellae that protect blood vessels at the center. Osteons are bordered by a tiny layer called cement line. Biologically, the cement lines are more mineralized than the surrounding bone and rich in osteopontin, a non collagenous protein. Their thickness varies between 1 and 5 $\mu m$ and they appear during the remodeling of bone tissue, separating the new bone from the old. These thin structures play a predominant role in biomechanics by effectively dissipating energy, by deviating or stopping microcracks, thus increasing the bone's resistance to fracture. Despite their importance, the mechanical behavior of cement lines remains poorly understood.

Local mechanical properties of cement line can be investigated by experimental techniques such as nanoindentation. However, the interpretation of the nanoindentation results is challenging as the cement lines are surrounded by osteon and interstitial bone, and they are very thin. Nanoindentation techniques face experimental limitations due to the size of the probed surface, which may be larger than the extremely fine dimension of the cement lines. Therefore, simulations can be used to better understand indentation results. The main objective of this master's thesis is to explore these local mechanical properties at bone interfaces through nanoindentation simulations conducted by the finite element method. This study determines the impact of the bone internal interfaces on local mechanical responses, evaluating the variability of indentation measurements induced by the positioning of the indenter, and thus proposes recommendations for supporting a better interpretation of experimental data.

Initially, pilot tests were conducted using the ANSYS Workbench software, where the model size, mesh sensitivity, and other simulation parameters were examined. The comparison of the results from two-dimensional and three-dimensional simulations showed an underestimation of measurements in two-dimensional modeling. Keeping this in mind, 2D models could still be used to perform parametric studies, especially for comparing relative properties and not absolute values.

The thesis was structured in two main phases. Initially, the material properties of 3 bone regions of different mineral content and age were analyzed. A spatial resolved analysis was performed, and it demonstrated a significant local influence of bone interfaces, causing substantial deviations in the measured tissue modulus with respect to the nominal value for a position in the middle of the cement line, with this deviation increasing as the indenter approached interfaces with surrounding tissues, thus highlighting the importance of the placement of the indenter tip within the cement line. Subsequently, the inclination of these bone interfaces was explored to assess its impact on the measured mechanical behavior. This confirmed that the sample sectioning process is of great importance in the reliability of the results.

In conclusion, thin bone interfaces have shown a significant influence on the mechanical properties that can be measured experimentally, suggesting several improvements in data interpretation. One possible improvement is the use of backscattered electron imaging post-nanoindentation to determine the exact position of the indents and to consider only those falling in the middle of the cement line, hence reducing the influence of surrounding tissues. This study has also opened new research perspectives, including the exploration of the influence of porosity, the study of surface roughness induced by polishing, and the direction of collagen fibers.

# Acknowledgments

This work was an enriching experience, immersing me in research for the first time. I discovered what it meant to start with a simple idea and end up with a multitude of questions, giving me the desire to explore further. I was lucky to be surrounded throughout my work, which would not have been possible without the invaluable help of all the people who accompanied me, to whom I would like to express my heartfelt thanks.

First, I would like to express my sincere gratitude to my supervisor, Professor Davide Ruffoni, for his warm welcome to his team, his patience, and his advice. I would like to thank him for all the time he devoted to me, and also for his contagious passion for his field, which was very inspiring and kept me motivated. His kind words at every meeting were a constant source of support.

Secondly, a big thank you to Astrid Cantamessa, PhD student, who suggested this subject to me and gave me her confidence. From the start, I did not hesitate to turn to her, and I am delighted with my choice. I sincerely thank her for always being there for me, for always having the right words to reassure and motivate me at every stage. Her kindness, attentive listening, and support made all the difference to my confidence in my work and the progress I made in my research. I am grateful for everything she has given me.

I would also like to thank the entire MBBM lab team for their help, advice and constant kindness. Thank you so much for welcoming me so warmly.

During these five years of study I have met exceptional people who gave me a lot both professionally and personally. I would like to sincerely thank my friends, whom I first met in project groups and who became true friends: Margaux, Kawthar, Hülya and Lena. Their support and all the positivity they gave me have enriched my life, and I am very grateful for that.

I would like to thank my best friends Rahma and Kasseye, who have always supported me, as well as Lo, who has always been there to push me to do my best.

To my family, my parents, and my little sister, who are my first source of motivation. Thanks to you, I have been able to continue my studies, and I am eternally grateful for your love and support at every stage of my life.

# Contents

# Notations

| | | |
|---|---|---|
| $P$ | load | N |
| $h$ | displacement | m |
| $E$ | Young's modulus | Pa |
| $\nu$ | Poisson's ratio | - |
| $P_{max}$ | maximum load | N |
| $R_{\text{tip}}$ | radius tip | m |
| $h_t$ | total penetration depth | m |
| $h_f$ | permanent penetration depth | m |
| $A_c$ | contact area | m$^2$ |
| $R_c$ | contact radius | m |
| $h_c$ | contact penetration depth | m |
| $S$ | stiffness of the contact | N/m |
| $E_r$ | effective Young's modulus | Pa |
| $E_{\text{indenter}}$ | Young's modulus of the indenter | Pa |
| $\nu_{\text{indenter}}$ | Poisson's ratio of the indenter | - |
| $E_{\text{sample}}$ | Young's modulus of the tested sample | Pa |
| $\nu_{\text{sample}}$ | Poisson's ratio of the tested sample | - |
| $b$ | half-length of the contact zone between 2 cylinders | m |
| $R_{eq}$ | reduced radius | m |
| $R_1$ | radius of the bottom cylinder | m |
| $R_2$ | radius of the top cylinder | m |
| $L$ | length of the cylinder | m |

# Abbreviations

| | |
|---|---|
| FEM | Finite Element Methods |
| CL | Cement Line |
| 2D | Two-Dimensional |
| 3D | Three-Dimensional |
| BEI | Backscattered Electron Imaging |
| IB | Interstitial Bone |
| OB | Osteonal Bone |
| DOF | Degrees Of Freedom |

# Introduction

Bone, this captivating biological material, reveals a complex architecture that spans from macroscopic to nanoscopic scales. At the heart of this fascinating structure is the cortical bone composed of osteons, with an architecture comparable to fortresses, sheltering the blood vessels essential to the bone [1]. On a finer scale, lamellae arranged in concentric circles strengthen the osteons [2]. Moreover, collagen fibers embedded in a more flexible matrix confer the mechanical resistance necessary to meet mechanical demands [3] [4]. The capabilities of bone do not stop there; it is also distinguished by its ability to remodel, revealing fine structures such as the cement line (CL), bordering the osteons and which not only protects but strengthens the osteons [5] [6]. This feature offers added value compared to materials used in engineering, inspiring biomedical engineering for the development of new approaches mimicking the remarkable properties that bone provides.

Bone interfaces play an important role in determining the mechanical properties of bone structures. Among these interfaces, the CLs, tiny layers measuring between $1 - 5 \ \mu m$, are distinguished from adjacent regions by their composition. From a biological perspective, these interfaces appear as boundaries between newly formed bone and older bone [7]. They are more mineralized than the surrounding bone, rich in osteopontin, a non collagenous protein, and are widely present in the bone structure [8] [9][10][11]. From a biomechanical perspective, research has highlighted their key role in the efficient dissipation of energy, acting as barriers that can deviate or even stop the propagation of microcracks, preventing their penetration into the osteons and contributing to increase the bone's resistance to fracture. Despite their importance, mechanical properties of the CLs remain poorly understood [12] [13] [14].

Local mechanical properties of the CL can be evaluated by nanoindentation experimentally. Although nanoindentation techniques provide nanoscopic resolution, experimental limitations are encountered, notably because the surface probed by the indentation which may be larger than the size of the CL itself. In this master's thesis, the goal is to characterize these local mechanical properties at the internal bone interfaces, between the CL and the osteon or interstitial bone (IB), using simulated nanoindentation through the finite element method (FEM). This study allows for the assessment of the impact of bone internal interfaces on mechanical responses on the variability caused by the position of the indent, and offers suggestions for better interpretation of experimental results.

The first chapter is dedicated to the structure and function of bone, with a particular focus on cortical bone and the CL. It also includes a review of the literature on the nanoindentation technique in order to master the key concepts necessary for assessing the mechanical properties of bone internal interfaces.

The second chapter is dedicated to the description of the pilot tests that led to the design of an appropriate model for conducting the study. This chapter details the model used, the meshing, and other simulation parameters, where simulations were carried out using the ANSYS Workbench software.

The third chapter presents the results in three main parts. First, it offers a comparison between two-dimensional (2D) and three-dimensional (3D) simulations. Next, it details observations on the mechanical properties measured for different placements of the indenter along 3 bone regions close to the interfaces, where each bone tissue exhibit different material properties. Finally, a section is dedicated to evaluating the impact of the inclinations of the bone interfaces

on the local mechanical behavior.

In the final chapter, a discussion of the results obtained on the bone structure from the previous chapter is deepened. An exploration of the limitations encountered during the study is also presented, along with suggestions of improvements in experimental results interpretations and potential future research.

# Chapter 1

# Background

The aim of this chapter is to give a detailed overview of the structure and function of bone, focusing on cortical bone and the CL, which are the central elements of this master's thesis. This is followed by an in-depth review of the nanoindentation literature, providing an understanding of current theoretical models. Finally, the last section will introduce the main topic of this master's thesis.

## 1.1   Bones

### 1.1.1   Functions

The musculoskeletal system is multifunctional. It has 4 main functions, with the first 2 as biological and the following pair as mechanical function.

i. **Hematopoiesis**

Hematopoiesis can be defined as a process of formation of red blood cells in a specific region called red bone marrow [15]. In trabecular bones, located in the epiphysis of long bones, there are a lot of pores which are filled with red bone marrow, playing a key role in the production of blood cells [2]. The outer shell of bone, known as cortical bone, contains an inner space called the medullary cavity in the diaphysis part, filled with yellow bone marrow, which serves as a fat storage system [5] [16]. These different parts are illustrated in Figure 1.
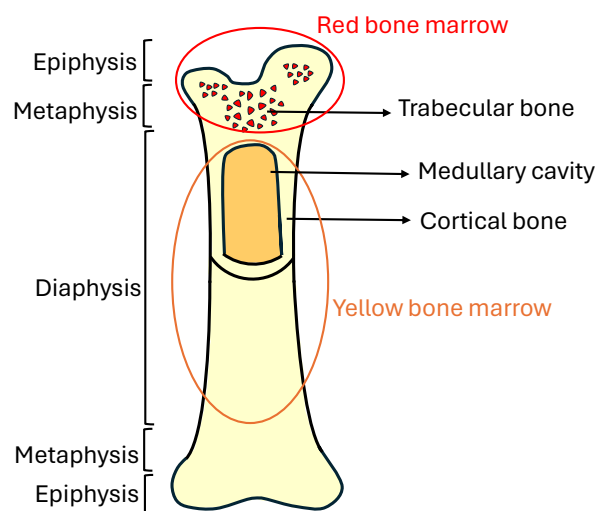


Figure 1: Schematic representation of anatomical structure of a long bone with its main components, including the red and yellow bone marrow, cortical and trabecular bone and also the sections of the bone, including the epiphysis, metaphysis, and diaphysis.

ii. **Mineral storage**

Bone is seen as a mineral reservoir, with higher calcium and phosphorous content. These minerals play an important role in metabolic functions and can be released into the blood-stream according to the body's needs [2]. In fact, $99\%$ of calcium is stored in the skeleton. The level of calcium in the blood can be regulated thanks to a remodeling process (see Section 1.1.4) [15] [5] [16].

iii. **Protection of vital organs**

Another function of skeletal bone is to protect vital organs such as the brain, lungs and spinal cord [15]. Bone is able to combine high energy absorption and low weight. As an example, the skull protects the brain by having a sandwich-like structure. It is composed of 2 external layers of cortical bones which are stiff, and inside it is trabecular bone that can be deformed [5] [16].

iv. **Support and motion**

The skeletal system has the ability to support the weight of the body. But also, the combination of joints, bones, and muscles provides motion. Bones and joints serve as anchor points for muscles, enabling them to generate movement [2] [5] [15] [16].

### 1.1.2   Shapes of bones

There are $3$ types of bones which lead to different biomechanical functions. The first one is long bones, like femur, which provides stability against bending and buckling. The second one is short bones, like vertebrae, which provides stability against compression. And the third one is plate-like bones, like the skull, which provides protection of vital organs like brain (see Figure 2) [17].
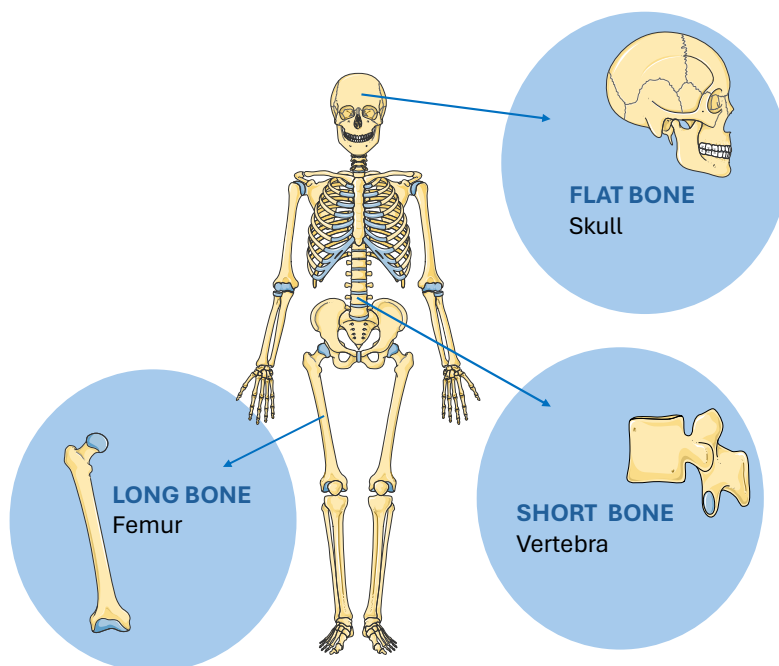


Figure 2: Schematic representation of $3$ different shapes of bones including long bone, short bone, and flat bone (adapted from [18]).

### 1.1.3 General form of long bones

The structure of long bones (see Figure 3) consists of 2 main parts, including diaphysis located in the middle part and the end of long bones in which trabecular bone, also called cancellous bone, is found. In this terminal region, there are epiphysis and metaphysis sections, which are separated by a line called growth plate. This specific region allows bone to grow. The growth plate is not mineralized, but is composed of cartilage. Once adulthood is reached, this growth plate is fused, gets mineralized and transformed into bone. The line can still be seen between the 2 regions [5] [19].

The bone surface is covered by periosteum, which is a layer of cells. When an impact or a fracture occurs on a bone, the pain is mainly felt due to the periosteum. Indeed, this layer is highly innervated [5] [19].

Bone is a highly vascularized tissue. Bones contain holes to accommodate blood vessels, and also cells. Since it is a tissue which carries a lot of load, bone evolves by finding many strategies to make these holes not dangerous from a mechanical point of view. Veins and arteries enter from the diaphysis and bring nutrients and remove waste product [5] [19].
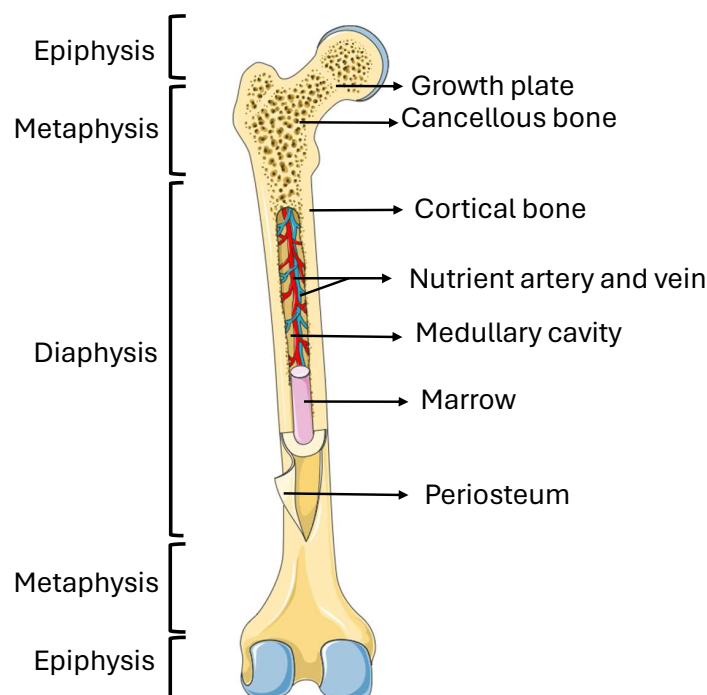


Figure 3: Schematic representation of the general form of long bones, labeling with its key components (adapted from [18]).

### 1.1.4 Biological process of bone remodeling

The bone remodeling process is defined as a continuous physiological process that renews old and damaged bone with new bone. Even if it does not avoid the presence of crack, it is able to prevent the propagation of cracks. Moreover, it maintains mineral homeostasis by controlling the level of ions [5] [20]. Remodeling has not the same meaning as modeling. The phenomenon of modeling is a process where the cells of bone tissue do not work in a coordinated manner, unlike the phenomenon of remodeling, where the cells are coordinated [6] [21].

There are 3 types of cells involved in the process of remodeling (see Figure 4). The first type is osteoclasts which come on the bone surface to release some acids, and eat collagen. By removing bone tissue, calcium ions stored within the bone are released into the blood. Thus maintain calcium homeostasis in the body. One signal for osteoclasts to release calcium is when blood calcium levels are low [2]. At the end, this resorption creates a space within bone. The presence of old or injured bone is a signal for osteoclasts to migrate to the bone surface [22] [23].

The second type of cell is osteoblasts, which are attracted to the spaces left by osteoclasts. One characteristic of remodeling is that the resorption and formation occur simultaneously in the same location. Osteoclasts and osteoblasts are closely interconnected, and there is a synchronization in the deposition of new bone tissue [16]. When osteoblasts reach the resorbed bone surface, they deposit collagen, initiating the mineralization process to form new bone [24]. Due to this continuous process of bone remodeling, this results in different content of minerals. In fact, thanks to X-rays, it is possible to see the degrees of calcification. A bone less mineralized will appear more transparent to X-rays than bone fully mineralized and which have completed their formation [22] [23] [25]. To lower elevated blood calcium levels, osteoblasts deposit calcium and phosphate ions, helping to regulate their concentration levels in the bloodstream [2].

The third type of cells is osteocytes, which act as strain sensors. This means that they are capable of sensing strains in the areas where bone remodeling is needed and send osteoclasts and osteoblasts to undertake this process. Some osteoblasts become trapped within the bone matrix and undergo a transformation in their phenotypes to become osteocytes. There are also the lining cells which sit on the surface of the bone [26]. Osteocytes and lining cells form an interconnected network that facilitates the exchange of information [22] [27].

Bone remodeling is mechanically controlled. In fact, load has an influence on the behavior of those cells. Bone has the ability to adapt to change in the loading environment. If there is an increase in loading condition, bone mass increases and bone architecture is reinforced. Whereas, if there is a decrease in loading condition, leads to a decrease of bone mass and weaken bone architecture [27].
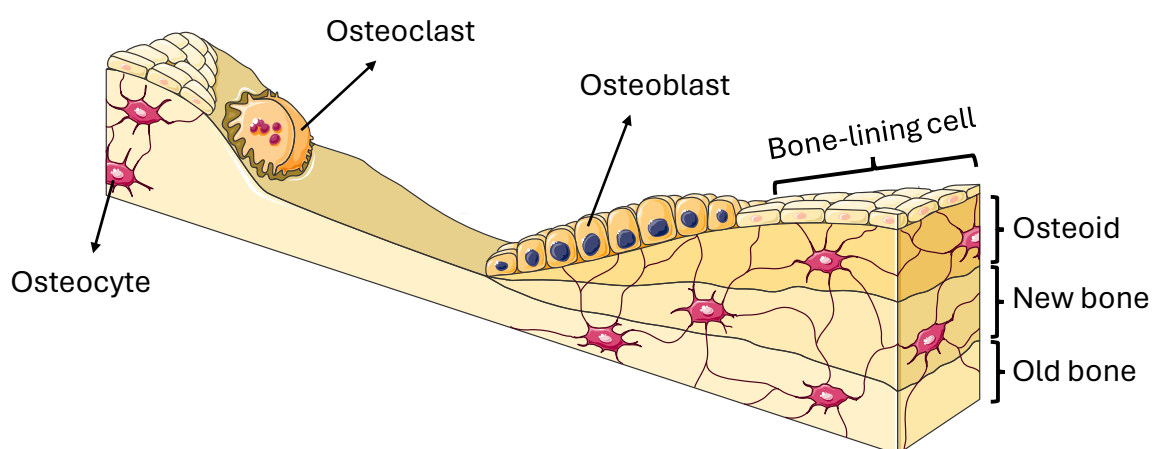


Figure 4: Schematic representation of bone remodeling (adapted from [18]).

### 1.1.5   Bone as hierarchical material

Bone is a hierarchical material (see Figure 5). In fact, it has multiple scales with different arrangements of material.

Within the subnanoscale level, below a few hundred nanometers, in terms of composition, bone is composed of an inorganic part which is the mineral part, an organic part which is the collagen protein and water with a role not clearly understood [3] [28].

The organic phase (about $30\%$ of the weight of bones) comprises collagen type I, III and IV, and non-collagenous protein. Collagen type I, forming around $85\%$ to $90\%$ of the bone's organic matrix, is the dominant protein in the body [2]. To achieve a stable configuration, collagen molecules form a triple alpha-helix structure. Collagen molecules synthesized by osteoblasts, when they are released in the extracellular space, are able to self-assemble. They align in a staggered fashion, leading to the formation of collagen fibrils at the nanometer length scale [3] [4] [29].

In terms of minerals (about $60\%$ of the weight of bones), bone is mainly composed of hydroxyapatite, $Ca_{10}(PO_4)_6(OH)_2$, in the form of tiny amorphous platelets deposited within the gaps of collagen molecules [30]. Then, these amorphous minerals undergo a transformation into crystals. This leads to the formation of mineralized collagen fibrils, which is the basic building block of bone [3] [28] [31].

The mineralized collagen fibrils assemble to form bundles, also named fibers. At the sub-microstructure, for 1-10 $\mu m$, these fibers arranged in a staggered planar manner to form different sheets called lamellae bone. Each plane is characterized by arrays of fibers [32].

Then, at the millimeter level, there is a distinction between 2 types of bone which are the cortical bone and trabecular bone. Cortical bone forms the walls of long bones, whereas the trabecular bone is located inside the end of long bones, which is highly porous. Cortical bone, known for its higher density, provides mechanical strength, while trabecular bone is characterized by its honey-comb structure [2]. These 2 types of bones differ in the microstructure level, from 10 to 500 $\mu m$ [28] [32].

The basic structural unit of cortical bone is the osteons. The cortical bone thickness is 10 $mm$. Therefore, due to this thick structure, bone builds this structure called osteons to bring nutrients to the cells. These osteons are concentric rings protecting blood vessels from the surrounding stresses (see Section 1.1.6). The remodeling process starts from their center [1].

Trabecular bone is a highly heterogeneous material, composed of different bone packets highlighting different content of minerals depending on the stage of bone mineralization. In contrast to cortical bone, there are no blood vessels inside trabecular bone because nutrients can diffuse easily due to the thin structure. In this type of bone, the remodeling process starts from the surface [33].

At the centimeter level, bone has different shapes (see Section 1.1.2).
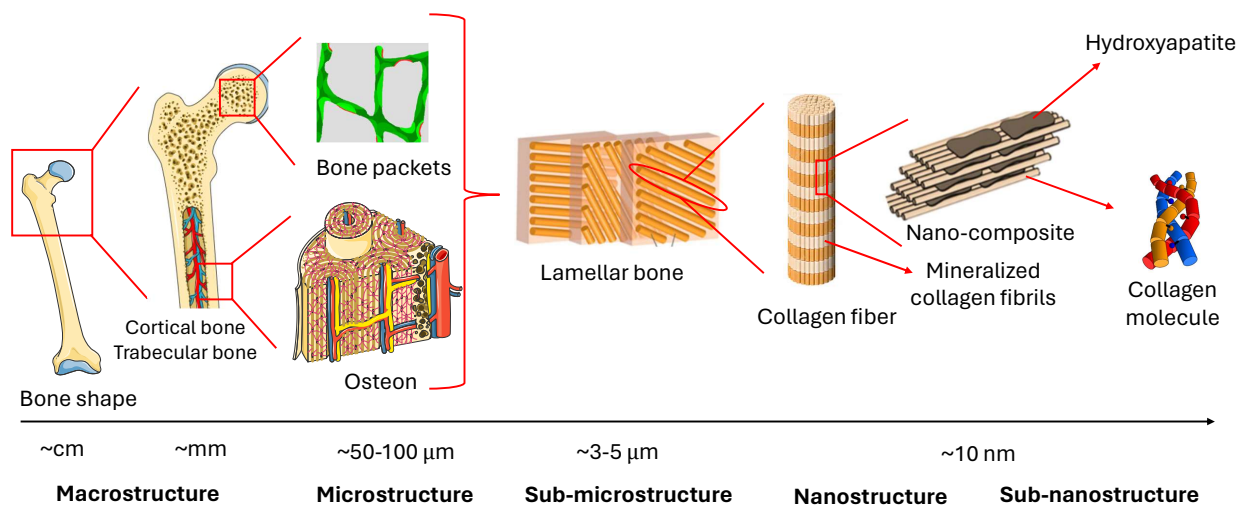
Figure 5: Schematic representation of the hierarchical structure of the bone (pictures taken from [18] [34] [35]).

### 1.1.6 Structure of cortical bone

To understand the mechanical function of cortical bone, one must study its microscopic organization (see Figure 6).

Cortical bone is the type of bone with the lowest porosity and is characterized by its heterogeneity. It is important to distinguish primary bone, which is the bone present since birth and has not yet undergone remodeling, from secondary bone, which has already been remodeled. Therefore, primary osteons, which contain fewer concentric lamellae, are less developed than secondary osteons that have undergone thorough bone remodeling, containing more concentric lamellae [2].

Osteons are oriented longitudinally. There are no transversely oriented osteons. A typical osteon resembles a cylinder with $100$–$250$ $\mu m$ in diameter [1]. Osteonal bone consists of $10$-$15$ thin lamellae ($2$-$6$ $\mu m$) arranged in concentric cylinders surrounding a central Haversian canal, through which blood vessels pass [4]. Osteons serve to protect and build channels for blood vessels to bring nutrients to cells and remove waste [36]. Additionally, the Volkmann's canals, perpendicular to the osteons, perforate bone matrix to connect osteons together. To clearly distinguish between osteons, each one has a boundary known as a CL (see Section 1.1.9) [29].

Lamellar bones consist of parallel sheets which contain mineralized collagen fibrils. Within each lamella, collagen fibers run parallel to each other and are oriented at a predominant angle. However, there is a shift in the orientation of collagen fibers between adjacent lamellae [37].

This spiral arrangement of collagen fibrils within lamellae serves 2 main purposes. Firstly, by changing the angles of the fibers, it is possible to locally adjust the stiffness of the osteons. In regions requiring high rigidity, the fibers are oriented along the axis of the osteon, whereas in regions requiring flexibility, the fibers are inclined at a steeper angle. Secondly, because the collagen fibrils are stiff and brittle, the spiral arrangement allows for higher deformation, allowing the bone to absorb more energy. As cracks propagate through osteons, they undergo

twisting because of the changing of angle in each plane. As a result, this structural feature improves the bone's toughness [30].

Within cortical bone, there are lamellae located around the bone's perimeter that do not form osteons but form lamellar bone [29] [32].

Within the structure of an osteon, lacunae are cavities where osteocytes sit. Osteocytes have the ability to elongate and perforate the bone matrix, forming canaliculi. These osteocytes and lacunocanalicular network serve a dual purpose: firstly, to transport nutrients, and secondly, to connect osteocytes for communication. The presence of fluid within the canaliculi enables osteocytes to sense the mechanical strain, which makes bone highly responsive to any external stimuli [2] [38].

Various studies have performed tests to determine the stiffness in cortical bone. To provide specific values of the Young's modulus for human cortical bone in the longitudinal direction is approximately 26 GPa for the interstitial bone and about 22 GPa for the osteonal bone [29] [39].
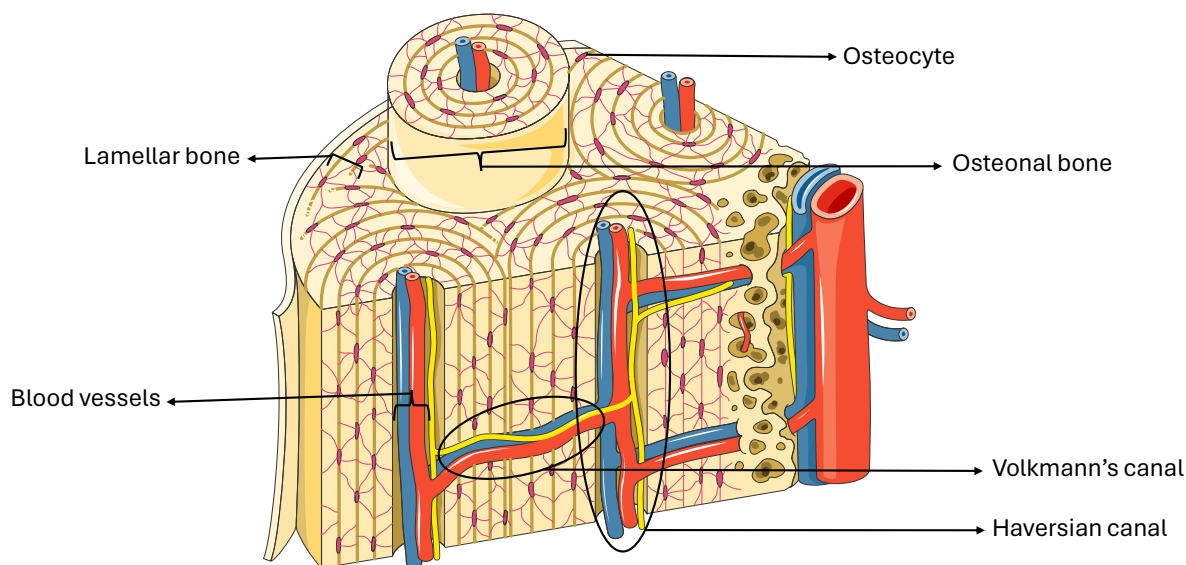


Figure 6: Schematic representation of a detailed cross-section view of cortical bone microarchitecture (adapted from [18]).

### 1.1.7 Osteonal bone remodelling

Figure 7 illustrates the bone remodeling process in the specific case of osteon formation. The remodeling process is depicted through sequential steps from right to left, where each zone has its unique cellular activities.

1. Resorption region:
   This region is dominated by the osteoclasts, which are multinucleated cells originating from blood vessels. These cells cluster together and secrete acid to resorb minerals and enzymes to degrade collagen. These cells create a cavity by resorbing the bone matrix. The resorption region moves at a rate of approximately $40 \ \mu m$/day, a rate which characterizes the speed of bone degradation.

2. Reversal region:
   This region is located between the osteoclasts and refilling regions, characterized as a transitional zone that serves as an interface between bone resorption and formation.

3. Refilling region:
   In this region, osteoblasts coordinate with each other to deposit new bone matrix, particularly by forming structured layers called lamellae. Osteoblasts ensure that the orientations of the deposited bone change every $2 \ \mu m$. Moreover, some osteoblasts not only fill the cavities left by the osteoclasts, but also become trapped in the bone matrix and differentiate into osteocytes.

4. Completed osteon:
   The completed osteon is shown on the left, featuring the central Haversian canal surrounded by new bone tissue [40] [41] [42].
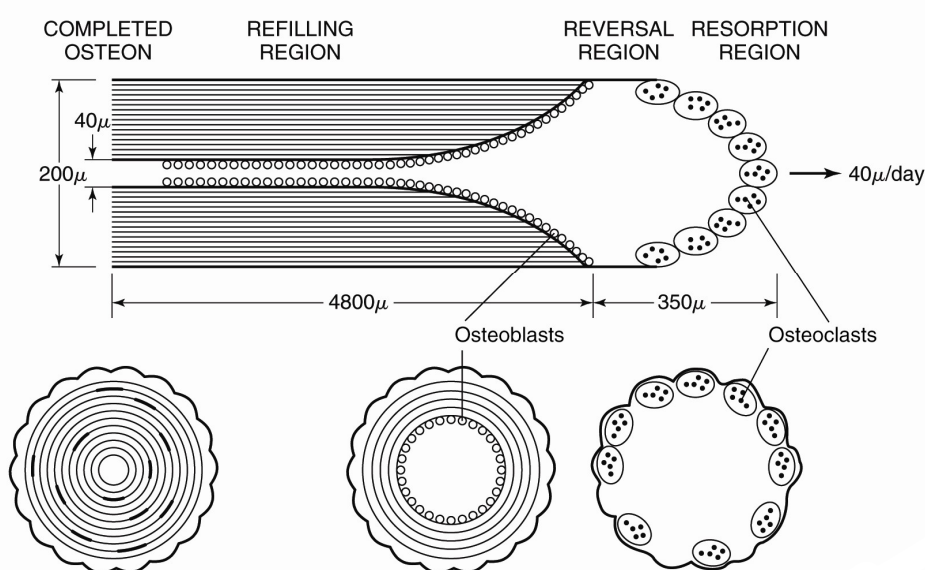


Figure 7: Schematic representation of the bone remodeling process in osteonal bone formation [34].

### 1.1.8 Mechanical properties of cortical bone

To determine the mechanical properties of cortical bone, tests are performed on bone samples subjected to uniaxial testing, until failure occurs. In Figure 8, 2 curves are depicted. The dotted red curve represents a longitudinal sample, while the full-blue line represents a transverse sample. The sample configurations are represented on the right [43].

Regarding the curve for the longitudinal sample, it exhibits a more ductile phase under tension. Additionally, it has higher mechanical properties compared to the transverse sample. The ultimate strain is greater under tension, which means that the ability of bones to deform is much higher in tension [1] [43].

Concerning the curve for the transverse sample, it displays greater ductility in compression. However, it is the least resilient as it is weaker. It has no plastic region but only an elastic region, before it breaks into a brittle manner [1] [43].

Cortical bone is assumed to be transversally isotropic. Osteons in cortical bone are arranged to confer homogeneity of mechanical properties in the transverse plane, as osteon distribution is more or less uniformly spread around the central axis of the bone. However, osteons are aligned in the longitudinal direction, resulting in a difference in mechanical properties compared to the transverse direction. This difference justifies the classification of cortical bone as a transversely isotropic material [1] [43] [44].

These 2 curves show asymmetry. It also shows anisotropy, where the properties vary depending on the direction. The yield strains are similar, indicating independence from direction and implying isotropy in this regard. Concerning Young's modulus, the values are quite different: for the longitudinal sample, it is $E_{\text{longitudinal}} = 17$ GPa, while for the transverse sample, it is $E_{\text{transversal}} = 10$ GPa. Additionally, cortical bone shows greater strength in compression than in tension, which makes sense because it is the main loading expected by the bones [1].

In terms of strength anisotropy, cortical bones are much stronger longitudinally than transversally. This discrepancy is a result of the way cracks behave within the bone. When a crack propagates transversally, it encounters osteons, which deflect its path, causing the crack to propagate around osteons. On the other hand, when a crack propagates longitudinally, it travels between osteons, encountering less resistance, and it results in a straight crack. Therefore, bone is anisotropic in the way it breaks [30].
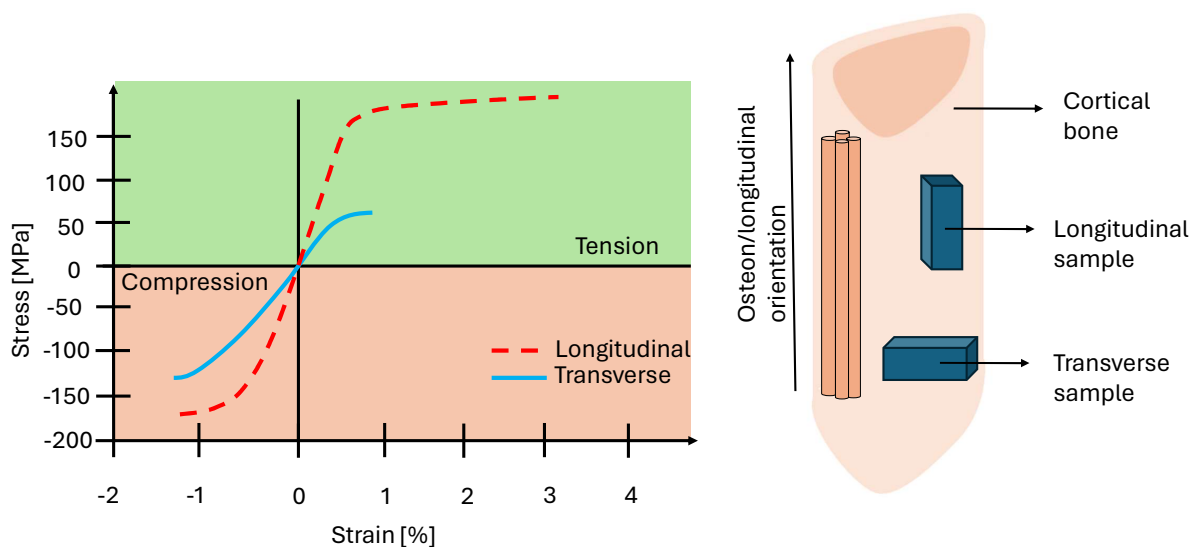


Figure 8: Stress-strain behavior of adult human cortical bone samples (inspired from [34]).

In conclusion, the cortical bone in terms of mechanical properties shows an anisotropic behavior [29].

### 1.1.9 Cement line

In bone structure, mechanical properties are influenced by various factors, including interfaces that play an important role. Within these interfaces are CLs, thin layers approximately 1 to 5 $\mu m$ thick. Their role is to separate secondary osteons from the surrounding IB or other secondary osteons [45]. CLs are present in different locations within the bone structure. Indeed, they are also found in trabecular bone around bone bundles [46]. They act as boundaries between

newly formed bone and older bone, thus separating tissues with different mineral contents (see Figure 9) [7].
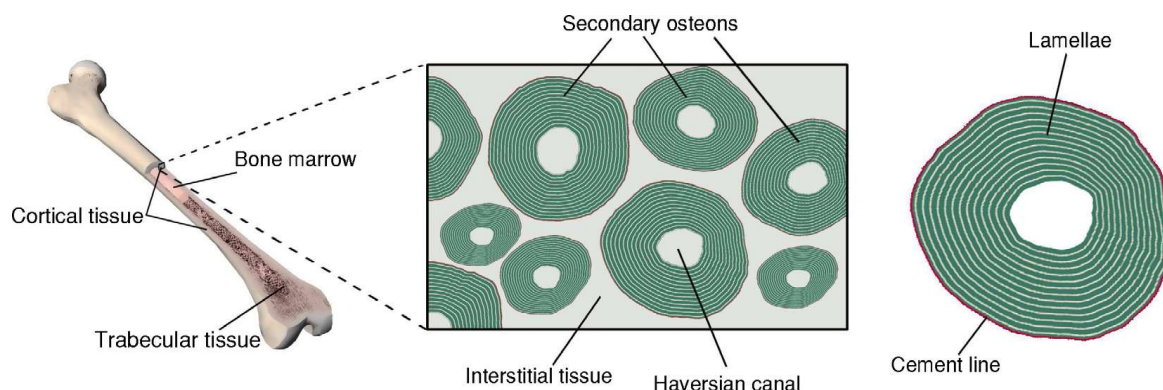


Figure 9: Schematic representation of a long bone on the left, a cross-section of cortical bone tissue in the middle, and a zoomed-in view of a typical secondary osteon on the right, consisting of concentric lamellae around the Haversian canals, with the CL marking the boundary of the osteons [47].

The composition and mechanical properties of CLs are the subjects of ongoing research.

► **COMPOSITION**

The exact composition of CLs is debated in the literature and therefore remains uncertain. However, studying this composition is important for understanding and analyzing their mechanical properties.

Regarding the composition of CLs, initial literature showed contradictions. Early studies indicated differences in mineral concentration in CLs compared to the surrounding bone tissue, showing both lower [48] and higher [10] mineral concentrations compared to adjacent bones. However, more recent work using synchrotron tomography and backscattered electron imaging (BEI) has observed a tendency for higher mineral concentrations than in corresponding osteons [7][11]. Furthermore, it has been found that this gap in mineral composition between the 2 tissues (CLs and adjacent bone tissues) tends to decrease with age[8].

► **BIOMECHANICS**

Different research has demonstrated that there is an influence of CLs on the mechanical properties of bone. Bright-field and fluorescence microscopy, as well as synchrotron radiation micro-computed tomography on cortical bone, have shown that the density of microcracks is greater in IB than in osteons [9] [49]. Consequently, this microscopic region plays an important role in effectively dissipating energy during crack propagation, thereby improving the fracture properties of cortical bone. By dissipating energy, it does not only enhance the bone's resistance to fracture but also serves as a barrier, deflecting or stopping the progression of cracks, minimizing the force that drives crack progression and preventing them from penetrating into the osteons [7] [12] [13] [14]. This is seen as a protective mechanism concerning both the integrity of the osteon and that of the blood vessels placed in the central Havers canal. CLs are therefore important for the mechanical properties of the bone [50].

Although important, the characteristics of CLs are among the least understood elements in bone [51]. Indeed, information regarding their mechanical properties is very poorly defined in

the literature, both in terms of their stiffness, i.e., their resistance to elastic deformation, and their hardness, i.e., their resistance to irreversible deformations. However, enriching the understanding of some of these aspects would be beneficial for evaluating their role in reinforcing osteonal and trabecular bones against fractures [52] [53].

▶ CURRENT WORK

As previously explained, studies have shown that CLs are present to deviate or stop the propagation of microcracks. The hypothesis is that nature has evolved to develop CLs to protect the osteons. However, their mechanical properties have been little studied. During her research, Astrid Cantamessa studied CLs to enhance understanding by characterizing the mechanical properties of the CLs and the surrounding bone tissue to assess whether the stiffness of the CL was softer or stiffer than the corresponding osteon. For these experimental tests, nanoindentation was used, a technique that measures the Young's modulus and hardness of materials. This technique is explained in more detail in Section 1.2. A grid of indents spaced 1 $\mu m$ apart was used, penetrating to 150 $nm$ with a force of 500 $\mu N$. 2 post-nanoindentation techniques were used: high-resolution secondary electron imaging to identify the imprints and backscatter electron imaging to see where the imprints are located in the CL. Thus, as illustrated in Figure 10, the results were able to determine the effective Young's modulus ($E_r$) measured in the region of the CL using a 2D map, indicating that the CL is 15% stiffer than its corresponding osteon [54].
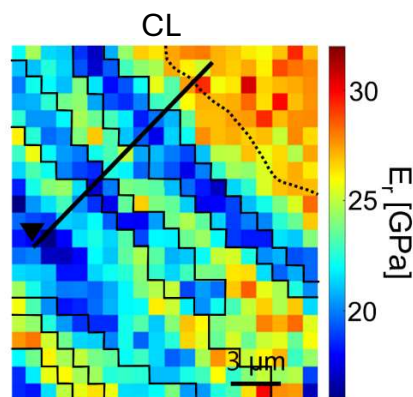


Figure 10: 2D map of the effetive Young's modulus with CL indicated by a dotted line [54].

## 1.2 Nanoindentation

### 1.2.1 Introduction to nanoindentation

Nanoindentation is a tool used in a wide range of applications, with a particular focus on biology and biomedicine [55]. It allows evaluating the mechanical properties of biological materials, particularly bone. It allows obtaining parameters as the hardness and elastic modulus of biological materials thanks to well-developed theoretical models [56] [57]. This technique provides insights to understand the relationship between bone structure and mechanics, and can be utilized as a diagnostic tool [58]. Nanoindentation is a popular technique thanks to its versatility, as it is suitable for use in a variety of applications, but also thanks to its ease of use; this means that no advanced knowledge is required to use it. Moreover, nanoindentation has high throughput potential. In fact, it is capable of obtaining results very quickly. Additionally, compared to more macroscopic techniques, nanoindentation allows for obtaining information on mechanical properties in a very localized and precise manner. This is why this technique is chosen to evaluate the mechanical properties of bone structures at the micro and nanoscale [59].

### 1.2.2 Nanoindentation fundamentals

During a typical nanoindentation test, the indenter, usually made of a hard material, penetrates into a softer material [59]. The nanoindentation system drives the indenter tip into the material to measure 2 parameters: first, the force applied by the tip on the sample, then the depth of penetration. These 2 parameters are recorded throughout the experiment as the indenter progressively penetrates [55]. Thanks to this, it is possible to evaluate, for example, the material's hardness. Indeed, this measurement is easily obtained as it is defined as the resistance of the material to penetration, directly correlated with the intensity of the force required to press the indenter into the material [60].
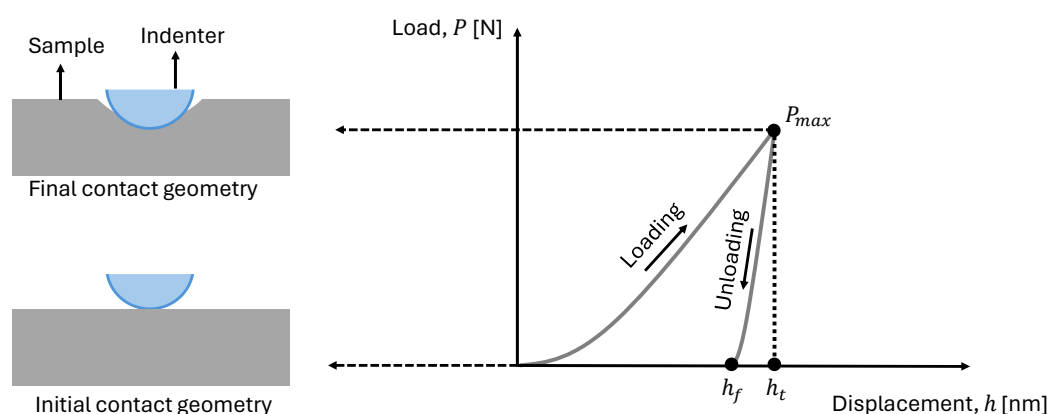


Figure 11: Schematic representation of a typical load-displacement nanoindentation curve with a spherical indenter, where initial and final contact geometries are also represented (inspired from [61]).

Nanoindentation measurements provide load ($P$) versus displacement ($h$) curves, as illustrated in Figure 11. This data depict the loading and unloading phases during penetration. During loading, the tip penetrates the material to leave an imprint. 2 types of deformation may occur:

firstly, elastic deformations which are reversible, allowing the material to return to its original shape when unloaded; secondly, plastic deformations, which are permanent deformations and the material is unable to return to its original shape when unloaded. When the indenter is removed, the depth of permanent deformation is characterized by the parameter $h_f$, as shown in the figure. During unloading, the indenter tip is removed from the material. Elastic deformations are recovered and observed. Put differently, if the material undergoes permanent deformations, it will not recover and will remain in the material. Therefore, the material only has memory for its elastic deformations [55] [62].

### 1.2.3 Materials and equipment used

► NANOINDENTER DESCRIPTION

Figure 12(a) schematically represents the nanoindentation system, and Figure 12(b) illustrates a typical nanoindentation instrument available on the market. This system is composed of a magnet and a coil that generate the necessary force to insert the indenter into the sample (material under test). Subsequently, a displacement gauge is utilized. It is a capacitive system consisting of 3 plates, enabling precise measurement of the displacement caused by the indenter tip when it comes into contact with the sample. Support springs stabilize the vertical column, ensuring uniform force transmission. The indenter tip is the part that directly contacts the tested sample. This tip is made of a hard material, typically diamond, to achieve the most accurate penetration results possible. The $x - y - z$ table allows positioning the sample accurately beneath the tip along 3 axes: horizontal ($x$), horizontal orthogonal to $x$ ($y$), and vertical ($z$) [55] [63].
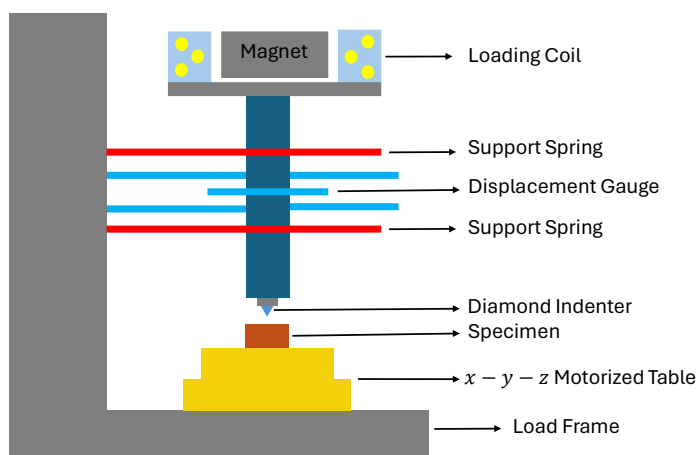


(a). Shematic representation of a typical nanoindation equipment (inspired from [55] [63]).

(b). Picture of nanoindentation tester, used for real testing at nanoscale [64].

Figure 12: Nanoindentation equipment.

► TIP TYPES AND THEIR INFLUENCE ON MEASUREMENTS

Nanoindentation can be used with different types of indenter. 4 different types of indenter geometry are illustrated in Figure 13. Generally, researchers often use spherical or pyramidal indenters to measure properties of materials.

Spherical (see Figure 13(a)) indenter is a type of indenter that is becoming increasingly popular, as it enables a gradual transition between the elastic and elastic-plastic phases. With spherical indenters, the advantage is manifested in more uniform stress fields than with pointed indenters. In addition, the elastic part of the stress-strain curves is larger, making it easier to follow the material's behavior in response to loading. In fact, spherical indenters induce a larger initial contact area than pointed indenters. As a result, the region undergoing elastic deformation will be larger, thanks to the more uniform pressure distribution. The spherical indenter therefore provides a better understanding of the elastic part of nanoindentation [59]. Conical (see Figure 13(b)) indenter is a geometry of tip often used in 2D numerical simulation studies as a substitute for Vickers and Berkovich indenters [65]. Vickers indenter (see Figure 13(c)) has a diamond-shaped tip with its opposing faces which have a semi-angle, denoted by $\theta$, equals to $68°$. This means that this indenter is inclined relative to a flat surface of a sample at an angle of $22°$, denoted by $\beta$. Vickers indenter is preferred for high-load testing because it offers more resistance. Vickers indenter is usually used for microindentation. Berkovich indenter (see Figure 13(d)) has a triangular pyramid shape. Berkovich's opposing faces generally have, for nanoindentation tests, a semi-angle equal to $65.27°$. In the case of the Berkovich indenter, the fact that it is based on a 3-sided base makes it easier to construct the pyramid's edges so that they all converge at a single point. Unlike Vickers, Berkovich has a finer tip, allowing for much more precise measurements. This means that the indentation produced by the Berkovich indenter will have a finer tip, resulting in a smaller contact area and potentially more accurate measurements. In the case of Vickers, the four edges do not ensure that they converge perfectly at a single point, but rather align along a line. As a result, the contact zone is larger with Vickers than with Berkovich. Consequently, the Berkovich indenter is used for smaller-scale testing for nanoindentation [55] [66].



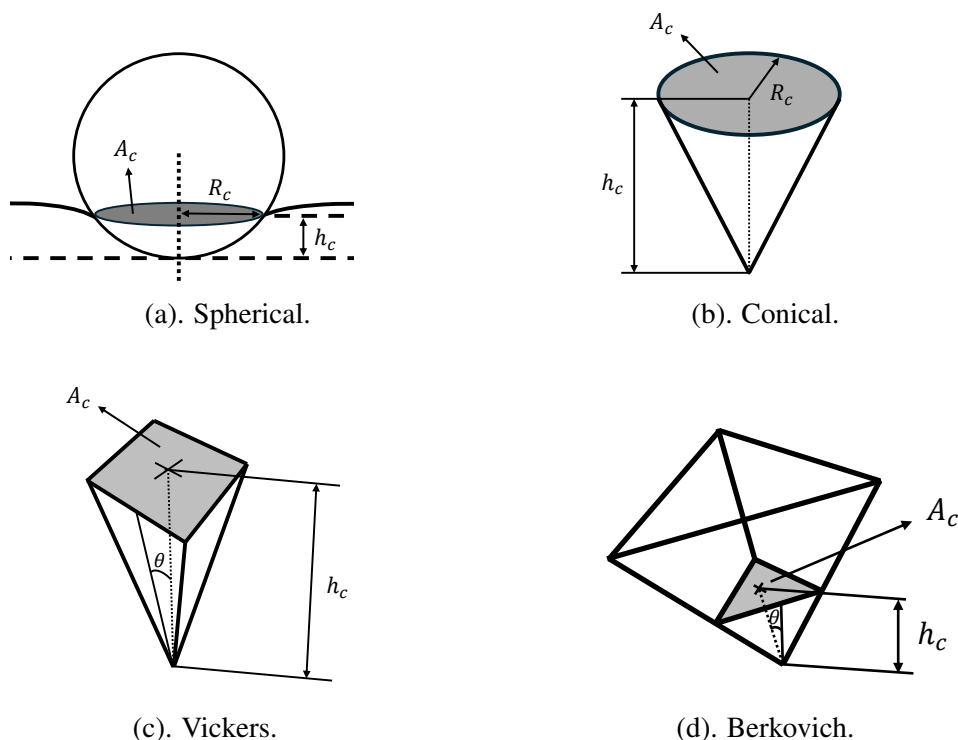(a). Spherical.

(b). Conical.

(c). Vickers.

(d). Berkovich.

Figure 13: Indenters geometry, where $A_c$, $R_c$, $h_c$ and $\theta$ are respectively the contact area, the contact radius, the contact penetration depth and the semi-angle (inspired from [66]).

Diamond is generally the preferred material for the indenter in nanoindentation tests. Diamond is chosen for its high hardness. However, it should not be overlooked that it is a brittle material. Typical Young's modulus and Poisson's ratio values used for nanoindentation are shown in Table 1 [67].

| Material | Young's modulus $E$ [GPa] | Poisson's ratio $\nu$ [-] |
|---|---|---|
| Diamond | 1140 | 0.07 |

Table 1: Material properties of the diamond indenter in typical nanoindentation tests [58] [68] [69].

### 1.2.4 Nanoindentation theory, models, and equations

Numerous methods have developed theoretical models to calculate the mechanical properties of materials tested during indentations. Hertz contact theory is an analytical approach that has played a fundamental role in measuring material hardness during nanoindentation tests. At the end of the 20th century, in 1992, the Oliver-Pharr method was proposed as an improvement for calculating hardness and Young's modulus.

▶ **OLIVER-PHARR**

The Oliver-Pharr method is a well-known and developed analytical approach in the field of nanoindentation [4]. It allows the determination of the effective indentation modulus and hardness of tested materials by extracting data obtained through loading and unloading cycles based on the force versus displacement curve during nanoindentation tests. This technique is adapted for evaluating the mechanical properties at small scales. The main improvement in this method is its enhanced capability to understand the elastic plastic behavior manifested in the material [70]. This method enables us to calculate the elastic properties of the material accurately based on established mathematical formulas.

The Oliver-Pharr method is based on a series of assumptions, which are as follows [58] [69] [70] [71]:

- The material is homogeneous, which means that the material's mechanical properties ($E$ and $\nu$) are identical throughout the part;

- The material is linearly elastic, which means that the material's yield point has not been reached, allowing us to remain within the material's linear elastic range;

- The material is isotropic, which means that the material's mechanical properties are identical in all directions;

- The material is incompressible, which means that the material does not change volume when subjected to load;

- During the unloading cycle, the material returns to its original shape without any residual plastic deformation. Therefore, the initial phase of unloading is assumed to be purely elastic during unloading and thus free from any inelastic phenomena such as a creep or plastic deformation;

- The pressure applied by the indenter causes a uniform depression around the contact area.

The Figure 14 shows an example of a loading and unloading curve, where $P$ represents the load and $h$ represents the displacement that the undeformed surface undergone. Moreover, in this figure, a line fits the slope in the initial phase of the unloading curve. This slope is the key parameter upon which the Oliver-Pharr method is based. In fact, this method does not require imaging techniques to measure the size of the indentation left by the indenter in order to calculate hardness. It is sufficient to rely on one loading and unloading cycle. By simplifying the way mechanical behavior is obtained, it has become one of the most used techniques for analyzing the mechanical properties of materials at the $\mu m$ and $nm$ scale, such as thin films. Initially, this method was exclusively applied to Berkovich indenters. Oliver and Pharr later discovered that the method could be adapted to any type of indenter, provided that the geometry is axisymmetric. Thus, this method can be considered quite general for axisymmetric indenters [72].

To apply this method, different important parameters must be measured: the maximum applied load, denoted $P_{max}$, the maximum displacement, denoted $h_t$, and the initial slope of the unloading curve, denoted $S = dP/dh$, named contact stiffness. A final important parameter shown in Figure 14 is $h_f$, corresponding to the depth of permanent penetration when the indenter is completely removed. It has been shown that the unloading curves are not exactly linear but slightly curved, and can be adjusted using a power-law type relationship. Generally, the upper $60\%$ of the unloading curve can be fitted by the Equation 1.1,

$$P = \alpha(h - h_f)^m,$$

(1.1)

in which $\alpha$ and, $m$ are parameters that can be adjusted to better match the curve with the power-law [58].

Stiffness can be calculated by differentiating the Equation 1.1 when $P$ equals to $P_{max}$,

$$S = \alpha m(h - h_f)^{(m-1)},$$

(1.2)

where $\alpha$ and $m$ are fitting parameters in Equation 1.2 [58].
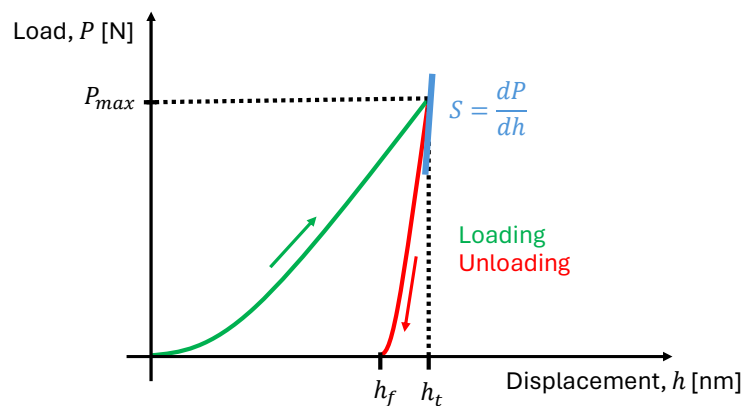


Figure 14: Schematic representation of indentation load–displacement curve showing the loading and unloading phase with the important parameters.

Concerning the modeling of an ideal spherical rigid indenter in contact with a sample, a schematic is represented in Figure 15. The new parameters entering the figure are $R_{tip}, R_c$ and $h_c$. Each of these parameters are described in the next paragraph.

The parameter $R_{\text{tip}}$ represents the radius of the tip. The indenter radius can vary depending on the type of indenter used, but typical value ranges from $50$ to $200$ $nm$. These dimensions are important to be chosen because they can affect the accuracy of the measurement during the nanoindentation tests [66]. During nanoindentation tests, either the force or the displacement to be applied is fixed, depending on the study's objective. The parameters $R_c$ and $h_c$ correspond respectively to the contact radius and the depth of the contact zone, 2 important parameters for theoretical calculations. It is essential to distinguish between the total depth of indenter penetration and the contact depth. The latter represents the effective contact height between the material and the indenter. The contact radius, on the other hand, is determined by the radius of the zone formed when the indenter is in direct contact with the material,

$$R_c = \sqrt{h_t R_{\text{tip}}}, \tag{1.3}$$

and it can be easily calculated thanks to the Equation 1.3 [72].

For a spherical geometric indenter, the depth of the contact zone can be easily calculated by Equation 1.4,

$$h_c = h_t - \frac{3}{4}\frac{P}{S}, \tag{1.4}$$

establishing a relationship between the contact depth with the total penetration depth, the applied load and the stiffness.

If the penetration has an elastic response, which is the case at the beginning of the loading,

$$h_t = 2h_c, \tag{1.5}$$

where this parameter, $h_c$ , can be calculated thanks to the Equation 1.5 [68].

Equation 1.6 shows the link between the contact area, $A_c$ with $R_c$ which can also be linked to $R_{\text{tip}}$ and $h_t$,

$$A_c = \pi R_c^2 = \pi h_t R_{tip}, \tag{1.6}$$

which is an important relationship for further calculations of the mechanical properties of the material during nanoindentation tests [68] .



Figure 15: Schematic representation of contact geometry during the loading process with a spherical indenter, showing the important parameters (inspired from [68]).

Equation 1.7 is the fundamental relationship in nanoindentation,

$$S = \frac{2}{\sqrt{\pi}}E_r\sqrt{A_c}, \tag{1.7}$$

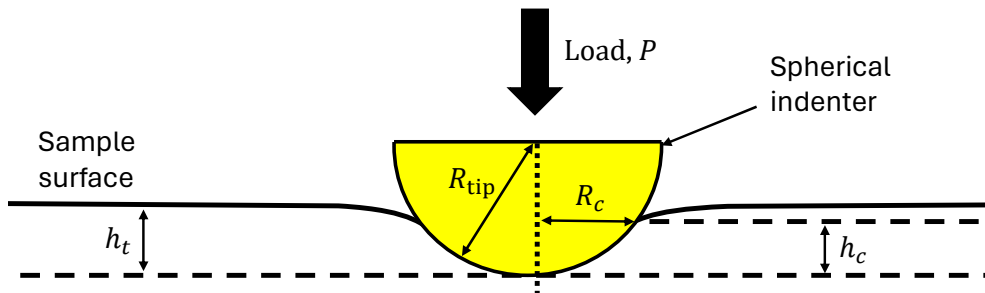where $S$ is determined by the slope at the beginning of the unloading part as illustrated, and $E_r$ is the effective elastic modulus. This relationship is applicable for 3D and axisymmetric problems [55].

This Equation 1.7 can be readapted as shown in Equation 1.8,

$$S = \frac{2}{\sqrt{\pi}} \beta E_r \sqrt{A_c},$$
(1.8)

to account for the geometry of the indenter by inserting a dimensionless parameter $\beta$, which is considered as a correction factor. Typically, this parameter is assumed to be equal to 1, but for more accurate calculations, it may deviate slightly from 1. These values can be found in the litterature [72].

The Young's modulus of a material is a physical quantity that characterizes the mechanical behavior of materials. It measures the material's resistance to deformation when subjected to stress.

In nanoindentation tests, the indenter, made of a hard material, often diamond, interacts with the sample, made of a softer material. As a result, the mechanical behavior of the material cannot be described solely by its Young's modulus. For this reason, $E_r$ must be defined to take account of the complex interaction between the 2 materials. $E_r$ represents the apparent stiffness between the sample and the indenter. For a monolithic material, $E_r$ can be calculated easily thanks to the Equation 1.9,

$$E_r = \left( \frac{1 - \nu_{\text{indenter}}^2}{E_{\text{indenter}}} + \frac{1 - \nu_{sample}^2}{E_{sample}} \right)^{-1},$$
(1.9)

where $\nu$ and $E$ represent the Poisson's ratio and the Young's modulus respectively. The indices 'sample' and 'indenter' designate the tested sample and the indenter, respectively [4]. The modulus of elasticity measured by indentation helps us to understand the response of a material when subjected to local stress. A high modulus of elasticity means that the material has a high degree of rigidity, indicating resistance to deformation. Conversely, a lower modulus of elasticity indicates that the material is more ductile, and therefore susceptible to deformation [59].

The Oliver-Pharr method, however, has certain limitations. Due to its assumptions, it is unable to characterize the mechanical behavior of more complex materials such as cortical bone, which is a multiscale and heterogeneous material. Thus, although it is commonly used to assess mechanical properties, it is important to keep in mind the assumptions and limitations of the model because this approach provides an approximation [70].

▶ **HERTZ**

The theory of Hertzian contact mechanics is the best-known method. It is the most widely used indentation theory

The Hertz model has different assumptions to be used which are the following ones [59] [73] [74]:

- ○ Isotropic elastic materials;

- ○ The interaction between the materials must be frictionless;

- ○ The indenter transmits only normal pressure to the sample;

○ The surface of contact must be continuous, smooth, and nonconforming;

○ The radius of contact must be small compared to the size of the sample tested.

The classical theory used is a sphere in contact with a half-space, as represented in Figure 16. Hertz was able to establish a relationship as shown in Equation 1.10,

$$P = \frac{4}{3} E_r R_{\text{tip}}^{\frac{1}{2}} h_t^{\frac{3}{2}}, \tag{1.10}$$

which has been validated for the contact between the spherical indenter and the flat surface [73] [75] [76].

It is also possible to fit the load-displacement curve with a power law of the depth penetration as shown in Equation 1.11,

$$P = ah^b + c, \tag{1.11}$$

where $a$, $b$ and $c$ are fitting parameters. This equation shows that, in materials possessing inclusions softer than their surroundings, a deviation from the Hertz model occurs. Indeed, this deviation manifests compared to the Hertz model, which assumes a perfect contact between a smooth surface and the indenter. Moreover, the appearance of grooves may occur after polishing, as softer materials polish more quickly than harder materials [75].

The contact stiffness can be calculated by differentiating the Equation 1.11 as shown in Equation 1.12,

$$K = \frac{dP}{dh} = abh^{b-1}, \tag{1.12}$$

where $K$ is the contact stiffness based directly on the slope of the power law [75].
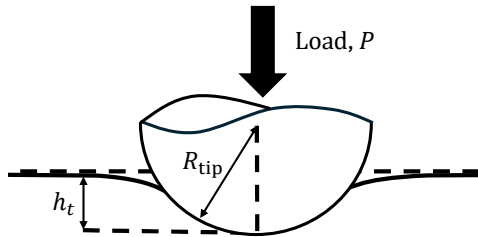


Figure 16: Schematic representation of the contact between a spherical indenter with a flat surface (inspired from [77]).

For a contact of 2 cylinders with axes parallel (see Figure 17), Equation 1.13 has been developed,

$$b = \left( \frac{2PR_{eq}}{\pi E_r} \right)^{\frac{1}{2}}, \tag{1.13}$$

describing the interaction of 2 cylinders pressing against each other. In this equation, the load, $P$, represents here a force per unit of length. The contact zone is defined by a half-length, denoted by $b$. The parameter $R_{eq}$ represents the reduced radius that can be calculated thanks to the Equation 1.14,

$$\frac{1}{R_{eq}} = \frac{1}{R_1} + \frac{1}{R_2}, \tag{1.14}$$

where $R_1$ and $R_2$ are the radii of the 2 cylinders.

For 2 cylinders with parallel axes, the force can be determined easily with the Equation 1.15,

$$P = \frac{\pi}{4} E_r L h_t = \frac{\pi}{4} E_r L \frac{b^2}{R_{\text{eq}}}, \tag{1.15}$$

showing that it is proportional to the total penetration depth and to the length of the cylinders denoted by $L$ [78].
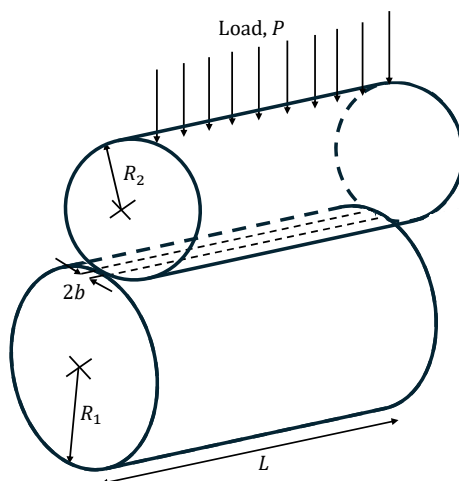


Figure 17: Schematic representation of the contact between 2 cylinders with axes parallel (inspired from [74]).

### 1.2.5   Limits and challenges of nanoindentation

As bone is a complex biological tissue due to its hierarchical structure, it exhibits high heterogeneity and complex anisotropic properties, as explained in the previous sections. These aspects can complicate the interpretation of experimental results obtained during nanoindentation tests [70].

Additionally, when nanoindentation is used to characterize the mechanical properties of bone, as the biological tissue is not homogeneous in these properties and due to the different interfaces, this can result in a blurring effect between these stiffened parts and the softer parts of the biological tissue [56]. This blurred area means that the transition zone between the 2 parts may appear larger than it is. This effect arises when measuring via indentation mapping, as the tip deforms a large area due to its size, which can complicate the precise delineation of the boundary between the interfaces. In contrast, the FEM can help study this transition between different types of biological tissue, offering more precise resolution by eliminating experimental limitations such as the blurring caused by indentation mapping [79].

Zlotnikov et al. [62] studied the ultra-thin organic layers in biosilica, as experimental data in the literature showed many contradictions in the Young's modulus due to the extremely thin thickness of the layer. Given that the diameter of the tip ($280\ nm$) exceeded the thickness of the organic layer ($35\ nm$), the indenter touched the stiffer ceramic on either side of the softer organic layer. Consequently, this altered the results as the modulus decreased approaching the ceramic-organic interface, while a peak in the modulus appeared at the center of the layer, complicating the determination of the exact modulus of the organic layer. Through simulations using the FEM, they aligned the experimental curve with those simulated for different

Young's moduli of the compliant part, thus precisely determining the Young's modulus of the latter. These results demonstrate the utility and importance of the simulations that enabled the determination of the mechanical properties of this very thin layer.

Furthermore, during experimental nanoindentation tests, it is the challenge related to the determination of the initial contact point between the indenter and the sample, and there are uncertainties regarding the precise geometry of the penetrator and the isotropy of the materials [59]. To overcome this limitation, the results can be combined with FEM to study the limits of instrumented indentation [56].

FEM will help to gain a more detailed understanding of the mechanical behavior of bone tissue [80]. Despite its contribution, it cannot totally replace the experimental approach. Both approaches need to be complementary to achieve a more comprehensive understanding of the mechanical properties of biological tissue.

## 1.3   Main aim of This Thesis

The literature reviewed in the previous sections shows the sustained interest in nanoindentation, a subject widely studied and continually used in various types of research. In the context of the bone-CL interface, indentation analysis is a key element in characterizing and understanding the structure-function relationships that play an important role in mechanical properties. The study of this zone may enable these interactions to be reproduced in other applications [56]. However, the precise role of the CL is still the subject of ongoing research. Many aspects are still poorly understood. As pointed out, experimental approaches alone do not provide a full understanding of mechanical behavior due to the thin thickness of the CL, measuring $1 - 5\,\mu m$ [7]. Thanks to numerical simulations, it is possible to understand some behaviors at multiple scales that are not understood through experimental methods [15].

To contextualize the main goal of this master's thesis, it is essential to revisit previous experimental work in the lab (Cantamessa et al. ESB 2023), which evaluated the mechanical properties of the CL and the surrounding bone experimentally. Using nanoindentation tests with grids of indents spaced at $1\,\mu m$ and penetrating up to about $150\,nm$ under a force of $500\,\mu N$, it was shown that the CL is significantly stiffer than the corresponding osteon. These results form the basis of this study, which aims to overcome the limitations of experimental tests, which rely on a probed surface of approximately the same size of the CL. The objective here is to examine the influence of bone interfaces on the mechanical properties measured by nanoindentation in bone tissues with varying mineral contents and ages. To this end, 2D simulations are used to deepen our understanding of the mechanical properties measured during nanoindentation across these interfaces.

The study is divided into 2 main phases. Initially, the focus is on the differences in material properties in order to assess the impact of the bone internal interfaces on the variability in measurements of indentations at different positions. Subsequently, the role of the inclination of the interfaces on mechanical behavior is examined. The simulations offer an insight into the variability of mechanical properties within the CL, thereby supporting a better interpretation of the experimental measurements.

# Chapter 2

# Materials and methods

In this chapter, the study focuses on the use of FE simulation models to characterize the mechanical behavior of bone interfaces during nanoindentation. Initially, a 3D model was used to best capture the interactions of materials in order to compare them with experimental tests. However, numerous convergence problems were encountered, which led to the adoption of 2D modeling to continue the analysis more effectively. This section presents and details the choice of models, the configurations of the meshes, and the various parameters used during the simulations. The simulations were performed using ANSYS WORKBENCH 2023 R2 software. As for the processing of the data provided by the simulations, this was done using MATLAB software.The simulations were run on a 20-core computer. Moreover, for all my simulations, the geometric modeling was done using the SPACECLAIM interface in ANSYS.

## 2.1 Simplifying assumptions

Different hypotheses have been formulated to simplify the study. The hypotheses retained in the work are as follows:

○ Isotropic materials: the mechanical properties of the material are identical in all directions;

○ Homogeneous materials: the mechanical properties, such as Young's modulus and Poisson's ratio, are identical throughout the material;

○ Absence of volumetric force: volumetric forces, such as gravity, are neglected;

○ Linearly elastic material: the yield strength is not exceeded. Although this hypothesis is simplifying, it is not realistic because the bone reaches plastic deformation for the indentation depths that will be simulated, namely $150\ nm$. However, this hypothesis allows for the simplification of the study by assuming that the loading and unloading curves overlap, as shown in Figure 18(a). In reality, during experimental tests, the material undergoes plastic deformation, resulting in non-overlapping loading and unloading curves (see Figure 18(b)). Furthermore, the tip can be held at a certain depth for a period, called the holding phase, before being released (see Figure 18(c)).



(a). Linear elastic.          (b). Plastic.          (c). Plastic and holding.
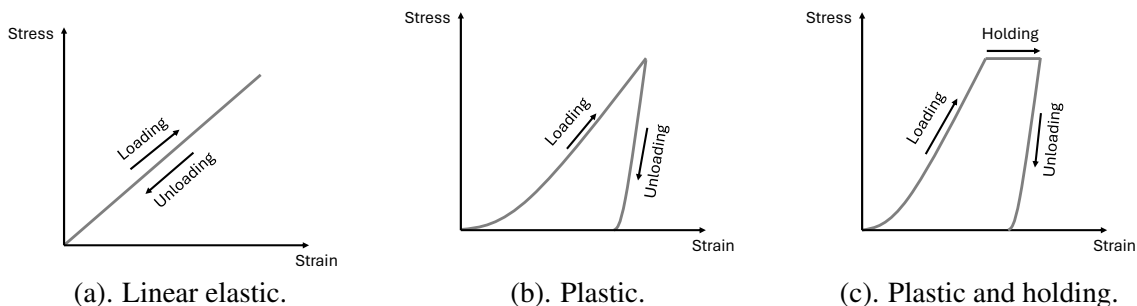
Figure 18: Schematic representation of the loading and unloading curves for different models.

## 2.2 Experimenting with 3D indentation depth

This study continues the preliminary work conducted by Astrid Cantamessa, who analyzed interfaces in 3D with a penetration of only $5\ nm$. However, the goal of this work is to increase the penetration to $150\ nm$ in order to better match the experimental studies carried out by Astrid Cantamessa. The study must therefore evolve from a basic model to a more complex model that requires detailed adjustments in the following sections.

### 2.2.1 3D modelling

#### ► GEOMETRY

The modelling of the 3D geometry is shown in Figure 19 with its dimensions which was chosen to be large enough not to feel the edges. The radius of the indenter will be the same for all the simulations performed because the goal of the study is to understand what has been conducted experimentally by Astrid Cantamessa. Therefore, the radius of the indenter is $200\ nm$. In terms of the dimensions of the sample tested, the length is $1\ \mu m$, the height is $0.5\ \mu m$ and the width is $0.25\ \mu m$. The location of the chosen Cartesian axis system is also illustrated.
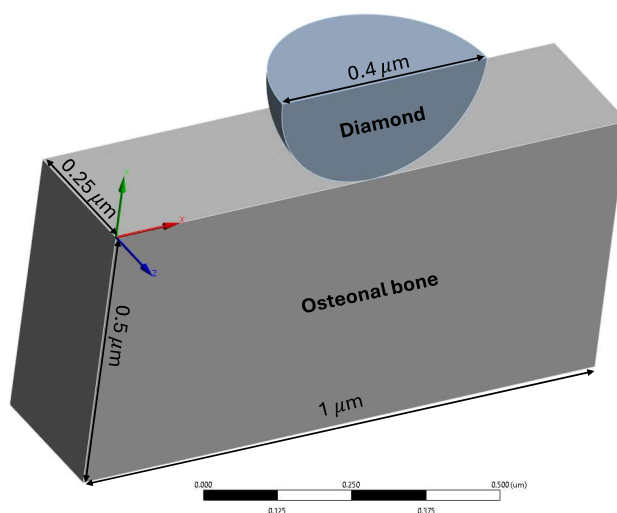


Figure 19: Symmetrically cut 3D model with annotated dimensions showing a spherical diamond indenter with a diameter of $0.2\ \mu m$. Model dimensions representing the osteonal bone are $1\ \mu m$ in length, $0.5\ \mu m$ in height and $0.25\ \mu m$ in width. The scale bar at the bottom shows dimensions in micrometers.

It became clear that the structure is symmetrical. Therefore, it is possible to focus the analysis on only half of it to reduce the computation time [75]. The 2 selected faces are shown in red on Figure 20 and have been aligned along the $z$-axis using the 'symmetry normal' option. Furthermore, previous work has shown that both configurations (a complete model and a symmetrical model) yield similar results. This justifies the decision to use the symmetrical approach for 3D simulations.
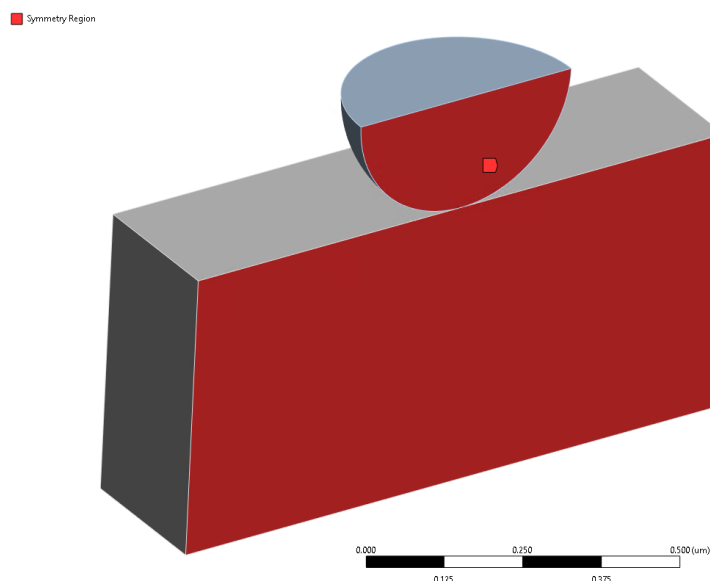
Figure 20: Symmetrically cut 3D model illustrating the region of symmetry in red, covering both diamond and osteonal bone. The scale bar at the bottom shows dimensions in $\mu m$.

## ▶ MESH

Regarding the meshing of this model, a study was conducted to identify the mesh configuration that provides the required accuracy while maintaining an optimal computation time. This investigation, performed by Astrid Cantamessa, involved simulations with the penetration of the tip along the negative $y$-axis to a depth of $5\ nm$ depth. By evaluating different meshes, one precise mesh ensuring accurate results was chosen. An illustration of the mesh is shown in Figure 21.

The approach to meshing begins with applying the 'Multizone' method to achieve a mapped hexahedral mesh with quadratic order elements. The source selection for this mesh was the upper face of the bone in order to achieve good resolution in the areas that are most critical, namely at the contact point. Next, a 'Face sizing' with an element size of $5\ nm$ was uniformly applied to this same upper face.

Also, on the bone geometry, an 'inflation' was implemented starting from the back face. The 'first layer thickness' option was adjusted to $15\ nm$ with a total of $8$ layers and a growth rate of $1$. This was put in place to optimize the computation time by increasing the mesh size away from the contact while maintaining a sufficiently fine mesh near the area of interest.

Finally, an 'edge sizing' was applied to the $4$ edges of the bone, with the 'number of divisions' set at $17$. Additionally, advanced settings were also modified by applying a 'hard bias' with a 'smooth transition' option and a 'growth factor' of $1.2$ in order to maintain a denser mesh where the stresses will be high.

Regarding the diamond, 2 types of meshing were applied. First, a 'body sizing' with an element size of $10\ nm$. Then, a 'refinement' on the outer face of the diamond in contact with the bone was done to model the geometry in such a way that it approximates a sphere as closely as possible and to avoid the irregularities that can be caused by meshing for curved surfaces.
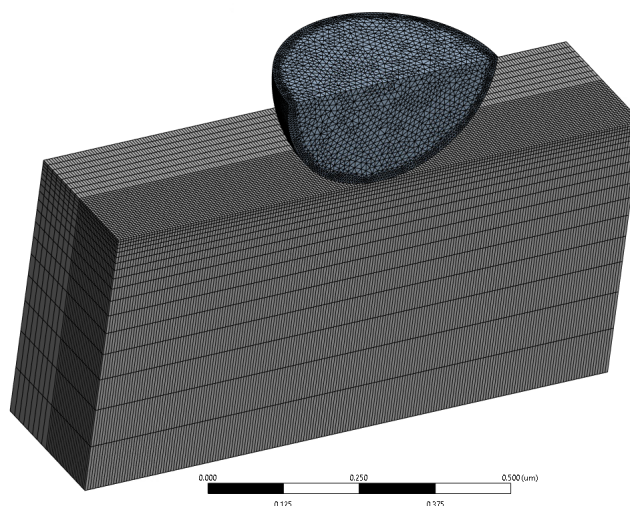
Figure 21: 3D mesh of the symmetrical model used for simulations, including both diamond and osteonal bone. The scale bar at the bottom indicates dimensions in $\mu m$.

▶ **PARAMETERS**

All necessary configurations, including the definition of contacts, boundary conditions, and other relevant parameters for this type of simulation, are explained in detail in this section and are applied to each configuration explained later. For the desired 3D simulations, some parameters were adjusted in an attempt to achieve convergence of results when these attempts failed. These adjustments, along with the explanations behind them, are provided in Section 2.2.2.

Regarding the configuration of the 'steps controls' parameters, whose purpose is explained in more detail just after, Table 2 presents the values used in the software.

| | |
|---|---|
| *Number Of Steps* | 20 |
| *Current Step Number* | 1 |
| *Step End Time* | 1 second |
| *Auto Time Stepping* | Program controlled |

Table 2: Step controls.

In non-linear simulations, time steps must be carefully adjusted to ensure convergence and accuracy of results. To access the various options, go to 'Analysis Settings' and then to 'Step Controls'. By default, the parameters are controlled by the software, which automatically adjusts the time step required to apply the imposed displacement increase by increments. However, the software does not always know how to correctly adapt these parameters, and it is therefore necessary to modify the options to help achieve a convergent solution.

It is possible to define an initial number of substeps, as well as a minimum and maximum substep range. Based on these fixed parameters, the software will adapt the step size by increasing or decreasing them according to the difficulties encountered by the simulation to converge. To better understand the role of each parameter, an example is shown in Figure 22.

If a total displacement of $150\ nm$ is applied, the 'step end time' can be set to $150$ seconds to make the calculations easier to understand. Substeps are related to the duration of the solution and not to the displacement applied. The time step can therefore be defined as 'Step End Time' divided by the number of substeps. An initial number of substeps equal to $1.5$ means that there are $100$ substeps in total, and so the time step is equal to $1.5$ seconds. The displacement will not reach $150\ nm$ directly, but will be imposed gradually every $1.5$ seconds.

This initial time step is used for the first calculation of the first displacement. However, if during subsequent steps, this time step does not allow convergence or finds convergence easy, the solver can adjust the time step using the 'minimum time step' and 'maximum time step' parameters. In this example, the 'minimum time step' is set to $0.15$ seconds, which means that the software will impose $1000$ substeps. This parameter means that if the solver fails to converge the solution, the time step algorithm will bisect the last substep that converged, in order to apply smaller increments. On the other hand, if the time step is too small and there is no point in wasting computation time, the solver uses the maximum time step. The software is limited only by these parameters, and cannot go beyond [81] [82].

| Details of "Analysis Settings" | |
|---|---|
| **Step Controls** | |
| Number Of Steps | 1. |
| Current Step Number | 1. |
| Step End Time | 150. s |
| Auto Time Stepping | On |
| Define By | Time |
| Initial Time Step | 1.5 s |
| Minimum Time Step | 0.15 s |
| Maximum Time Step | 1.5 s |

Figure 22: Step Controls.

Figure 23 illustrates displacement as a function of time, with the $3$ parameters for adjusting time step size. This illustration makes it easier to understand graphically the role of each of these $3$ parameters, where $\Delta t_{\text{start}}$ represents the initial time step, $\Delta t_{min}$ corresponds to the minimum time step and $\Delta t_{max}$ is the maximum time step. Displacement increments are adjusted according to these $3$ parameters throughout the simulation. More complex convergence will be achieved with smaller increments, while easier convergence will be achieved with larger increments [83].
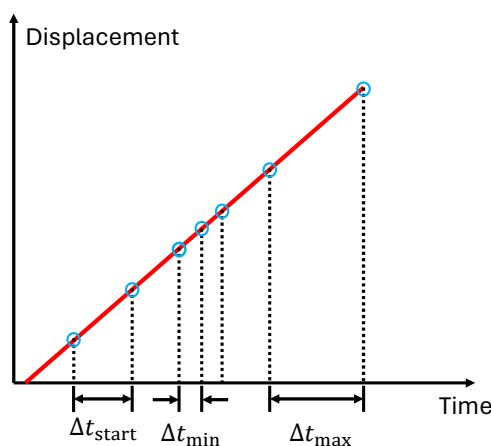
Figure 23: Graph showing displacement (red line) as a function of time (inspired from [83]).

#### ▶ MATERIALS PROPERTIES

In this model, the quarter sphere represents the spherical diamond indenter, while the rectangular parallelepiped represents the osteonal bone. The mechanical properties of these materials are given in Table 3.

| Material | Young's modulus E [GPa] | Poisson's ratio $\nu$ [-] |
|---|---|---|
| Diamond | 1140 | 0.07 |
| Osteonal bone | 20 | 0.3 |

Table 3: Materials properties.

#### ▶ CONTACT DEFINITION

In this work, an indenter must come into contact with the sample to be tested. The contact is defined as the moment when the 2 distinct surfaces of the materials touch each other. These 2 surfaces are tangent to each other. It is important to define this contact in FE analysis to obtain the expected results [84].

In ANSYS, the first step is to define the 'target' and the 'contact'. The surface of the indenter was chosen as the 'contact' because it is the surface that will penetrate into the material. The bone, being the material undergoing penetration, was defined as the 'target' surface (see Figure 24) [70].
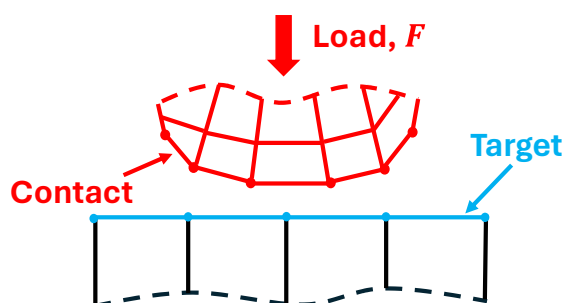


Figure 24: Schematic representation of the definition of 'target' and 'contact' surfaces in ANSYS. The surface of the indenter is defined as the 'contact', while the surface of the bone undergoing penetration is defined as the 'target' surface (inspired from [84]).

The interaction between the 2 contact surfaces was set to 'frictionless'. With this type of contact, there is no resistance between the 2 surfaces, allowing them to slide or separate freely relative to each other [33] [69].

Then, there are advanced options that also need to be set, not only defining the contact as frictionless. In the FE approach in ANSYS, it is important to prevent the physical bodies in contact from interpenetrating. This interpenetration phenomenon, as illustrated in Figure 25, is non-physical. Therefore, in the advanced options, it is possible to define the type of relationship between the contact surfaces. This procedure is known as enforcing contact compatibility. The

term 'enforce' means that the software ensures that the surfaces remain in contact but do not penetrate each other and remain tangent to each other. To achieve this, different mathematical formulations are provided in the software [84].
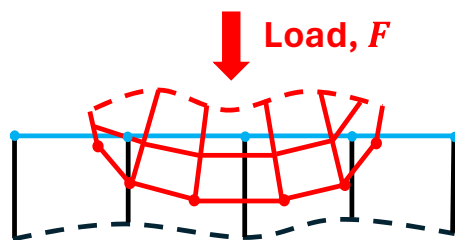


Figure 25: Schematic representation of penetration occurring due to contact compatibility, which is not enforced (inspired from [84]).

For the simulations conducted in this study, the 'Normal Lagrange' formulation was chosen. This formulation adds a degree of freedom (DOF), the contact pressure, to ensure contact compatibility. This DOF represents the force per unit area at the contact points between the 2 distinct bodies. The software calculates the necessary pressure to prevent interpenetration while maintaining contact. The disadvantage of this formulation is the increased computation time compared to other formulations [85] [86].

Figure 26(a) illustrates the Normal Lagrange method where no penetration is allowed. Throughout the simulation, the software must identify the contact status. This status is binary, meaning the 2 surfaces of the distinct bodies are either in contact (closed) or not (open). The problem with this type of step function arises when many contacts oscillate rapidly between the open and closed contact statuses, causing difficulties in the convergence of results. This phenomenon of rapid oscillations between these 2 contact statuses is called chattering [85] [86].

Conversely, there are formulations like the Penalty-Based method (see Figure 26(b)) that allows a certain amount of penetration, thus facilitating the convergence of results. However, this method requires a more in-depth study regarding the acceptable error. For more accurate results, the Normal Lagrange method was preferred. Additionally, an extra option was enabled in the 'interface treatment', set to 'adjust to touch'. This option adjusts the nodes so that the surfaces of the bodies in contact perfectly touch each other when the simulation starts [85] [86].
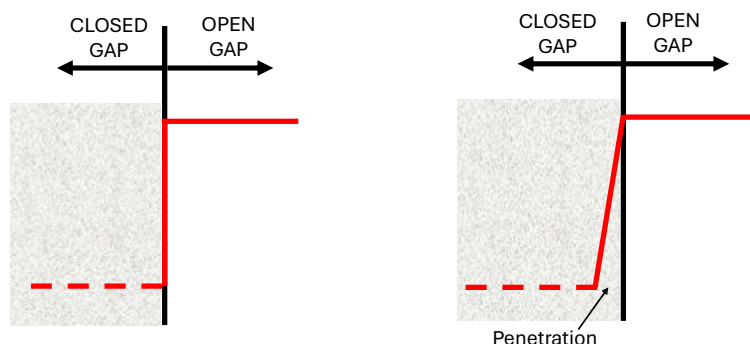


(a). Normal Lagrande method.

(b). Penalty-Based method.

Figure 26: Schematic representation of 2 formulations for contact (inspired from [86]).

► **BOUNDARY CONDITIONS**

**INDENTER**

For the indenter, the boundary conditions consist of imposing a vertical downward displacement. This displacement should not occur abruptly but gradually. Therefore, tabular data was inserted for the $y$ component, allowing the creation of a linear displacement vector based on the chosen number of steps and substeps until the final displacement. This boundary condition was imposed on the upper face of the indenter. All other DOFs were set to $0$.

Depending on whether the simulations were carried out in 2D or 3D, different options were chosen. For the 2D case, the 'displacement' option was used, while for the 3D case, the 'remote displacement' option was selected. The values set are shown in Tables 4 and 5.

| Type | Remote displacement |
|:---:|:---:|
| **X component** | $0\ m$ |
| **Y component** | Tabular Data |
| **Z component** | $0\ m$ |
| **Rotation X** | 0° |
| **Rotation Y** | 0° |
| **Rotation Z** | 0° |

Table 4: Remote displacement.

| Type | Displacement |
|:---:|:---:|
| **X component** | $0\ m$ |
| **Y component** | Tabular Data |
| **Z component** | $0\ m$ |

Table 5: Displacement.

**SAMPLE**

With regard to sample boundary conditions, the literature on FE simulations does not propose a single method. For the simulations carried out in this work, it was decided to fix the entire model base using the 'fixed support' option (see Figure 27) [69] [87] [88] [89].
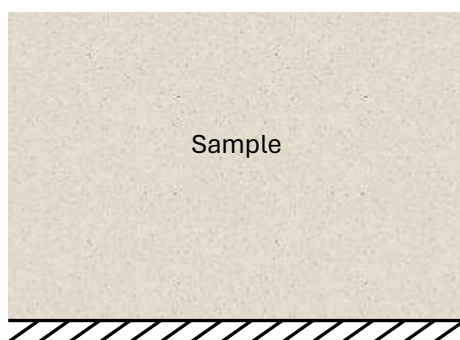


Figure 27: Boundary condition of the sample. The entire model base is fixed.

▶ **SOLVER CONTROLS**

The simulations carried out in this work are categorized as large deformations. The geometry is therefore non-linear. In ANSYS, it is necessary to activate the 'Large Deflection' option in the 'solver control' to enable the software to calculate the stiffness of the model throughout the deformation. Without this option, the approach used by the solver is to assume constant stiffness, regardless of deformation, which not only distorts the results but can also lead to non-convergence.

2 tests were carried out with and without the 'Large Deflection' option. With this option deactivated, the software was unable to achieve convergence. However, enabling this option increases computational complexity and is also time-consuming. This is why, by default, it is deactivated [90].

### 2.2.2 Attempts to resolve non-convergence in 150 nm indentation

Various simulations were attempted to achieve an indentation depth of $150\ nm$ in 3D. Through this diversity of approaches, knowledge about different parameters was gained, even though not all simulations consistently converged. This section thus highlights the most relevant approaches that were explored among all the tests conducted.

A first attempt was made by drawing inspiration from pre-existing simulations conducted by Astrid Cantamessa, for a depth of $5\ nm$. The parameters, model dimensions, and meshing are those described in the previous sections. However, this initial test did not succeed after 12 hours of simulations, indicating the presence of non-convergence issues. Figure 28 illustrates a typical example of what is visually obtained during non-convergence. The potential sources of these errors are generally difficult to quickly identify. Various possibilities can be considered, such as insufficiently refined meshing, errors related to contact definition, or an inadequate number of steps and substeps. These different sources of errors complicate the identification and resolution of the problems encountered.
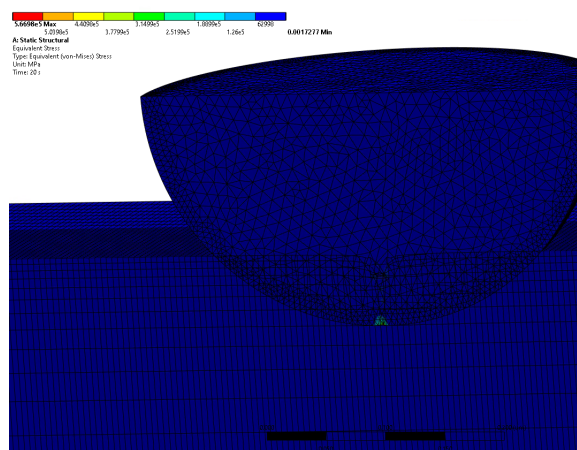


Figure 28: Typical example of a visual result obtained when simulations are not convergent.

To reduce computation time and gain a more detailed understanding of the model's behavior, a second test was conducted using a coarser mesh. To achieve this mesh, the 'sizing relevance center' option was set to 'medium,' which allows for the automatic generation of a coarse mesh. This approach led to convergence. However, the results obtained with this type of simulation

are unsatisfactory, as a coarse mesh does not accurately capture stresses and deformations. In Figure 29, the deformation of the model appears jagged around the contact area due to the coarse mesh. Following this, the mesh was refined by changing the parameter from 'medium' to 'fine,' but this adjustment did not result in successful convergence of the solution.
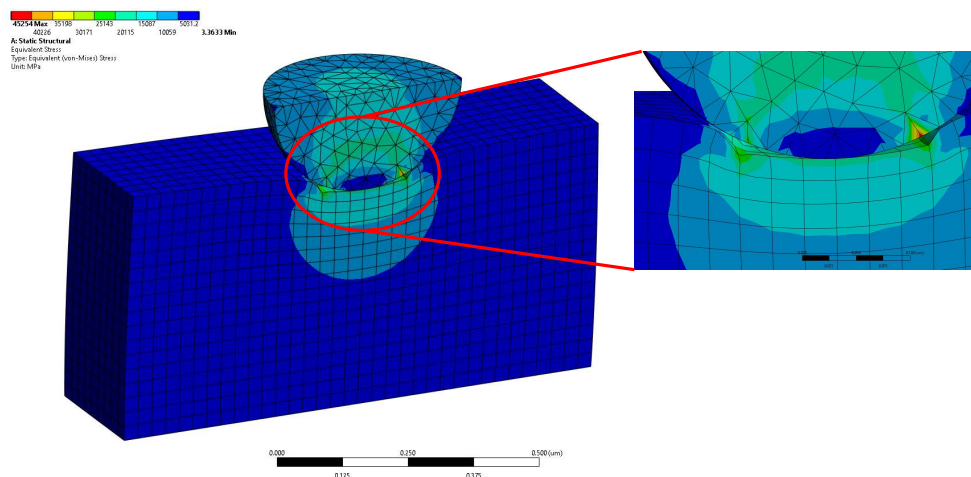


Figure 29: Typical example of a visual result obtained when simulations are not convergent.

Continuing the efforts, mesh refinement was tested down to a minimum element size of $0.5\ nm$ around the contact area between the diamond and the bone. Although this approach aimed to achieve high precision, it did not result in a convergent solution. The computation time also significantly increased, sometimes reaching 20 to 30 hours per simulation. In some cases, after 20 hours, the simulation had only completed a third of its process, necessitating its interruption because such lengthy simulations were not feasible within the timeframe of this work.

Modifications were also made to the model's dimensions, both increasing and decreasing its size. No impact on resolving the non-convergence issue was observed.

Another attempt involved modifying the parameters related to the 'stiffness behavior' of the diamond, changing it from 'flexible' to 'rigid'. This is a configuration that can sometimes be considered to facilitate the simulation, but according to the ANSYS documentation, it can also increase convergence problems [91].

Another important consideration was increasing the number of steps and substeps. Although this option plays a significant role in convergence, it did not lead to converging results. Increasing these parameters also resulted in a significant increase in computation time and storage requirements, needing up to 100 Go. A test with a total of 100 substeps failed due to the limited storage capacity of the computer available for this work, thus restricting further exploration of this approach.

Given the issues encountered with the non-convergence of the simulations at $150\ nm$, it was decided to simplify the approach by reverting to 2D simulations. This shift to 2D allows for stabilizing the complexity generated in 3D. However, before moving to 2D modeling, some simulations at $5\ nm$ in 3D were conducted. It may seem counterintuitive to remain in 3D for a penetration of $5\ nm$, but an indentation of 150 nm causes larger deformations compared to that of $5\ nm$, which complicates the convergence calculations. The configurations for these simulations are explained in the following section.

## 2.3   3D model with interface

### 2.3.1   Adding an interface

► GEOMETRY

When materials are added side by side and need to deform as a single multi-body piece, it is necessary to use an additional parameter during the geometry creation. In ANSYS, the 'Workbench' tab offers an option called 'Share,' which allows sharing the topology between contacting bodies, including faces, edges, and vertices. With this shared topology, the mesh will properly conform to the contact points between the bodies. This ensures a perfect mesh at these intersections [91].

Figure 30 shows the 3D modeling of 2 materials side by side, representing respectively, from left to right, the osteonal bone and the CL. The dimensions of each material as well as the Cartesian axis system are also illustrated. Moreover, the symmetry has also been exploited here.
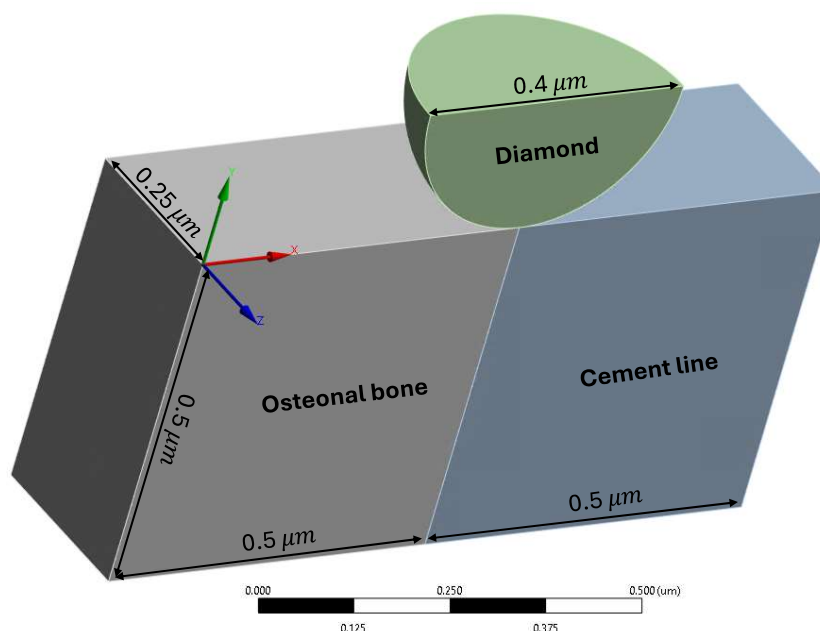


Figure 30: Symmetrically cut 3D model with annotated dimensions showing a spherical diamond indentor with a diameter of $0.2\,\mu m$. Models dimensions representing the osteonal bone and the CL are $0.5\,\mu m$ in length, $0.5\,\mu m$ in height and $0.25\,\mu m$ in width. The scale bar at the bottom shows dimensions in $\mu m$.

► MESH

Regarding the meshing, the chosen parameters are the same as those described in section 2.2.1. Indeed, this mesh has already been studied for its sensitivity and can also be used for an interface. It is important to note that the mesh is not only refined near the contact with the indenter but along the $x$-axis. This is important because, in future simulations, the indenter will move along the $x$-axis, requiring a uniform mesh to ensure good accuracy. A representation of this mesh is shown in Figure 31.
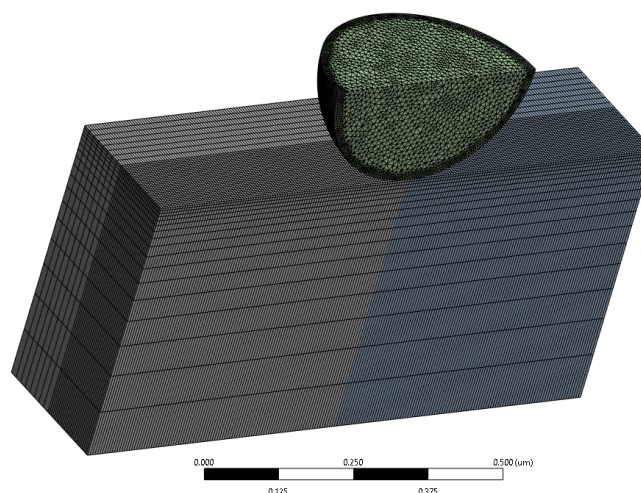
Figure 31: 3D mesh of the symmetrical model used for simulations, including both diamond, osteonal bone and CL. The scale bar at the bottom indicates dimensions in $\mu m$.

▶ **PARAMETERS**

The parameters for 'step controls' are identical to those used in the previous section.

▶ **MATERIALS PROPERTIES**

Table 6 presents the material properties defined for this type of model. In this configuration, the rectangular parallelepiped is composed of osteonal bone and the CL. For the CL, 2 values of Young's modulus were studied: 25 GPa and 30 GPa.

| Material | Young's modulus E [GPa] | Poisson's ratio $\nu$ [-] |
|---|---|---|
| Diamond | 1140 | 0.07 |
| Osteonal bone | 20 | 0.3 |
| Cement line | 25-30 | 0.3 |

Table 6: Materials properties.

### 2.3.2 Interface indentation configuration

Figure 32 illustrates the positioning of the indenter in the various simulations conducted for this configuration. The spherical indenter moves along the $x$-axis, traversing both materials: the osteonal bone and the CL. This displacement is measured relative to the interface between the 2 materials, which serves as a reference for establishing relative displacement. The starting position of the indenter is $-100\ nm$ and it moves up to $100\ nm$. The chosen positions are respectively: $-100, -50, -32, 0, 32, 50$, and $100\ nm$.

In the simulations related to this configuration, the indentation depth of the indenter is $5\ nm$. The position at $32\ nm$ is a key value because it represents the contact radius, calculated from Equation 1.3. This position is important as it corresponds to the point where the diamond indenter starts to feel the second material.
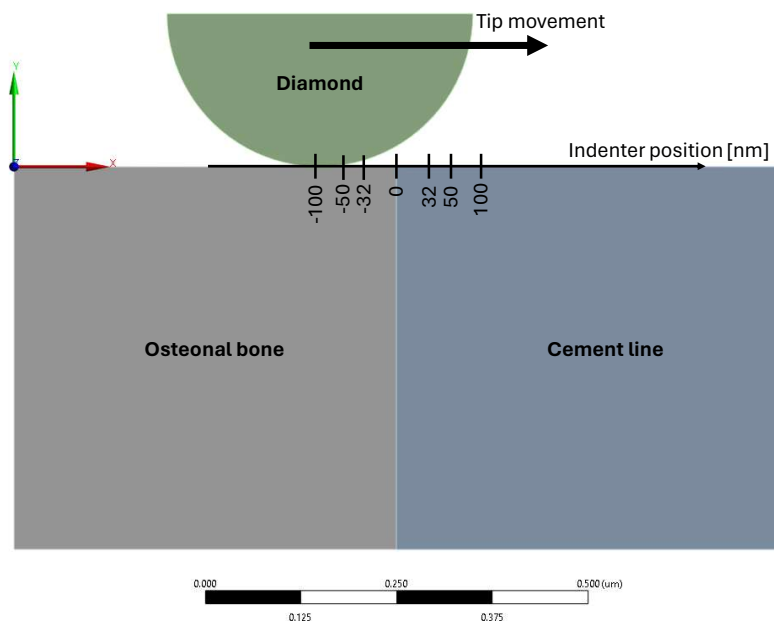
Figure 32: Representation of the simulation setup showing the movement of the diamond indenter across the interface between osteonal bone and CL. Indenter positions range from $-100\ nm$ to $100\ nm$, with key points noted at$-100, -50, -32, 0, 32, 50,$ and $100\ nm$.

## 2.4 Transition to 2D modeling

### 2.4.1 Reasons for 2D transition

The motivation for moving towards a 2D modeling approach is based on several factors, the main one being the resolution of convergence issues for large deformations.

In terms of convergence, 3D simulations, due to their complexity, make resolving non-convergence issues difficult. This complexity is significantly reduced when considering 2D modeling. Indeed, this geometric simplification facilitates the resolution of systems of equations by reducing the number of DOFs considered. Consequently, the simulations have a higher chance of converging.

Moreover, 3D modeling requires a lot of computational resources. In the context of this work, this constitutes a limitation as it restricts the ability to conduct multiple simulations with different configurations and parameters. Thus, transitioning to 2D modeling offers the advantage of significantly reducing computation time and allowing for a more advanced exploration of the study.

It is important to note that current studies on nanoindentation primarily focus on 3D and axisymmetric modeling. In this study, the axisymmetric option was not feasible because the goal is to investigate the impact of bone interfaces on mechanical properties, which requires a non-axisymmetric approach. Additionally, due to the various limitations mentioned, 3D modeling was also not a viable option within the available time frame.

The search for theoretical models to evaluate the feasibility of the study in 2D is more complex. Indeed, while current theoretical models are well-established for axisymmetric and 3D configurations, extending to 2D modeling requires more in-depth studies in the literature. Thus,

adopting a 2D modeling approach to study the bone interface is an innovative approach.

To simplify the behavior of stresses and deformations in 3D, 2 choices are possible in 2D: plane strain and plane stress. The choice was made to use plane strain. Plane strain can be defined as a plane state where all out-of-plane strains ($z$-axis) are zero, while the in-plane strains ($x$-axis and $y$-axis) are non-zero. The justification for this choice lies in the application scope of this concept. Indeed, plane strain applies to bodies whose thickness is very large, where a thin layer is taken of this very large object. In the case of bone tissues, the thickness can be considered very large [92].

Moreover, the deformation zone induced by the indenter is primarily concentrated in the direction of its penetration. The plane strain model allows for better capture of the stresses and deformations in this zone.

### 2.4.2 Replication of 3D simulations in 2D

To verify if the 2D modeling is reliable and provides key information for this type of study, a comparison between the 3D and 2D simulations was performed for an indenter penetration of $5\ nm$. This depth induces minimal deformation, facilitating convergence in 3D, thus allowing for an evaluation of the impact of 2D modeling on the results.

To ensure a reliable comparison between the 2 models, the parameters used in 2D must be the same as those in 3D. The dimensions, contact definition, 'step controls' parameters, etc., were set as in the 3D model. However, for the meshing, using the same bias factor proved to be much too coarse in 2D, preventing the convergence of the results.

To ensure a sufficiently refined mesh without conducting a sensitivity analysis for this comparison, a $5\ nm$ mesh (the most refined element size in the 3D model) with Q8 elements was used everywhere in the model. This configuration ensures that the results obtained in 2D are accurate and comparable with the 3D modeling.

### 2.4.3 Methods for obtaining Young's modulus

To obtain $E_r$ during nanoindentation tests, as described in the Section 1.2.4, there are different methods. In the case of a spherical indenter in 3D, the Young's modulus can be obtained using the Oliver-Pharr or Hertz methods. However, in 2D, the established formulas for a spherical indenter are not applicable because 2D modeling assumes that the indenter is cylindrical. The most suitable formula for deducing the reduced modulus is the theoretical Hertz model for 2 cylinders in contact with parallel axes. Additionally, an assumption is made that the radius of the cylinder representing the tested material is much larger than the radius of the cylinder representing the diamond. Therefore, the Equation to use is Equation 1.15.

# 2.5   2D advanced studies

### 2.5.1   Indentation at 150 nm in 2D

▶ **DIMENSIONS**

In the advanced studies of nanoindentation, a depth of $150\ nm$ along the negative $y$-axis is set for the indenter. The dimensions of the model are crucial to ensure that the edges of the model do not influence the results. A study described in Section 2.5.3 explains the final choice of the model's length.

Regarding the height of the model, it is often recommended for nanoindentation tests performed using the FEM to choose an indentation depth not exceeding $10\%$ of the model's height [93] [94].

In this study, to apply this rule, the height must be at least $1.5\ \mu m$. To ensure that the influence of the lower edges does not affect the accuracy of the results, a height of $3\ \mu m$ was chosen. Moreover, it does not increase the computational time.

▶ **PARAMETERS**

In the model, there is a single load step, which is the loading phase. The simulation of the loading is performed by incrementing the displacement of the indenter. Given that the number of substeps cannot be small due to the large induced deformation, the minimum number of substeps is 100 and can go up to 1000, depending on the software and simulation requirements to ensure convergence of the results [73]. The configuration of the 'step controls' parameters is shown in Table 7.

| | |
|---|---|
| *Number Of Steps* | 1 |
| *Current Step Number* | 1 |
| *Step End Time* | 150 seconds |
| *Auto Time Stepping* | On |
| *Define By* | Time |
| *Initial Time Step* | 1.5 seconds |
| *Minimum Time Step* | 0.15 |
| *Maximum Time Step* | 1.5 seconds |

Table 7: Step Controls.

### 2.5.2   Mesh sensitivity analysis

▶ **DEFINITION OF ALL ELEMENTS USED**

In the context of this study on mesh sensitivity, the first type of element studied was T6 element, as illustrated in Figure 33, was used. This element consists of 6 nodes positioned at the vertices of the triangle and at the midpoints of each of its sides. This element is part of the category of parabolic triangular elements. Moreover, each node has 2 DOFs. Therefore, the T6 element has a total of 12 DOFs. An advantage of the T6 element is the use of shape functions characterized by second-degree polynomials. Thus, it is capable of applying displacements following a quadratic model, which allows it to model complex curves with high precision and to capture

the elevated variations in the fields of stresses and deformations. It therefore allows for a more faithful representation of the observed physical phenomena [95] [96].
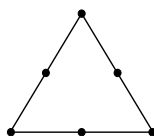


Figure 33: Schematic representation of the element T6.

The second element used is the Q8 element, illustrated in Figure 34. This element is a quadrilateral with eight nodes, giving it a total of 16 DOFs. At the corner, there is 1 node and at the midpoint of each side of the quadrilateral. Analytically, displacements are modeled by third-order polynomial functions. This implies that the shape functions are also third-order functions. In terms of advantages, it is clear that this element provides better accuracy and a more faithful representation of curvatures. Its benefits make it ideal for applications requiring high precision in stress and deformation analysis [95] [96].
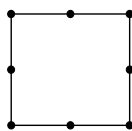


Figure 34: Schematic representation of the element Q8.

Figure 36 shows the evolution of 4 variables as a function of the number of elements generated in each simulation. These evolutions will be evaluated for 2 types of meshes: T6 and Q8.

For this sensitivity analysis study, a coarse mesh composed of elements with an initial size of $100\ nm$, refined down to $5\ nm$ near the contact, was used. The mesh of the indenter was not modified between each simulation, as the precision needs to reside in the tested sample. For the indenter, a mesh composed of quadratic triangular elements (T6) with an element size of $10\ nm$ and refinement around the contact with the sample was chosen. Triangular elements were selected due to their ease of adapting to curved surfaces like the indenter, which is not the case with quadrilateral elements [95].

To study the overall convergence, the analysis of the average displacement induced in the entire structure was conducted. Figure 36(a) shows that both types of elements allow convergence towards a similar value and at a similar rate.

Regarding the study of local convergence, the maximum value of the Von Mises stress in the sample was evaluated as a function of the number of elements. This parameter provides a good indication of the local stress concentration in the tested sample. Figure 36(b) shows that the Von Mises stress is bounded in its growth for both types of elements. Both element types converge to the same value and do so quickly.

Since the goal of this work is to study the Young's modulus based on the obtained reaction force, a sensitivity study of the reaction force was also conducted, as shown in Figure 36(c). This graph shows that a coarse mesh causes oscillations in the reaction force value, and these

oscillations stabilize as the mesh is refined. The more elements there are, the more the reaction force stabilizes for both types of elements.

Finally, an important factor to consider is the CPU time, illustrated in Figure 36(d). Analyzing this, the computation time evolves more or less linearly for each mesh as a function of the number of elements. However, a difference can be observed between the 2 types of elements, as they do not have the same slope. The goal is to minimize computation time while maintaining good accuracy.

Therefore, the choice is not for the most refined mesh, but for the previous one in terms of number of elements that gives similar results. For this mesh, the computation time between the 2 types of elements differs by a few minutes. The choice was made for Q8 elements because they are better suited to the rectangular shape of the model. Indeed, T6 elements are placed heterogeneously in the model, unlike Q8 elements, which perfectly fit the rectangular sample. The selected mesh cannot be visually displayed due to its refinement and the large size of the model, which exceeds the display capabilities of the available computer. But a zoomed-in view of the mesh is illustrated in Figure 35. For the final mesh parameters, the first step is to apply an 'Edge Sizing' with an element size of $5\ nm$ on the top edge of the model. Next, an 'Edge Sizing' was applied to the 2 sides of the bone, with the 'number of divisions' set to $250$ and the 'bias factor' option set to $6$. Finally, the 'Multizone' method was used to obtain a mesh with PLANE183 elements.
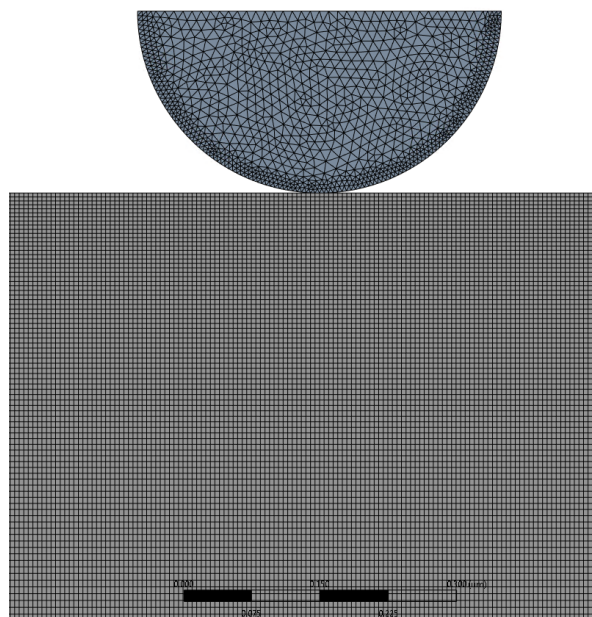


Figure 35: A close-up view of the 2D mesh used for simulations, including both diamond and bone. The scale bar at the bottom indicates dimensions in $\mu m$.

(a). Average displacement
in micrometers [$\mu$m].

(b). Maximum equivalent Von Mises stress
in megapascals [MPa].

(c). Reaction force in newtons [N].

(d). CPU time in seconds [s].
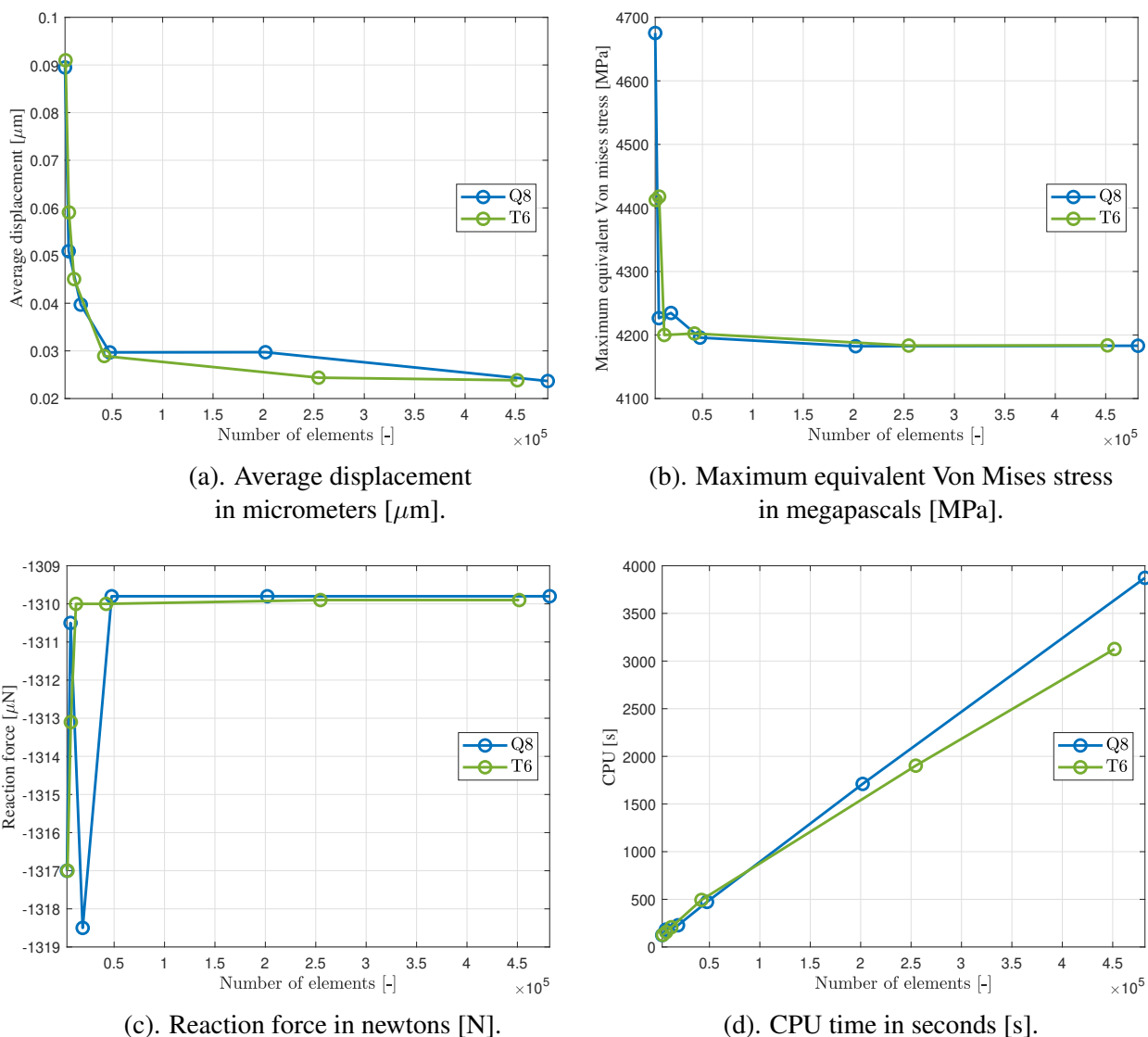
Figure 36: Mesh sensitivity analysis for $4$ different key variables as a function of the number of elements, with an imposed displacement of $150\ nm$ for $2$ mesh types: quadrilateral elements with 8 nodes (Q8) and triangular elements with 6 nodes (T6) shown in blue and green respectively.

### 2.5.3   Influence of model length

In this work, the study focuses on the mechanical properties across the bone interfaces during nanoindentation tests. The CL is the key point of the study. However, this thin layer has a thickness between 1 and 5 $\mu m$. For the simulations, the chosen thickness is the smallest, 1 $\mu m$. In the modeling, the osteonal bone is on the left of the CL, and the IB is on the right. These tissues (osteonal bone and IB) have much greater thicknesses than that of the CL.

To avoid significantly increasing the computation time, it is necessary to choose a thickness for these tissues. However, since the indentation is performed to a depth of $150\ nm$, the outermost edges can be felt and influence the results. Therefore, it is important to study the influence of the edges on the accuracy of the results.

Figure 37 shows in blue the parameter representing the half-length of the bone sample, which

is modified for each of the simulations conducted in this section. The other dimensions have been fixed and discussed previously.

0.4 $\mu$m

Half-length

3 $\mu$m
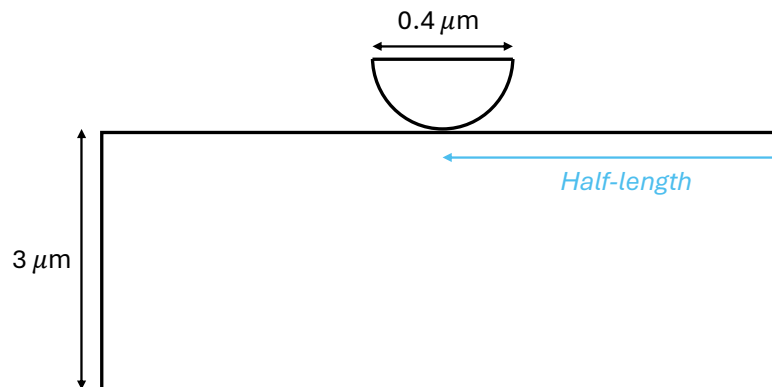
Figure 37: Schematic representation of the model with the parameter representing the half-length of the model in blue which is modified for each simulation of this section. Other dimensions are fixed, the height of the model is $3$ $\mu m$ and the diameter of the diamond is $0.4$ $\mu m$.

Figure 38 shows the evolution of the $E_r$ as a function of the half-length of the model. It can be observed that as the length of the model increases, the $E_r$ converges to a certain value. Therefore, the indentation must take place at a maximum distance of $3.5$ $\mu m$ from the edges. The chosen size for the osteonal bone and IB will therefore be $4$ $\mu m$, as the goal is to study what happens near the bone interface. This interface should be studied within a perimeter of approximately $500$ $nm$ around it.
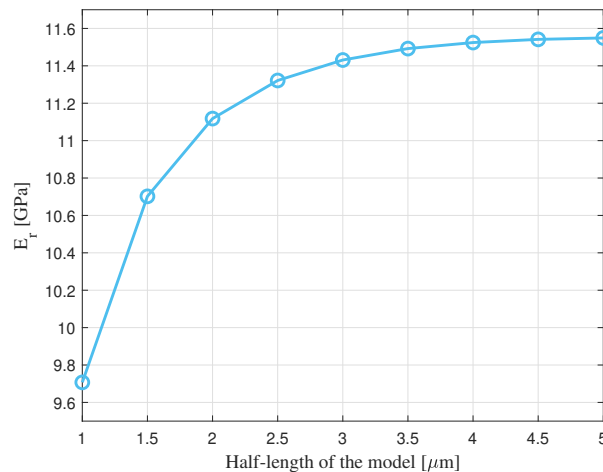
Figure 38: Graph showing the influence of the model half-length in $\mu m$ in the value of the effective Young's modulus in GPa.

In a more qualitative manner, the deformation in $\mu m$ induced in the model can be illustrated for 2 different lengths. The deformation here is defined as the displacement induced in the model. This latter was chosen because it directly influences $E_r$ that will be obtained. It can be seen in Figure 39(a) that with a half-length of $2$ $\mu m$, the displacement of the model also occurs at the edges. This has a direct impact on $E_r$ obtained. In contrast, as shown in Figure 39(b), with

a half-length of $3.5$ $\mu m$, the edges no longer influence the visual result of the displacement induced in the model.
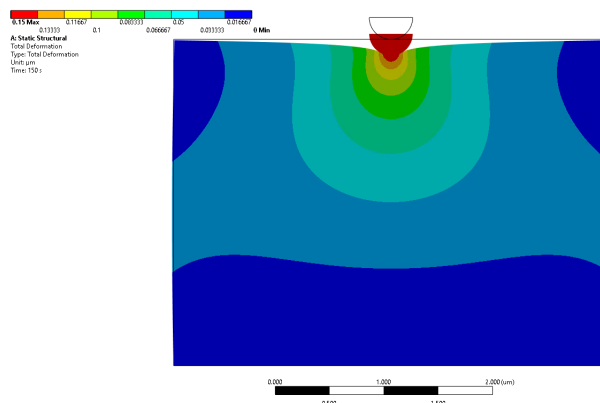


(a). Model length of $4$ $\mu m$ (half-length of $2$ $\mu m$).
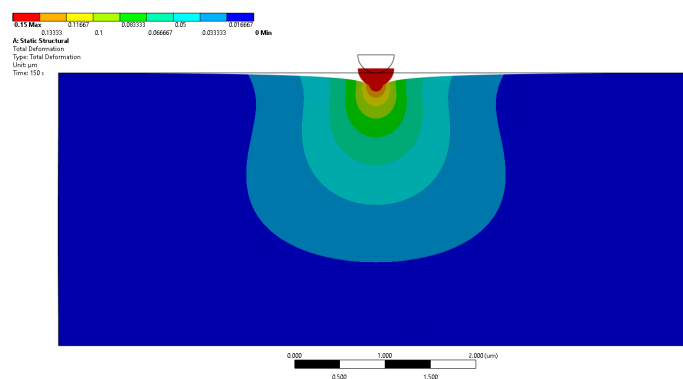


(b). Model length of $7$ $\mu m$ (half-length of $3.5$ $\mu m$).

Figure 39: Spatial distribution of the displacement, showing the influence of model length.

## 2.6    Introduction of 3 materials in 2D

### 2.6.1    Placement of the tip

For this part of the study, $3$ materials are modeled side by side (osteonal bone, CL, and IB). The goal is to study the mechanical behavior at the interface between the osteonal bone and the CL, as well as at the interface between the CL and the IB. To choose the strategic points for placing the indenter, the contact radius, calculated from Equation 1.3, was used as a reference.

For an indenter depth of $150$ $nm$ in the negative $y$ direction, the contact radius is $173$ $nm$, as illustrated in Figure 40, where the contact radius is symbolized in yellow. The placement of the indenter is measured relative to the osteonal bone-CL interface and is chosen to be a multiple of the contact radius. The middle of the CL and the interfaces have also been included as a placement point.

Each position of the indenter is illustrated in Figure 41. The chosen positions are respectively: $-3R_{c_1}, -2R_{c_1}, -1R_{c_1}, -0.5R_{c_1}$, Interface 1, $1R_{c_1}, 2R_{c_1}$, Middle of the CL, $-2R_{c_2}, -1R_{c_2}$, Interface 2, $1R_{c_2}, 2R_{c_2}$ and $3R_{c_2}$.
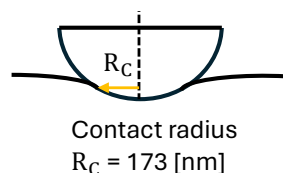
Figure 40: Schematic represenation of the contact radius.
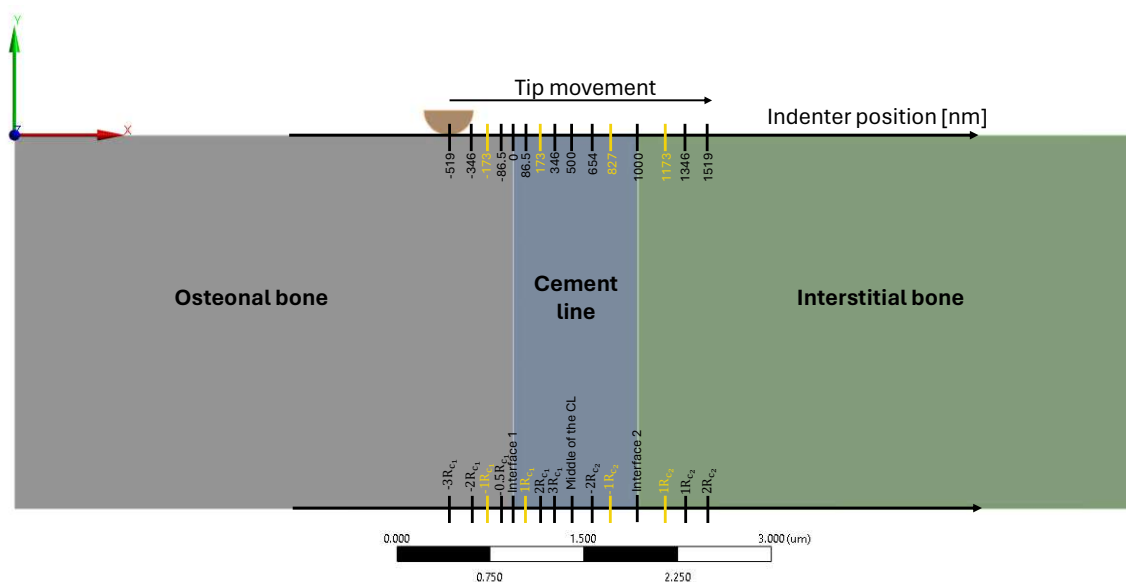


Figure 41: Representation of the simulation setup showing the movement of the diamond indenter across the interfaces between osteonal bone, CL and IB. Indenter positions range from $-3R_{c_1}$ to $3R_{c_2}$.

### 2.6.2 Tilted cement line

The second advanced part of the study focuses on the inclination of the interfaces. The inclination is measured in degrees, using the vertical interface as a reference. It is measured positively in the clockwise direction and negatively in the counter-clockwise direction (see Figure 42). 4 inclinations are studied: $-45°$, $-30°$, $30°$, and $45°$. The geometry of these different configurations for each inclination is illustrated respectively in Figures 43(a), 43(b), 43(c),and 43(d).
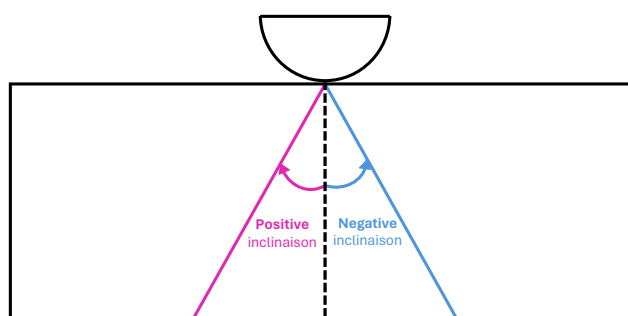


Figure 42: Schematic representation of the CL tilted. Inclination is measured in degrees relative to the vertical interface, with positive inclinations clockwise and negative inclinations counter-clockwise.

(a). CL tilted at -45°.



(b). CL tilted at -30°.



(c). CL tilted at 30°.



(d). CL tilted at 45°.
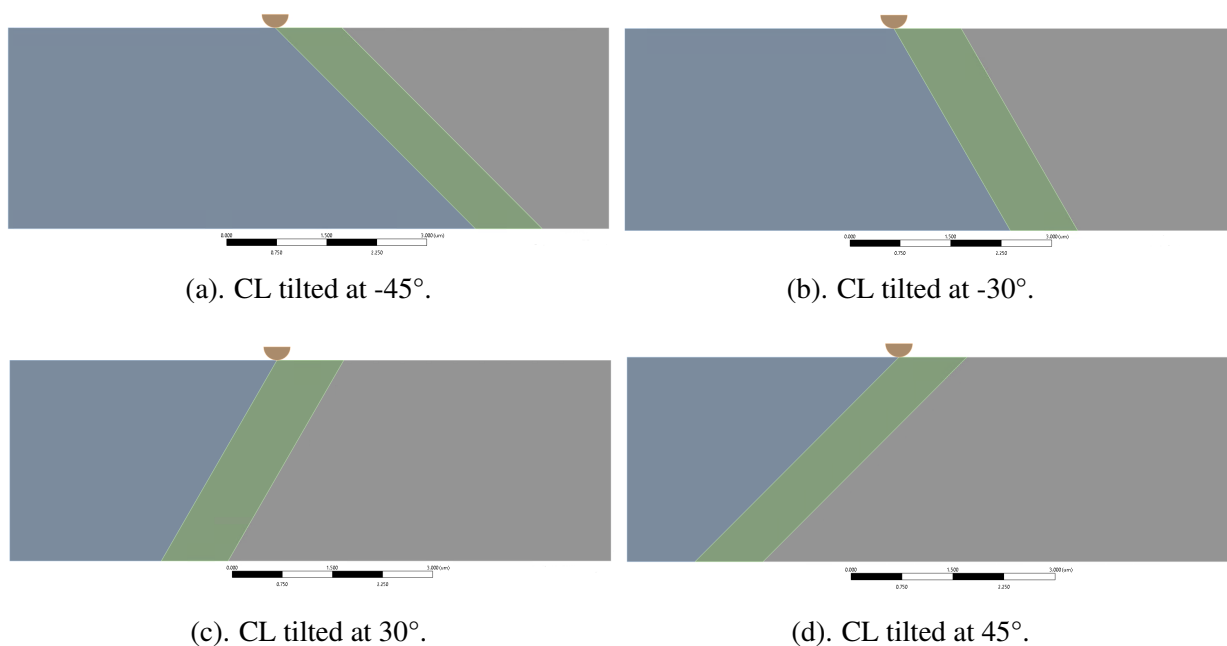
Figure 43: Different configurations of the CL tilted.

## ► MATERIALS PROPERTIES

Regarding the material properties, Table 8 presents the different values of Young's modulus and Poisson's ratio defined for each material. In this advanced study, the rectangular parallelepiped is composed of osteonal bone, the CL, and IB. For the CL, 3 values of Young's modulus were studied: 16 GPa, 22 GPa, and 24 GPa.

In the Section 3.1, it will be shown that the 2D simulations underestimate the actual $E_r$ value measured. To facilitate understanding, a reference value has been chosen. This reference value is a Young's modulus of 20 GPa. The other Young's modulus values will be expressed as a percentage relative to this reference value of 20 GPa.

The values of $E$ are based on the experimental results of Astrid Cantamessa [97], and the literature in general [52][98][99]. These values were chosen to correspond to experimental results and literature data. Given that the mechanical properties of the CL are poorly understood and often contradictory, the decision was made to test both soft and stiff values.

| Material | Young's modulus E [GPa] | Poisson's ratio $\nu$ [-] |
|---|---|---|
| Diamond | 1140 | 0.07 |
| Osteonal bone | 20 | 0.3 |
| Cement line | 16 - 22 - 24 | 0.3 |
| Interstitial bone | 28 | 0.3 |

Table 8: Materials properties.

## 2.7  Statistical testing

In the Sections 3.3.2 and 3.3.2 different groups are compared with each other by performing a one-way ANOVA. Significance levels were set at $p < 0.01$. The statistical analysis was performed in MATLAB. The p-value is a statistical indicator used to decide whether the null hypothesis is rejected or not. In a one-way ANOVA analysis, the null hypothesis assumes that all group means are equal. If the p-value set at $0.01$ is below the significance threshold, this means that the null hypothesis is rejected, suggesting significant differences between at least 2 of the groups. Conversely, if the p-value is above the significance threshold, this means that the null hypothesis is true, suggesting that no groups show significant differences.

# Chapter 3

# Results

This chapter aims to present the various results obtained during the simulations performed with the Ansys software. Initially, a comparative analysis of 2D and 3D simulations is conducted. Subsequently, the differences between the Hertz theoretical model and the 2D simulations are examined. Following this, an analysis is conducted on the position of the indenter along different materials. Finally, the impact of the inclination of the interfaces is studied.

## 3.1 Comparison: 2D and 3D simulations

For this section, the indenter penetrates the bone structure by $5\ nm$ to compare the results obtained from the 2D and 3D simulations.

### 3.1.1 Exploring elastic properties through Young's modulus

Figure 44 illustrates on the ordinate axis; the effective Young's modulus, $E_r$, measured in GPa, as a function of the position of the indenter, indicated on the abscissa axis. For better understanding, the position of the indenter is measured relative to the interface between the osteonal bone and the CL. The point at $0\ nm$ marks this interface. The Young's modulus assigned to the osteonal bone is 20 GPa, while that assigned to the CL is either 25 GPa or 30 GPa. The graph displays 4 curves representing the data obtained by 2 types of modeling: 3D and 2D plane strain. The yellow circle corresponds to the contact radius, equal to $32\ nm$ for an indenter penetration of $5\ nm$. The elastic modulus was calculated along the interface between these 2 materials. The curves differ by the values of Young's modulus (25 GPa or 30 GPa) of the CL and by the dimensionality (2D or 3D).

It is observable that the Young's modulus, $E_r$, varies depending on the position of the indenter in each configuration. As the indenter approaches the CL, whose stiffness is higher than that of the osteonal bone, the measured $E_r$ progressively increases. Thus, $E_r$ shows sensitivity to the position of the indenter. Furthermore, it is also noticeable that the curves tend to converge towards a stable value of Young's modulus, both to the left and right of the interface, i.e., as the position of the indenter moves away from the interface.

Moreover, a comparison illustrates the effects of setting the Young's modulus at 25 and 30 GPa for the CL. A modulus of 30 GPa results in a more pronounced increase in $E_r$, which is reflected by a steeper slope of the curves. Indeed, the pink curves show a more pronounced rise compared to the blue curves.

The green dotted lines illustrate $E_r$, calculated assuming an interaction of the indenter with a single homogeneous material in the 3D case. It should be noted these dotted lines for the 2D case are not available for comparison, as shown in the graphs following the blue dotted lines because they are obtained from simulations. From bottom to top, these blue dotted lines correspond respectively to homogeneous materials with an elasticity modulus of 20, 25, and 30 GPa. The 3D curves tend to converge towards these values depending on the position of the indenter. Particularly, when the indenter is positioned $100\ nm$ to the left of the interface, the

measured $E_r$ approaches the theoretical value for a homogeneous material of 20 GPa, which is the value assigned to the osteonal bone in the simulation for the material on the left.

A comparison can also be made between 2D and 3D simulations. Considering the curves for the 20-25 GPa configurations (and similarly for 20-30 GPa), the general trend remains similar, although the values of the calculated $E_r$ differ. Regarding computation time, the 3D simulation required 6 hours, while the 2D one was completely simulated in 20 minutes. Thus, the case with a cylindrical indenter is approximately 18 times faster than that with a spherical indenter. Moreover, the distinction between the 20-25 GPa and 20-30 GPa cases, both in 2D and 3D, shows differences. The 3D case shows a more marked disparity between the blue curve and the pink curve. For the 20-30 GPa configuration, Figure 44 indicates that at the interface, $E_r$ value reaches 27.97 GPa for the spherical indenter, versus 14.18 GPa for the cylindrical indenter, the latter representing 50.69% of the $E_r$ value obtained with the spherical indenter. This difference is relatively similar for each position.
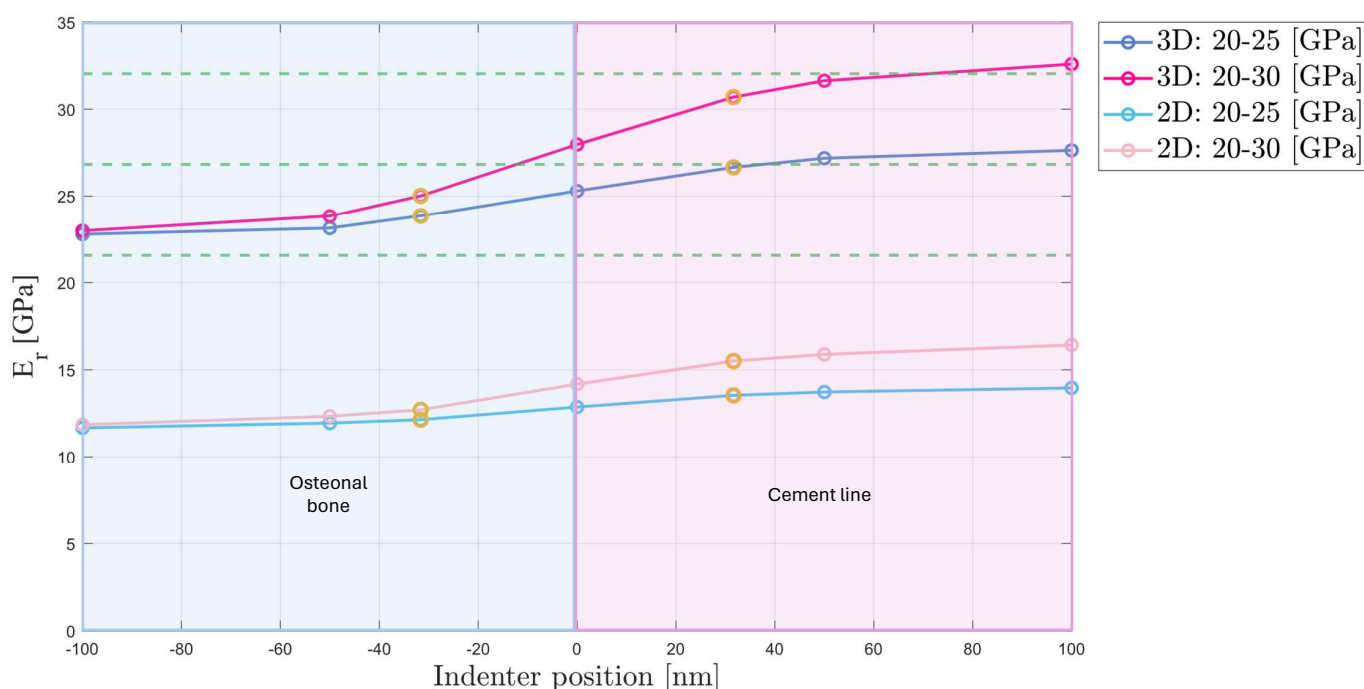


Figure 44: Comparison of the variation in $E_r$ measured in GPa as a function of the indenter position measured in $nm$ for a bone system with elastic modulus assigned as 20 GPa on the left and 25 or 30 GPa on the right for 2D and 3D simulations. The indenter positions range from $-100$ $nm$ to 100 $nm$ relative to the interface between the osteonal bone (on the left) and the CL (on the right). The yellow circles indicate the position of the contact radius during an indentation of 5 $nm$, equivalent to 32 $nm$. The green dashed lines correspond to the Young's modulus obtained for an interaction between a homogeneous material and a diamond. From bottom to top, these dotted lines represent a homogeneous material of 20, 25, and 30 GPa.

It should be noted that the Young's modulus obtained for the 3D simulation is calculated based on the Oliver and Pharr method but can also be calculated using the Hertz model. The values obtained from the 2 theoritical models are relatively similar. A comparison between the 2 methods is presented in Appendix A, Figure 61.

### 3.1.2 Qualitative analysis of Von Mises stress

Figure 45 illustrates the distribution of Von Mises stress in the model when the indenter is located at the interface between the osteonal bone, with an elasticity modulus of $20$ GPa, and the CL, with a modulus of $25$ GPa. In the 3D case, the stress distribution appears more complex while the extent of the stresses is broader in the 2D case. Visually, the representation of stress, colored, extends deeper in the 2D model than in the 3D model. Furthermore, a discontinuity at the stress level is observed at the interface. Indeed, stress values are higher on the CL side, due to its higher elastic modulus.

In Figure 45, the second column presents a comparison of the distribution of Von Mises stresses in 3D and 2D when the indenter is placed $100$ $nm$ to the right of the interface. In both models, the stress distribution shows no discontinuity caused by the interface. At this distance, the influence of the interface no longer manifests on the distribution. This absence of discontinuity can be correlated with Figure 44, which shows a convergence of $E_r$ towards the value corresponding to a homogeneous material with an elasticity modulus of $25$ GPa.
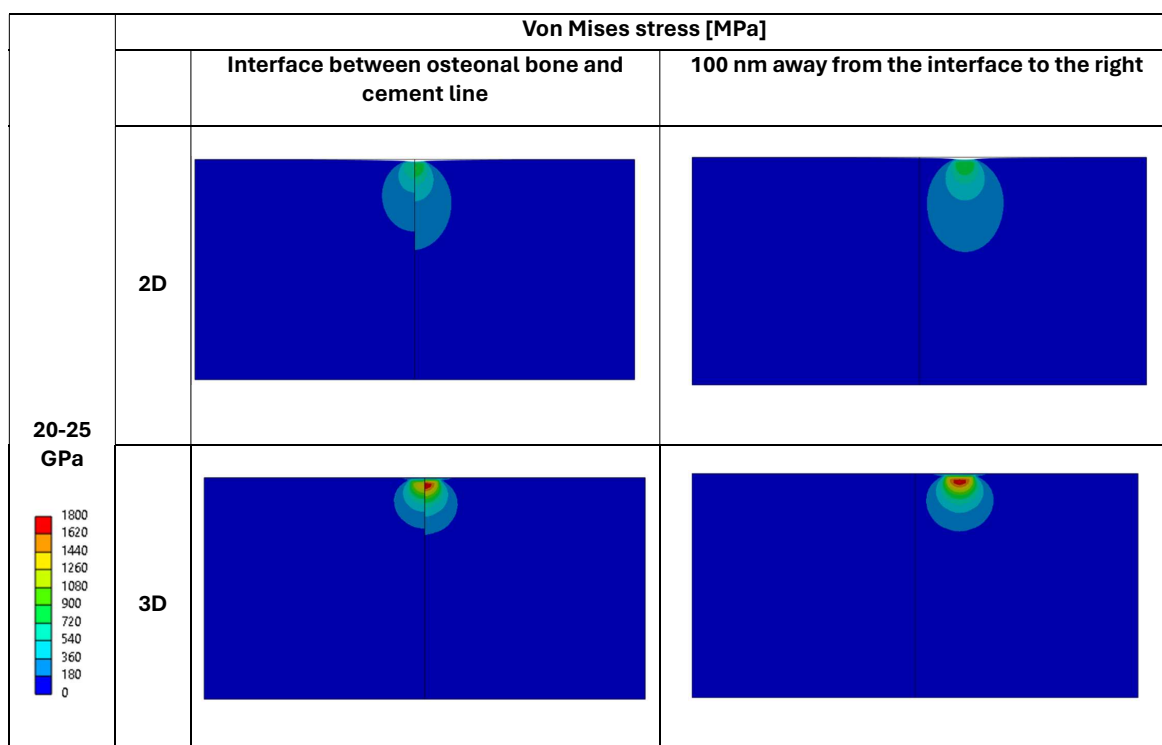


Figure 45: Comparison of the Von Mises stress distribution in a bone system composed of an osteonal bone of $20$ GPa on the left and a CL of $25$ GPa on the right for 2D and 3D simulations. The Von Mises stress is measured in MPa. 2 indenter positions are illustrated: at the interface between the osteonal bone and $100$ $nm$ to the right of the interface.

## 3.2 Comparison: Hertz and simulation in 2D

Figure 46 compares the load versus the displacement curve obtained from the Hertz theoretical model and the data extracted from the simulation. To determine the reaction force in the Hertz model, Equation 1.15 was used. As this equation takes into account the out-of-plane model length, it is fixed at $1$ $\mu m$. The depth in the equation corresponds to the same vector generated

during the simulation, resulting in $150\ nm$. The Young's modulus used is that obtained during the interaction between diamond and a homogeneous material of 20 GPa, as described in Equation 1.9. Regarding the simulation curve, the reaction force is directly extracted, as it is directly calculated. It is observable that both curves are linear, although the slope of the Hertz curve is more pronounced than that of the simulation, indicating that the simulation underestimates the reaction force compared to the Hertz model. The values obtained by Hertz are approximately twice those of the simulations.
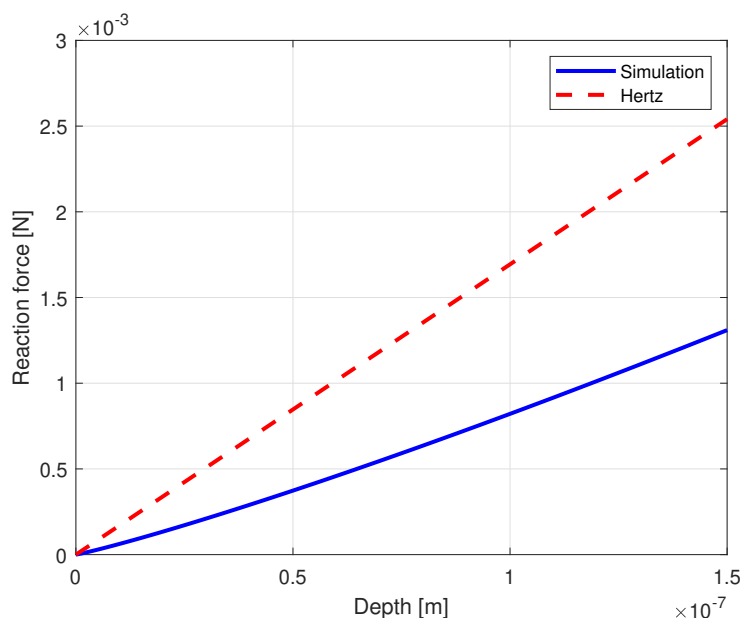


Figure 46: Comparison of the reaction force measured in N as a function of depth measured in $m$ for a 2D plane strain simulation and a theoretical Hertz model of the contact between 2 cylinders with parallel axes.

## 3.3 Placement of the tip across 3 different materials

For future sections, the indenter penetrates the bone structure by $150\ nm$ in all simulations performed. This penetration is chosen to match the experiments carried out by Astrid Cantamessa.

### 3.3.1 2D Young's modulus simulation for homogeneous materials

As mentioned previously, simulations performed in 2D tend to underestimate the value of $E_r$ that should be obtained. To quantify this underestimation, various simulations were conducted using a homogeneous model composed of a single material. The properties used for the homogeneous material are listed in the first column of Table 9, with Young's modulus of $16, 20, 22, 24$, and $28$ GPa. The values obtained for $E_r$ in 2D are presented in the second column and are consistently lower than the values initially assigned to the material. The 2D model thus shows an underestimation of the Young's modulus. For example, when a Young's modulus of 20 GPa is assigned to the material, the value obtained in the 2D simulation is only $11.55$ GPa.

These values are important, as in subsequent analyses, inhomogeneity is explored using 3 materials with distinct properties. The Young's modulus values obtained in 2D will serve as refer-

ences. This will make it possible, both visually and quantitatively, to determine the proximity or divergence of the Young's modulus values obtained relative to these reference values, depending on the position of the indenter tip.

To facilitate the understanding of the material properties assigned to different materials (CL, osteonal bone, and IB) upon the introduction of inhomogeneity, the various Young's modulus values have been designated by specific names. For example, the value of 20 GPa has been defined as the reference value, noted as "Ref". All other values are named in reference to this baseline value. Thus, the value of 16 GPa is named "Ref-20%" because it is 20% lower than 20 GPa. The designations for each of the Young's modulus values are also presented in Table 9.

| Young's modulus [GPa] | Young's modulus obtained in 2D [GPa] |
|---|---|
| 16 (Ref-20%) | 9.25 |
| 20 (Ref) | 11.55 |
| 22 (Ref+10%) | 12.69 |
| 24 (Ref+20%) | 13.84 |
| 28 (Ref+40%) | 16.12 |

Table 9: Comparison of $E_r$ assigned to a homogeneous material, in GPa, with those obtained from 2D simulations.

### 3.3.2 Exploring elastic properties of inhomogeneous materials via Young's modulus

2 configurations of material inhomogeneity have been chosen to study the 2 configurations in which CLs are found in reality (either between 2 osteons or between osteon and IB):

1. In the first configuration, an osteon is placed on the left, the CL in the center, and another osteon on the right.

2. In the second configuration, an osteon is placed on the left, the CL in the center, and the IB is located on the right.

Figure 47 illustrates the evolution of $E_r$ measured according to the position of the indenter as it traverses 3 different materials, in order: osteonal bone, the CL, and again osteonal bone. An estimation based on vertical orthogonal symmetry through the midpoint of the CL was applied to the blue, orange, and purple curves to show their behavior if indentation had also occurred at the right interface. This extrapolation is represented by dashed curves, thus extending the expected behavior of the curves.

Figure 50 illustrates the evolution of $E_r$ measured according to the position of the indenter as it traverses 3 different materials, in order: osteonal bone, the CL, and IB.

The graph shows specific positions on the $x$-axis related to the placement of the indentation: at the interfaces between osteonal bone and the CL, named "interface 1", and between the CL and the IB, named "interface 2". An indentation was also made in the middle of the CL. All other indentation positions were performed based on the contact radius, noted as $R_c$, relative

to the interfaces. The indices $1$ and $2$ in the notation, for example $-1R_{c_1}$ and $+2R_{c_2}$, indicate a distance of once the contact radius to the left of "interface 1" and twice the contact radius to the right of "interface 2", respectively. On the graph, the positions corresponding to once the contact radius to the left and right of each interface are highlighted in yellow.

The blue dotted lines on the graph represent $E_r$ obtained for 2D simulations, using a homogeneous material with elastic modulus of $16, 20, 22,$ and $24$ GPa, from bottom to top respectively for Figure 47 and $16, 20, 24,$ and $28$ GPa, from bottom to top respectively for Figure 50. The values of Young's modulus thus obtained in 2D simulation correspond to those previously indicated in the second column of Table 9.

On these $2$ graphs, $5$ curves are represented, as they correspond to $4$ different configurations. Indeed, each curve illustrates a unique combination of elastic modulus for the $3$ materials involved.

Initially focusing on Figure 47, the analysis of the behavior of the different curves is explained below:

1. Purple curve (Ref | Ref-20% | Ref):
   This curve represents the configuration where both the osteonal bone and the IB are assigned the reference value, while the CL has an elastic modulus $20\%$ lower than this reference. The $E_r$ decreases as the indenter moves towards the CL, which is less rigid, reaching a minimum in the middle of it at $500$ $nm$. The reduction in $E_r$ is particularly rapid near the interface. However, at the ends of the curve, either at $3$ times the contact radius and in the middle of the CL, the curve converges to the expected value for a completely homogeneous material, as indicated by the second dotted blue line from the bottom on the graph. In the middle of the CL, it can be seen that $E_r$ is over-estimated.

2. Orange curve (Ref | Ref+10% | Ref):
   In this configuration, the CL has a Young's modulus that is $10\%$ higher than the reference value assigned to the osteonal bone and the IB. The increase in $E_r$ occurs more gradually compared to the other $2$ curves. The convergence to the expected value, as the indenter moves away from the interface and penetrates into the osteonal bone, is better than in other configurations; the value obtained at $3$ times the contact radius almost coincides with the dotted blue line. However, when the indenter is in the middle of the CL, the measured $E_r$ is underestimated compared to the expected value for a homogeneous material. Nevertheless, the gap between the obtained value and the expected value is the smallest among the $3$ curves.

3. Blue curve (Ref | Ref+20% | Ref):

This curve corresponds to the configuration where the CL has an elastic modulus $20\%$ higher than the reference value. An increase in $E_r$ is observed as the indenter moves towards the CL. The convergence of $E_r$, as the indenter moves away from the CL to the left, tends towards the value corresponding to a homogeneous material. The modulus obtained is slightly higher than that observed for the orange curve. Near the interface, the increase in $E_r$ is more abrupt compared to that of the orange curve. Regarding the value obtained in the middle of the CL, it is underestimated compared to the expected value for a homogeneous material.

Figure 47: Variation of the $E_r$ measured in GPa as a function of the indenter position measured in $nm$ for a bone system with 3 different configurations of elastic modulus assignments for 2D simulations. The indenter positions range from $-3R_{c_1}$ to $3R_{c_2}$ relative to the interfaces: osteonal bone (on the left) - CL (in the middle) and CL and IB (on the right). The yellow circles indicate the position of the contact radius during an indentation of $150\ nm$, equivalent to $173\ nm$. The blue dashed lines correspond to the Young's modulus obtained for an interaction between a homogeneous material and a diamond during 2D simulations. From bottom to top, these lines represent a homogeneous material of $16, 20, 22,$ and $24$ GPa.

The analysis can focus on 2 particular curves: the blue curve and the purple curve. These 2 curves were chosen to examine the impact of modifying the material properties of the CL, made $20\%$ softer (purple curve) and $20\%$ stiffer (blue curve) than its environment. In Figure 47, these 2 curves show orthogonal symmetry. Indeed, they exhibit opposite but symmetrical responses relative to the positioning of the indenter. However, as shown in Figure 48, the orthogonal symmetry is not observed at the reference line, where the Young's modulus equals "Ref", but slightly below it. Figure 49 illustrates the percentage difference calculated relative to the Young's modulus obtained at the first position, $-3R_{c_1}$, for each configuration (blue curve and purple curve). The 2 curves on this figure almost perfectly overlap, revealing the presence of

symmetry. Nevertheless, with the axis of symmetry located slightly below the reference line, it is more accurate to say that the 2 curves exhibit slight asymmetry relative to this reference line.
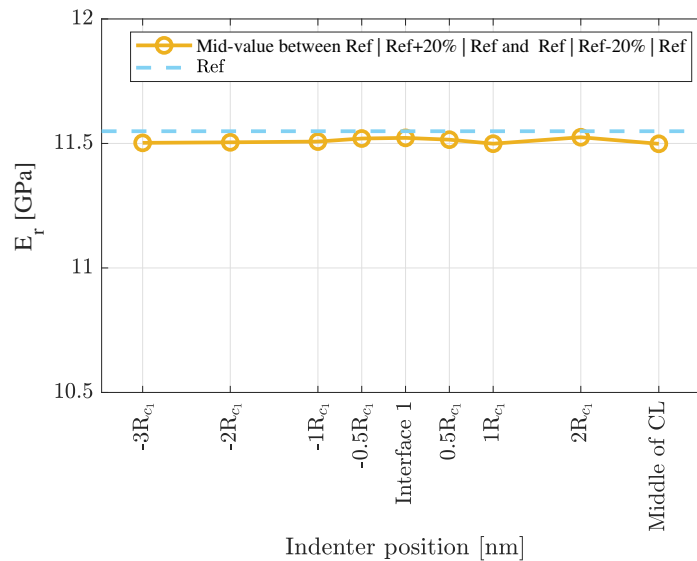


Figure 48: Comparison of average Young's modulus between 2 configurations and a homogeneous material with Young's modulus equal to "Ref".
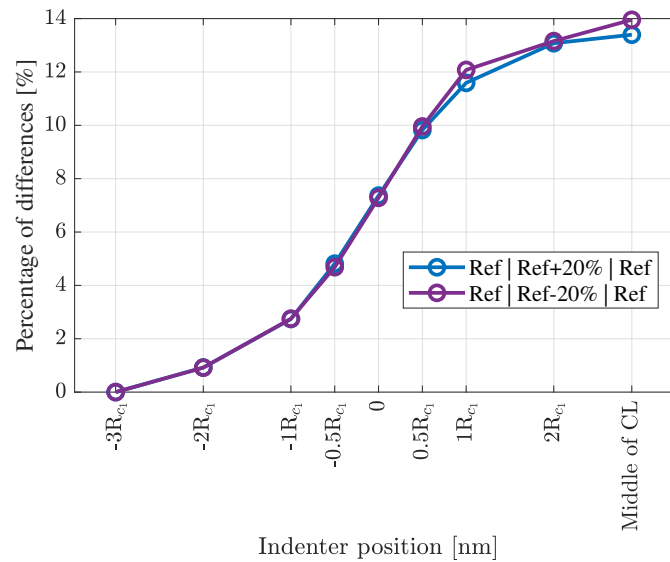


Figure 49: Comparison of the variation in percentage differences in % as a function of the indenter position measured in $nm$ for a bone system with 2 different configurations of elastic modulus assignments for 2D simulations.

The behavior of the curves for asymmetric configurations of the material properties of the bone structure is explained below:

1. Burgundy curve (Ref | Ref-20% | Ref+40%):
   In this configuration, the CL is the least rigid material, with a Young's modulus 20%

lower than that of the osteonal bone. The IB, on the other hand, has a Young's modulus that is $40\%$ higher than that of the osteonal bone. Starting from the position $-3R_{c_1}$, as the indenter moves towards the CL, the measured Young's modulus decreases, reaching a minimum in the middle of the CL. From there, as it moves towards $3R_{c_2}$, $E_r$ increases rapidly without reaching it.

2. Green curve (Ref | Ref+20% | Ref+40%):
   The CL has an elastic modulus $20\%$ higher than that of the osteonal bone, which has a Young's modulus equal to the reference value. On the other hand, the IB has a Young's modulus $40\%$ higher than this same reference value. Unlike other configurations, in this case, $E_r$ continuously increases as the indenter approaches the more rigid IB. In the middle of the CL, the obtained value is almost the same as the expected value for a homogeneous material.
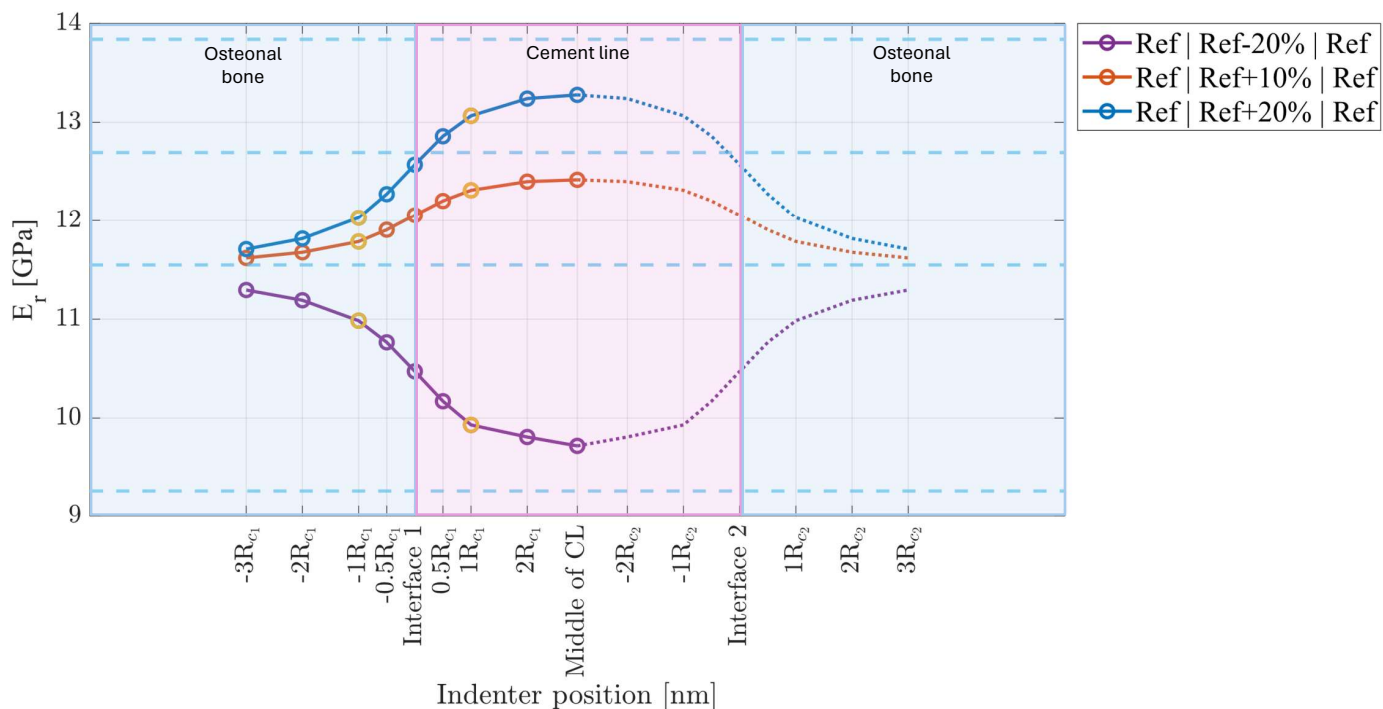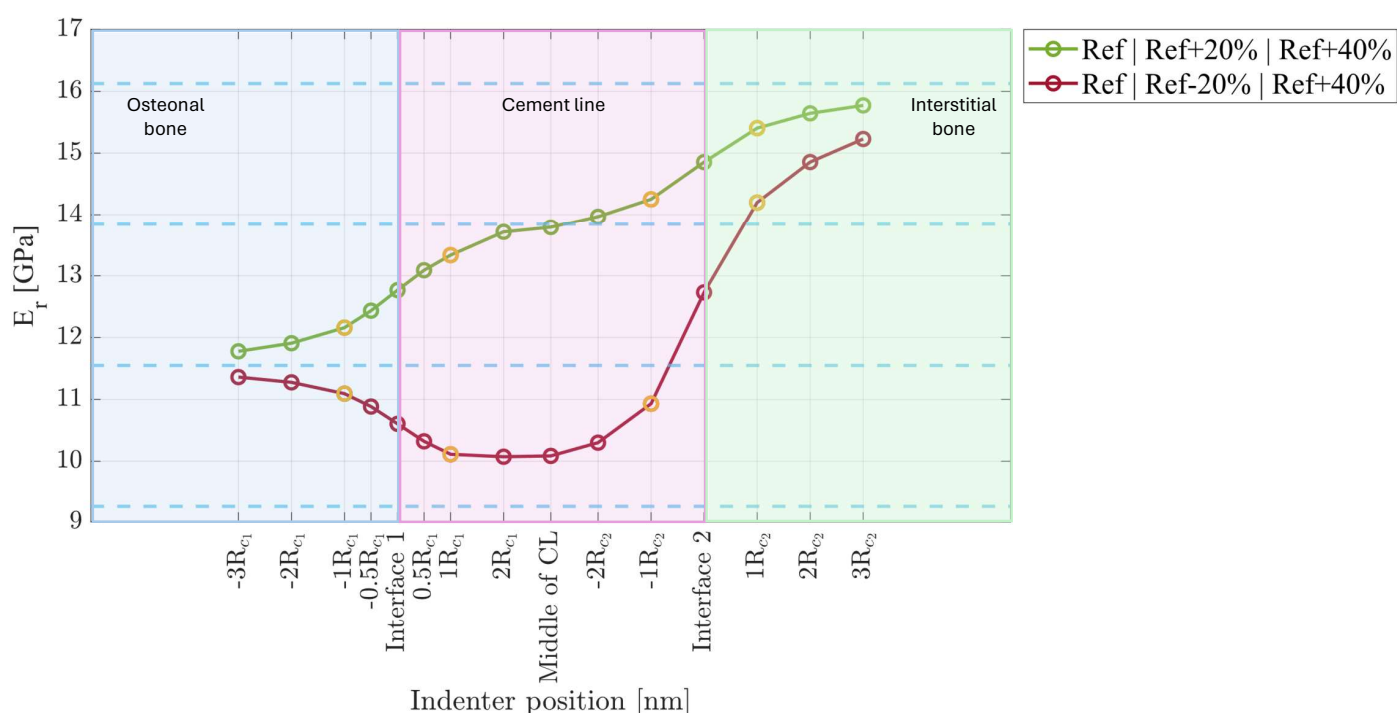


Figure 50: Variation of $E_r$ measured in GPa as a function of the indenter position measured in $nm$ for a bone system with 2 different configurations of elastic modulus assignments for 2D simulations. The indenter positions range from $-3R_{c_1}$ to $3R_{c_2}$ relative to the interfaces: osteonal bone (on the left) - CL (in the middle) and CL and IB (on the right). The yellow circles indicate the position of the contact radius during an indentation of $150\ nm$, equivalent to $173\ nm$. The blue dashed lines correspond to the Young's modulus obtained for an interaction between a homogeneous material and a diamond during 2D simulations. From bottom to top, these lines represent a homogeneous material of $16, 20, 24$, and $28$ GPa.

An analysis of the slopes was performed during the phases of the indenter's approach and movement away from the interfaces. These slopes were calculated only between once the contact radius to the left of the interface and once the contact radius to the right, thus covering a total distance of $346\ nm$. Between these 2 points, marked in yellow, the curves can be approximated by a straight line, which allows for the determination of the slope. This slope

provides a quantitative measure to compare the rate of change of the Young's modulus for each configuration. To calculate the slope, Equation 3.16 was used,

$$\Delta = \frac{\Delta y}{\Delta x}, \tag{3.16}$$

with $\Delta$ representing the slope, $\Delta y$ the change in the measured Young's modulus in GPa, and $\Delta x$ the displacement of the indenter measured in $nm$, which is equal to $346\ nm$.

Table 10 presents the calculated slopes from $-R_{c_1}$ to $R_{c_1}$ for the different configurations. A negative slope indicates that the Young's modulus decreases, suggesting a less rigid material at the interface. Conversely, a positive slope indicates a transition from a less rigid to a more rigid phase. The slope with the smallest absolute value corresponds to the configuration "Ref | Ref+10% | Ref", and is equal to $0.0015$ GPa/$nm$. The slope with the highest absolute value is observed for the configuration, "Ref | Ref+20% | Ref+40%", reaching $0.0034$ GPa/$nm$. The configurations "Ref | Ref-20% | Ref" and "Ref | Ref+20% | Ref" show identical slopes in absolute value but of opposite sign. It is noteworthy that for the configurations with osteonal bone followed by the CL followed by an osteonal bone, when the Young's modulus value of the CL is "Ref+20%", the slope is twice as high as when it is "Ref+10%".

| Configuration | Slope from $-R_{c_1}$ to $R_{c_1}$ |
|---|---|
| Ref \| Ref-20% \| Ref | -0.0030 |
| Ref \| Ref+10% \| Ref | 0.0015 |
| Ref \| Ref+20% \| Ref | 0.0030 |
| Ref \| Ref-20% \| Ref+40% | -0.0028 |
| Ref \| Ref+20% \| Ref+40% | 0.0034 |

Table 10: Comparison of the slopes of the curves in Figures 47 and 50 from $-R_{c_1}$ to $R_{c_1}$.

Table 11 lists the measured slopes from $-R_{c_2}$ to $R_{c_2}$ for the configurations exhibiting asymmetry in the bone structure. The highest slope is observed in the configuration, "Ref | Ref+20% | Ref+40%", and amounts to $0.0094$ GPa/$nm$.

| Configuration | Slope from $-R_{c_2}$ to $R_{c_2}$ |
|---|---|
| Ref \| Ref-20% \| Ref+40% | 0.0034 |
| Ref \| Ref+20% \| Ref+40% | 0.0094 |

Table 11: Comparison of the slopes of the curves in Figure 50 from $-R_{c_2}$ to $R_{c_2}$.

In order to establish quantitative measures of the differences between the various configurations, a percentage difference calculation was performed for each material. For the osteonal bone, the percentage difference was determined at each indenter position for each curve by comparing the measured $E_r$ with the reference value expected for a homogeneous material. This process was systematically applied when the indenter was within each analyzed material: the osteonal bone, the CL, and the IB. For each curve, the percentage difference relative to the corresponding reference line was calculated.

When the indenter is in the osteonal bone, Figure 51(a) illustrates the percentage error between the measured $E_r$ and the value expected for a homogeneous material. A negative percentage difference indicates that $E_r$ underestimates the material properties, while a positive percentage indicates an overestimation. The graph shows that at 3 times the contact radius to the left, there is still an error in the Young's modulus value. The highest error in absolute value, $-2.2\%$, corresponds to the configuration, "Ref | Ref-20% | Ref". When the indenter is placed at one contact radius to the left, the percentage difference does not exceeds $5\%$ for all configurations except "Ref | Ref+20% | Ref+40%" with a deviation of $5.2\%$. When the indenter is at the interface between the osteonal bone and the CL, the percentage differences are high because the indenter is in contact with 2 different materials. The highest percentage difference, $10.5\%$, is observed for the configuration "Ref | Ref+20% | Ref+40%". An additional observation is the notable difference that manifests between the blue curve and the green curve. Although these 2 curves have the same configuration for the osteonal bone and the CL, the difference comes from the third material on the right, which is osteonal bone for the blue curve and IB for the green curve. This difference influences the measured values in the osteonal bone region on the left.

Figure 51(b) shows the percentage differences when the indenter is positioned in the CL. Unlike the osteonal bone, where all curves share the same Young's modulus value, each curve has a different assigned Young's modulus for the CL, so the percentage difference is calculated relative to the expected value for a homogeneous material, adapted to each configuration. In this case, the percentage differences are relatively high. For example, when the indenter is in the middle of the CL, the percentage difference ranges from $-2.2\%$ for the configuration "Ref | Ref+10% | Ref" to $9.3\%$ for "Ref | Ref-20% | Ref+40%". At the interfaces, high percentage errors are also observed. At "interface 1", the configurations "Ref | Ref-20% | Ref+40%" and "Ref | Ref-20% | Ref" show the largest discrepancies, with an overestimation of the expected value by $17.6\%$ for the former and an underestimation by $13.2\%$ for the latter. At "interface 2", the percentage differences of "Ref | Ref-20% | Ref+40%" and "Ref | Ref+20% | Ref+40%" are $11.3\%$ and $0.9\%$ respectively. However, for these 2 configurations, the minimal difference tends to approach $0\%$ only when the indenter is positioned at a distance of $-1R_{c_2}$.

Figure 51(c) displays the percentage differences when the indenter is in the IB, only for the configurations "Ref | Ref-20% | Ref+40%" and "Ref | Ref+20% | Ref+40%". When the indenter is at "interface 2", both configurations underestimate the expected $E_r$ value, with underestimations of $-21\%$ for the configuration "Ref | Ref-20% | Ref+40%" and -8% for "Ref | Ref+20% | Ref+40%. Further away from the interface, at one contact radius, the percentage differences are -12% and -4% respectively for the 2 configurations. At 3 times the contact radius, the underestimation is more pronounced in the configuration "Ref | Ref-20% | Ref+40%", with a discrepancy of -5.5%, compared to -2.2% for "Ref | Ref+20% | Ref+40%".
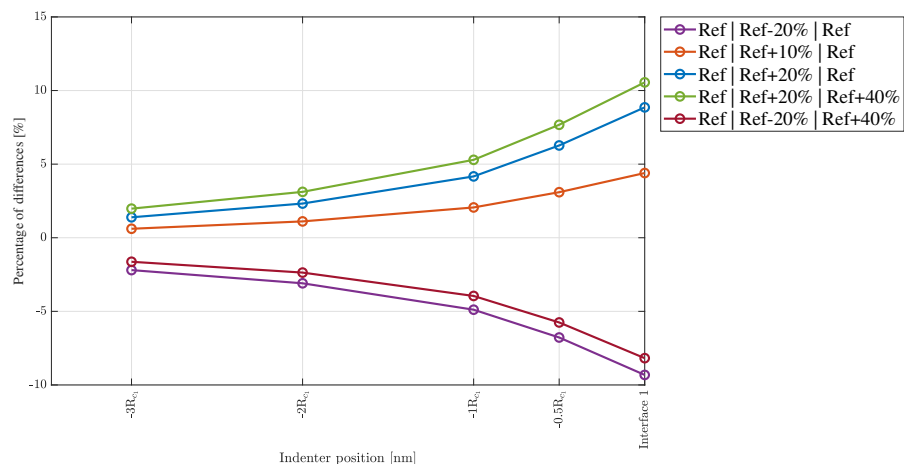
(a). Osteonal bone.
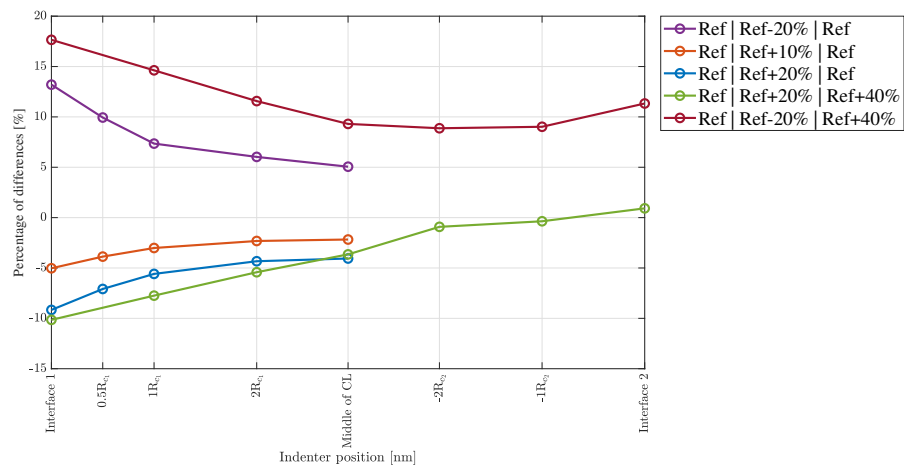


(b). Cement line.
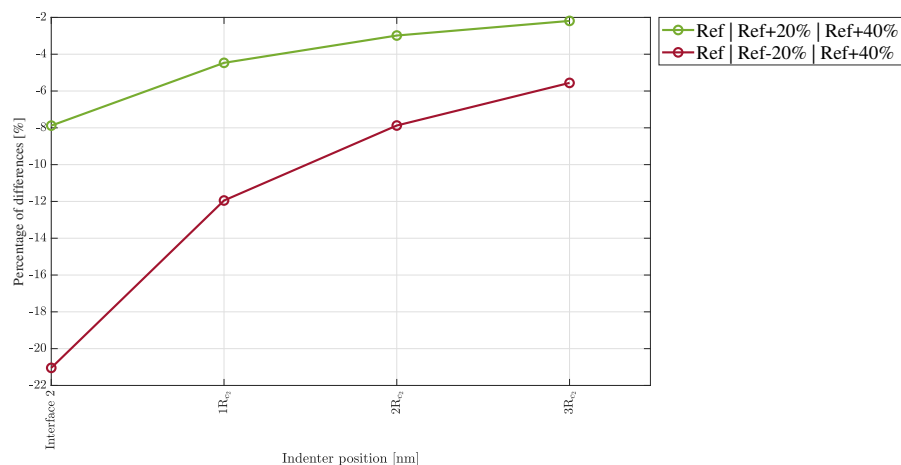


(c). Interstital bone.

Figure 51: Comparison of the variation in percentage differences in % as a function of the indenter position measured in $nm$ for a bone system with different configurations of elastic modulus assignments for 2D simulations.

In Figures 52(a), 52(b) and 52(c), normalized boxplots present the difference between the Young's modulus measured at each position and the expected value (the value measured in the homogeneous material) for the osteonal bone, the CL, and the IB respectively. This normalization allows for a comparison between the different simulated configurations, providing insight into the deviation from the expected value as well as the induced variability.

These results show significant variability depending on the configurations. For example, the configuration "Ref | Ref+10% | Ref" is significantly different from all other configurations in the osteonal bone ($p < 0.01$). In the osteonal bone, the configuration "Ref | Ref+20% | Ref+40%" is significantly different from all groups except for the configuration "Ref | Ref+20% | Ref". Visually and statistically, in the same zone, the configuration "Ref | Ref-20% | Ref" is not significantly different from the configuration "Ref | Ref-20% | Ref+40%" only.

In the CL, it is more complicated to visually distinguish significant differences. The one-way ANOVA analysis shows that the configuration "Ref | Ref+10% | Ref" is significantly different from the configuration "Ref | Ref-20% | Ref" and "Ref | Ref-20% | Ref+40%" only (($p < 0.01$). The values of this configuration result in values close to $0$ in the box plots in the osteonal bone and the CL, as well as a narrow range of values. This observation can be correlated with its low standard deviations, $0.17$ GPa in the osteonal bone and $0.15$ GPa in the CL. This indicates that this configuration provides the best approximation of the expected value. The means of the configuration "Ref | Ref-20% | Ref+40%" and "Ref | Ref+20% | Ref+40%" are significantly different. The configuration "Ref | Ref-20% | Ref+40%" is significantly different from all groups except for the configuration "Ref | Ref-20% | Ref".

In the IB, the configuration "Ref | Ref-20% | Ref+40%" shows the highest standard deviation of $1.1$ GPa but is not significantly different from "Ref | Ref+20% | Ref+40%". Additional information regarding the mean and standard deviation for each of the configurations in each zone is provided in Appendix B, in Tables 15, 16, and 17.

(a). Osteonal bone.



(b). Cement line.



(c). Interstitial bone.
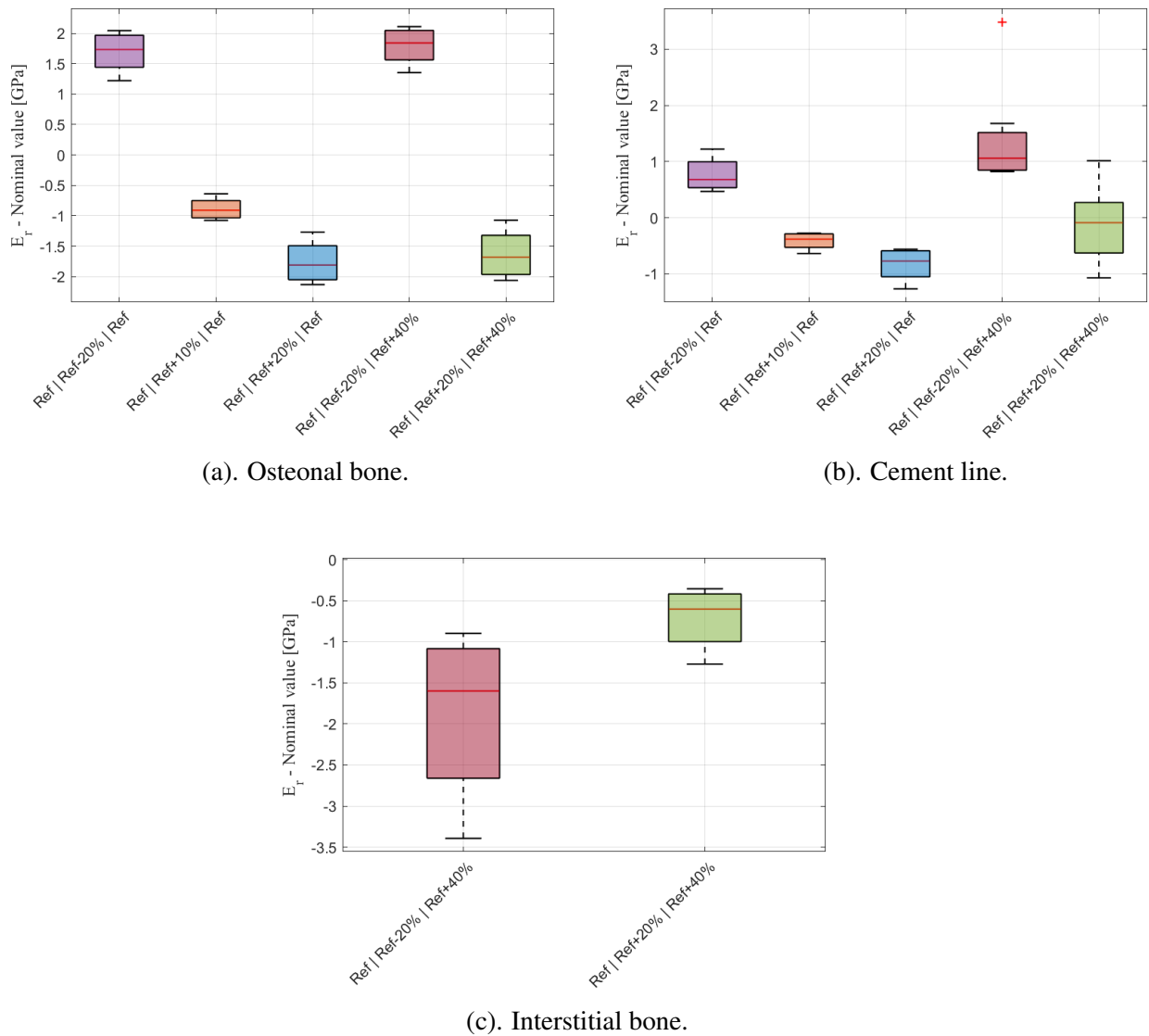
Figure 52: Boxplots representing the variability of the normalized Young's modulus for different configurations in the different regions.

### 3.3.3 Qualitative analysis of Von Mises stress

Figures 53, 54, and 55 illustrate the distribution of Von Mises stress for the configurations, "Ref | Ref+20% | Ref", "Ref | Ref+20% | Ref+40%", and "Ref | Ref-20% | Ref+40%" respectively. The different captures show the stress distributions at various indenter positions. For the configuration with 2 osteons framing the CL, 6 positions were selected, ranging from $-R_{c_1}$ to the middle of the CL. For the other configurations, comprising an osteonal bone on the left and an IB on the right of the CL, 9 positions were chosen, ranging from $-3R_{c_1}$ to $3R_{c_2}$. A color scale is used to represent the intensity of the Von Mises stress, ranging from $0$ to $6000$ MPa. The colors range from dark blue, indicating low stress, to red, indicating high stress. The color scale is the same for each image to allow consistent comparisons. The images show only the bone structure, without the indenter, and depict the bone structure in an undeformed state.

Figure 53 shows a higher concentration of stress near the contact with the indenter, propagating with a decreasing gradient from warm to cool colors. As we move away from the contact point,

the stress decreases. At positions $-3R_{c_1}$ and $-1R_{c_1}$, where the indenter is placed to the left of the interface, the stress remains high around the indenter but extends partially into the CL. When the indenter is at the interface, the stress distribution is visible on both sides of this interface, with higher intensity on the CL side. This stress propagation extends more into the CL as the indenter moves towards the middle of the CL. In the middle of the CL, the stress distribution extends beyond both interfaces, with stress values reaching approximately $1000$ MPa at the interfaces.

In Figure 54, the observed stress is also low at the interface when the indenter is far away, at $-3R_{c_1}$ and $3R_{c_2}$. At the interfaces, the stress discontinuity is clearly marked, with less pronounced stress propagation in the material with the lowest Young's modulus. Unlike the configuration "Ref | Ref+$20\%$ | Ref", the stress distribution is asymmetrical when the indenter is in the middle of the CL. Indeed, greater stress propagation occurs on the IB side compared to the osteonal bone side.

In Figure 55, $9$ indenter positions are illustrated for the configuration, "Ref | Ref-$20\%$ | Ref+$40\%$". In this configuration, the stress concentration is the highest when the indenter is in the IB, with a red color under the indenter indicating the highest stress values. This configuration stands out from the other $2$ because there is a more pronounced reduction in stress propagation in the CL compared to the propagation of stress in the osteonal bone. This difference in stress propagation is even more visible as the indenter approaches the IB. In general, the higher the Young's modulus, the higher the stress concentration will be.
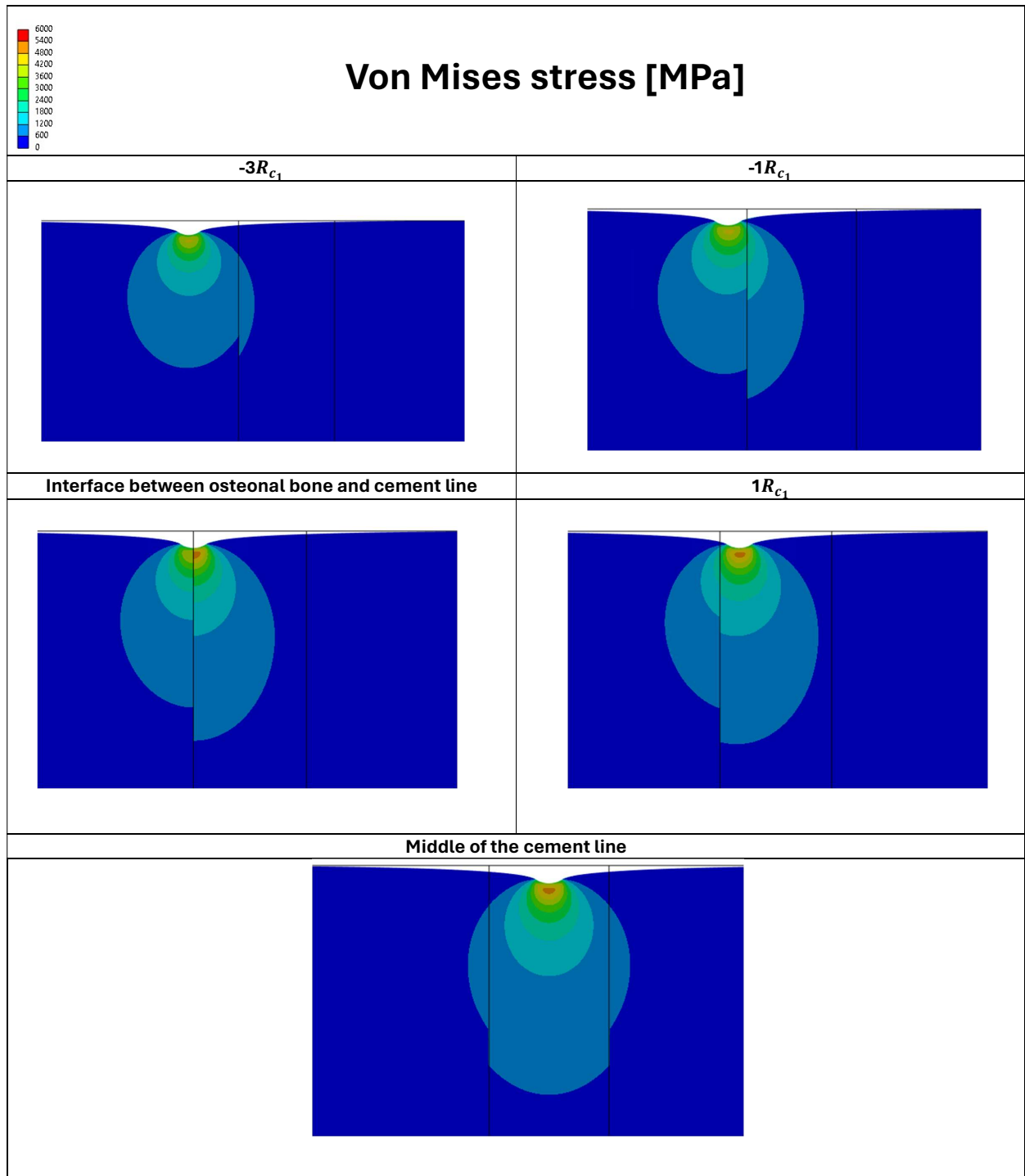
Figure 53: Comparison of the Von Mises stress distribution in a bone system composed of an osteonal bone of 20 GPa on the left, a CL of 24 GPa in the middle, and an osteonal bone of 20 GPa on the right for 2D simulations. The Von Mises stress is measured in MPa. 5 indenter positions are illustrated.
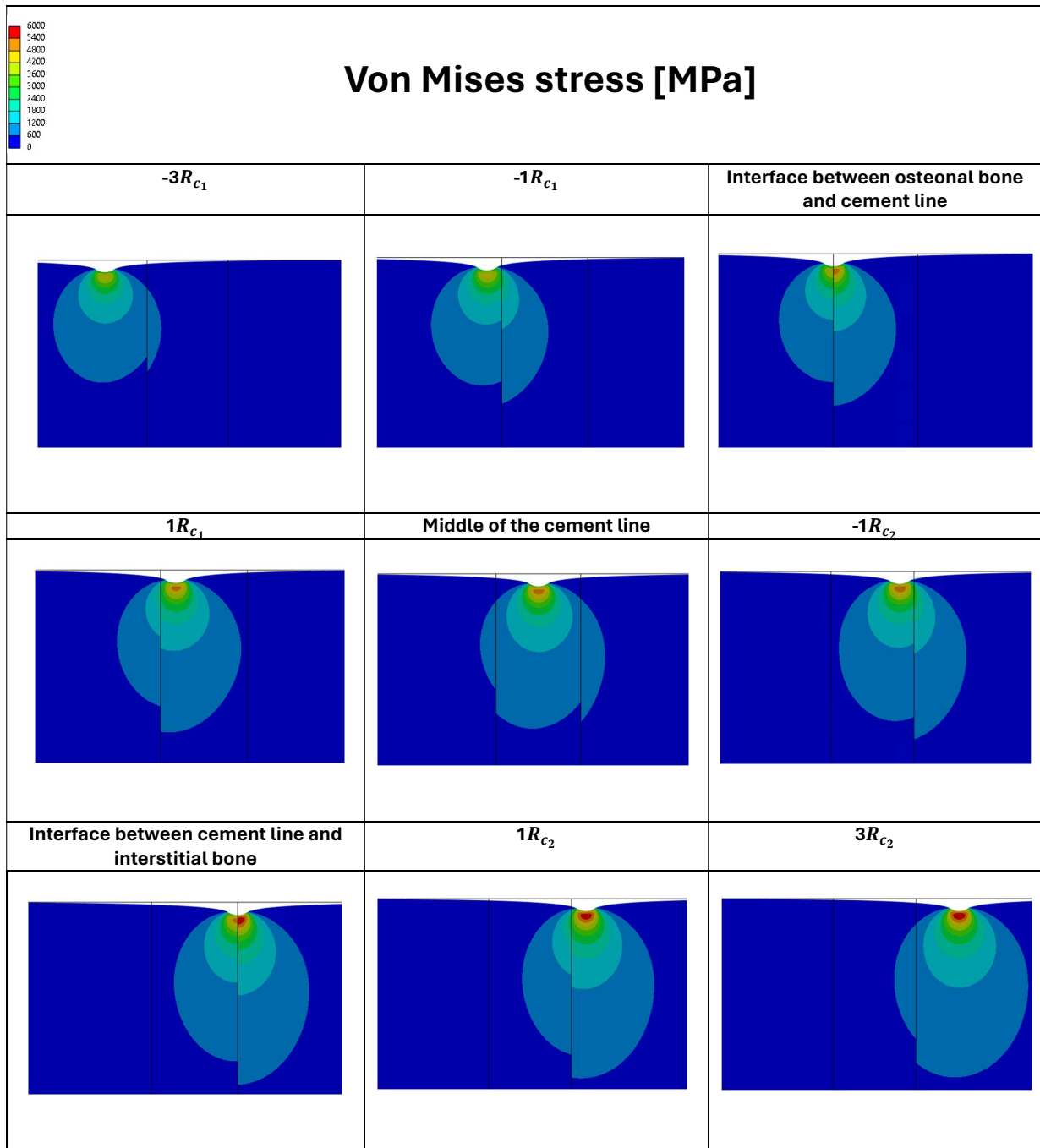
Figure 54: Comparison of the Von Mises stress distribution in a bone system composed of an osteonal bone of 20 GPa on the left, a CL of 24 GPa in the middle, and an IB of 28 GPa on the right for 2D simulations. The Von Mises stress is measured in MPa. 9 indenter positions are illustrated.
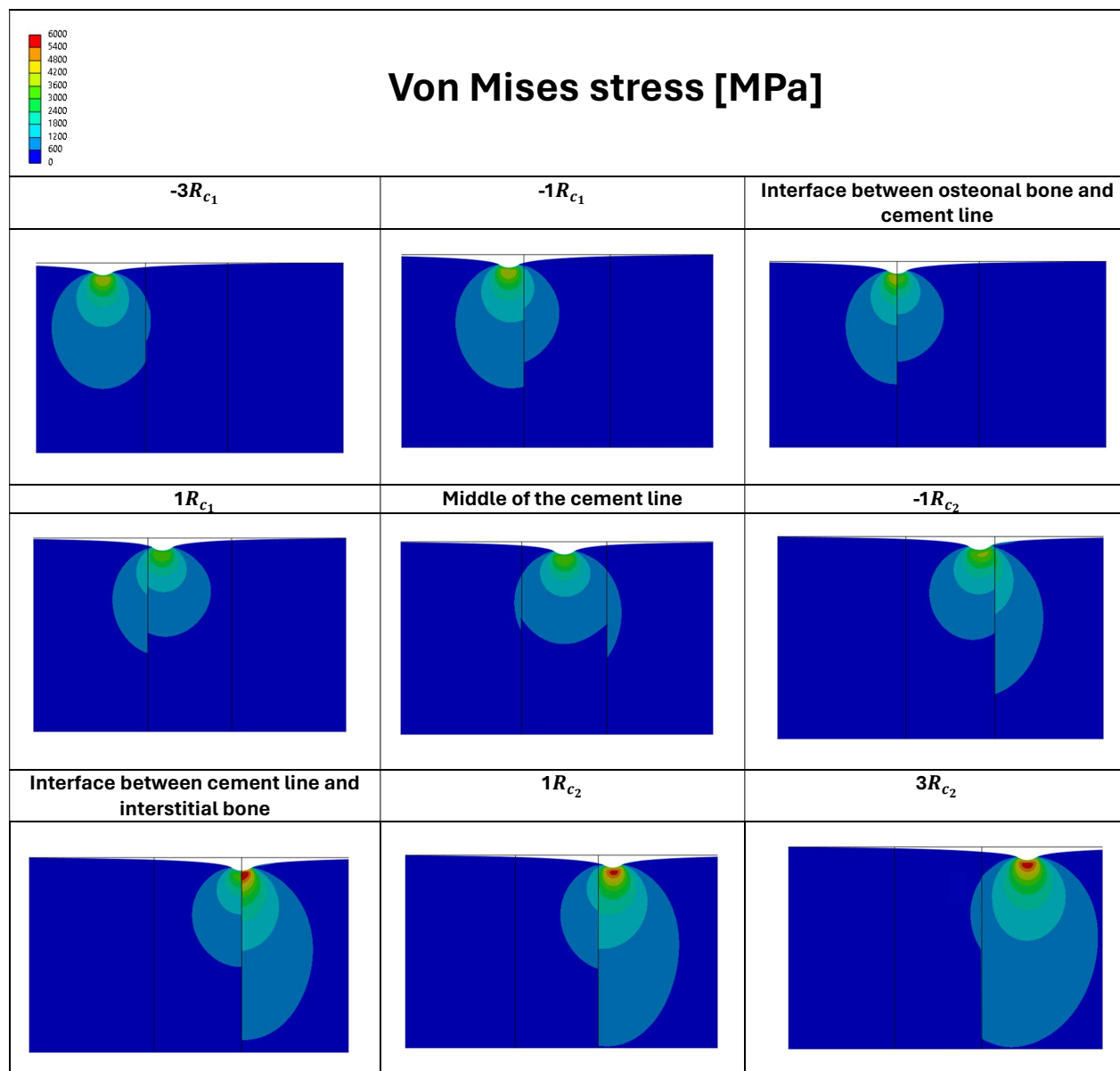
Figure 55: Comparison of the Von Mises stress distribution in a bone system composed of an osteonal bone of $20$ GPa on the left, a CL of $16$ GPa in the middle, and an IB of $28$ GPa on the right for 2D simulations. The Von Mises stress is measured in MPa.
9 indenter positions are illustrated.

## 3.4 Tilted cement line

### 3.4.1 Exploring elastic properties of inhomogeneous materials via Young's modulus

The study focused on the effect of interface inclination on mechanical properties by analyzing 5 different angles: $-45°$, $-30°$, $0°$, $30°$, and $45°$, as illustrated in Figure 56. In this diagram, to facilitate understanding, a color has been assigned to each inclination, which also corresponds to the color of the curves in the following graph. This study also introduced inhomogeneity in the material properties of the bone structure. The only configuration studied is "Ref | Ref-20% | Ref+40%" for the osteonal bone, the CL, and the IB, respectively because it is the closest to

the experimental results. Figure 57 presents $E_r$ obtained as a function of the indenter's position for these $5$ different interface inclinations, with positions ranging from $-3R_{c_1}$ to $3R_{c_2}$.
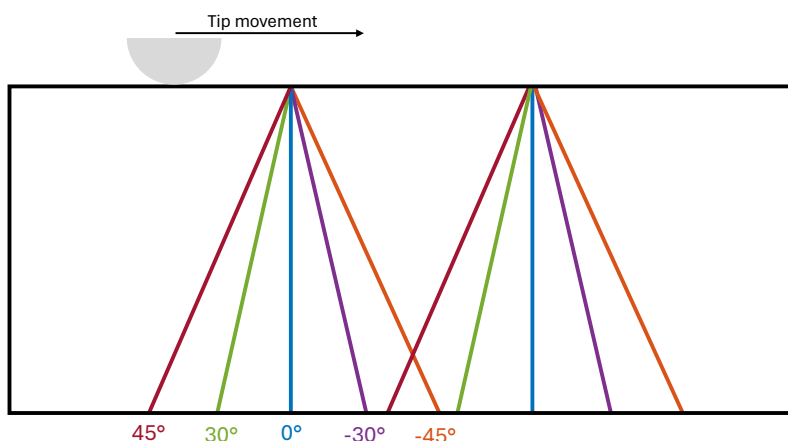


Figure 56: Schematic representation of $5$ inclinations of the interfaces.

In Figure 57, the blue dotted lines represent the Young's modulus values obtained for a 2D simulation of a homogeneous material. These lines, from bottom to top, correspond to an assignment of a Young's modulus of $20, 24$, and $28$ GPa respectively for the homogeneous material. The points marked in yellow correspond to the indenter's position equivalent to the contact radius, located on both sides of the interfaces.

It is notable that negative and positive inclinations exhibit asymmetric behavior in the Young's modulus values. Indeed, the inclinations of -45° and -30° tend towards the reference value on the left, corresponding to the expected Young's modulus for a homogeneous material. On the other hand, the inclinations of 30° and 45° approach the reference value of the IB on the right.

When the indenter is placed in the middle of the CL, it can be observed that only the blue curve gives an $E_r$ corresponding to the expected reference value. The burgundy and green curves are above this reference line, overestimating the expected value. Conversely, the purple and orange curves are below this reference line, underestimating the expected value.

In the CL region, the Young's modulus increases for all curves. However, when the interfaces are inclined, the Young's modulus value varies significantly throughout the entire region. In contrast, when there is no inclination of the interfaces, a stabilization of the Young's modulus is observed between $2R_{c_1}$ and $-2R_{c_2}$. In this situation, the increase in $E_r$ is less pronounced compared to the other curves.

An additional observation concerns the transition between the different zones: from the osteonal bone to the CL, and from the CL to the IB. In the configuration without inclination, a significant increase in the Young's modulus is observed when the indenter crosses the interface, particularly from $-1R_{c_1}$ to $1R_{c_1}$, as well as between $-1R_{c_2}$ and $1R_{c_2}$. During the passage of the indenter from $-1R_{c_1}$ to $1R_{c_1}$, the -45° inclination shows the smallest increase in the Young's modulus among the four inclinations studied. Additionally, for the passage from $-1R_{c_2}$ to $1R_{c_2}$, the 45° inclination shows the smallest increase.

The difference in behavior between the 30° and 45° inclinations gradually decreases as the indenter moves towards the IB. Conversely, an opposite trend is observed between the -30°

and -45° inclinations; the difference between these 2 curves increases as the indenter moves towards the IB. The reverse behavior is observed when the indenter moves towards the osteonal bone.

In conclusion, this study shows that the Young's modulus varies not only according to the position of the indenter but is also sensitive to the inclination of the interfaces.
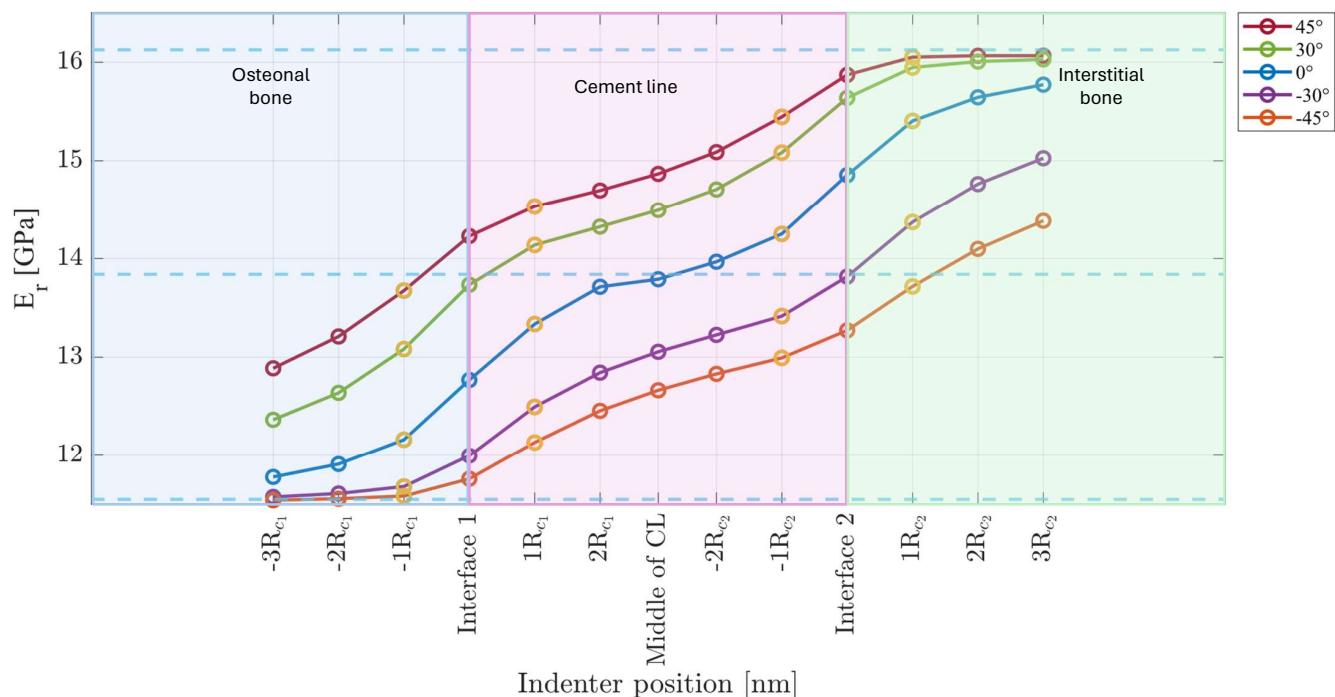


Figure 57: Variation of the $E_r$ measured in GPa as a function of the indenter position measured in $nm$ for a bone system with a different configuration of assigned elastic modulus for 2D simulations. The 5 curves represent 5 different inclinations of the interfaces. The indenter positions range from -$3R_{c_1}$ to $3R_{c_2}$ with respect to the interfaces: osteonal bone (on the left) - CL (in the middle) and CL and IB (on the right). The yellow circles indicate the position of the contact radius during an indentation of $150\ nm$, equivalent to $173\ nm$. The blue dashed lines correspond to the Young's modulus obtained for an interaction between a homogeneous material and a diamond during 2D simulations. From bottom to top, these lines represent a homogeneous material of $16, 20,$ and $28$ GPa.

Tables 12 and 13 show measurements of vertical distances, calculated from the position of the indenter when it is indented by $150\ nm$ until it meets an inclined interface at different angles (-45°, -30°, 30°, 45°). These measurements help to understand how the distance between the indenter and the interface varies based on the inclination and its position, which aids in interpreting the mechanical behavior of the bone structure. These distances were calculated using principles of trigonometry. The details of the calculations are illustrated in Appendix B, Figure 62.

| Indenter position | | Distance from the position of the indenter at 150 nm depth to the interface 1 [nm] | | | Distance from the position of the indenter at 150 nm depth to the interface 2 [nm] | | | | | |
|---|---|---|---|---|---|---|---|---|---|---|
| | | $-3R_{c_1}$ | $-2R_{c_1}$ | $-1R_{c_1}$ | Interface 1 | $1R_{c_1}$ | $2R_{c_1}$ | Middle of the cement line | $-2R_{c_2}$ | $-1R_{c_2}$ |
| Inclinaison [°] | 30 | 749 | 449 | 149 | 1582 | 1282 | 982 | 716 | 449 | 149 |
| | 45 | 369 | 196 | 23 | 850 | 677 | 504 | 350 | 196 | 173 |

Table 12: Vertical distance calculated between the position of the indenter when it is depressed by $150\ nm$ and the first interface encountered for interface inclinations of 30° and 45°.

| Indenter position | | Distance from the position of the indenter at 150 nm depth to the interface 1 [nm] | | | | | | Distance from the position of the indenter at 150 nm depth to the interface 2 [nm] | | |
|---|---|---|---|---|---|---|---|---|---|---|
| | | $1R_{c_1}$ | $2R_{c_1}$ | Middle of the cement line | $-2R_{c_2}$ | $-1R_{c_2}$ | Interface 2 | $1R_{c_2}$ | $2R_{c_2}$ | $3R_{c_2}$ |
| Inclinaison [°] | -30 | 149 | 449 | 716 | 982 | 1282 | 1582 | 149 | 449 | 749 |
| | -45 | 23 | 196 | 350 | 504 | 677 | 850 | 23 | 196 | 369 |

Table 13: Vertical distance calculated between the position of the indenter when it is depressed by $150\ nm$ and the first interface encountered for interface inclinations of -30° and -45°.

Figure 58(a) shows, for each inclination, the percentage differences between $E_r$ obtained at each indenter position and the expected reference value for a homogeneous material, designated "Ref", in the osteonal bone area. Figure 58(b) also shows the percentage difference, but here the reference used is "Ref+$20\%$", corresponding to the CL. Finally, Figure 58(c) compares the percentage difference relative to a value of "Ref+$40\%$", which is that of the IB.

In Figure 58(a), the general trend shows an increase in the percentage difference as the indenter moves towards the interface between the osteonal bone and the CL. However, this increase is relatively small for interface inclinations of -30° and -45°, where the percentage difference increases from $0\%$ to $3.8\%$ for the -30° inclination and to $1.8\%$ for the -45° inclination, starting at the position $-3R_{c_1}$. In contrast, the curves for the 30° and 45° inclinations show more pronounced increases from the beginning, at the position $-3R_{c_1}$, with values of $7\%$ and $11.6\%$ respectively. These values increase further to reach $18.9\%$ and $23.2\%$ at "interface 1". The blue curve, representing the configuration without inclination, lies between these extremes, starting with a percentage difference of $2\%$ and rising to $10.5\%$ at "interface 1".

Figure 58(b) focuses on the CL region. Negative percentage values indicate that $E_r$ is underestimated compared to the expected Young's modulus. The orange and purple curves, corresponding to inclinations of -45° and -30° respectively, underestimate the Young's modulus throughout the region, with percentage differences starting at -15% and -13% at the position of "interface 1" and decreasing to -4% and -0.1% at "interface 2". The blue curve, corresponding to the configuration without inclination, underestimates the Young's modulus up to the middle of the CL, where the percentage error is $0\%$. Beyond this position, it overestimates the expected value, reaching up to $7.2\%$ at "interface 2". The green and burgundy curves overestimate $E_r$ at every indenter position in the CL region. Table 14 shows the percentage differences for all

configurations when the indenter is placed in the middle of the CL, illustrating that the orange and purple curves underestimate $E_r$ while the green and burgundy curves overestimate it.

Figure 58(c) evaluates the percentage differences in the IB region. All curves underestimate the expected Young's modulus value. The greatest underestimation occurs at "interface 2" for the -45° inclination, where the percentage difference is -17.7%. For the inclinations of 30° and 45°, the errors tend towards 0% as the indenter moves to the right.

Another way to calculate the percentage difference was performed by calculating the percentage error relative to the configuration without inclination considered as the reference (see Appendix B, Figure 63).

In Figures 59(a),59(b), and59(c), normalized boxplots are presented via the difference between the measured Young's modulus at each position and the expected value (the value measured in the homogeneous material) for the osteonal bone, the CL, and the IB respectively. Each boxplot is associated with a specific inclination.

The presented results show significant variability in mechanical properties depending on the inclination, as well as the considered bone region. For the osteonal bone, the 45° inclination exhibits the highest standard deviation, at $0.59$ GPa, while the -45° inclination shows the lowest standard deviation, at $0.1$ GPa. This behavior is reversed in the IB, where the 45° inclination provides the lowest standard deviation, at $0.09$ GPa, and the -45° inclination the highest, at $0.48$ GPa. In the osteonal bone, as the inclination approaches positive values, the measurements deviate further from $0$, indicating a progressive overestimation of the expected Young's modulus. This is manifested by an increase in values on the ordinate axis. Conversely, in the IB, a negative inclination leads to values increasingly deviating from the expected value, resulting in an underestimation of the expected Young's modulus, with a decrease in values on the ordinate axis.

The one-way ANOVA analysis allows for examining the significant differences in terms of the means of these various groups ($p < 0.01$). In the osteonal bone, the inclinations of -45° and -30° are both significantly different from the positive inclinations, namely 30° and 45°. The means of the configuration with no inclination and an inclination of 45° are significantly different.

In the CL, the 0° inclination provides the values closest to $0$, indicating that this inclination offers the best estimation of the expected Young's modulus. The -45° inclination is significantly different from the inclinations of 0°, 30°, and 45° in the CL area. Also in this area of interest, the -30° inclination has a mean that is significantly different from the inclinations of 30° and 45°. Finally, the configuration with no inclination (0°) is significantly different from the extreme inclinations, namely -45° and 45° in the CL.

In the IB, the inclinations of -45° and -30° are significantly different from all other inclinations. Unlike what was observed in the osteonal bone, the configuration with no inclination has a mean that is significantly different from the inclinations of -45° and -30°.

Additional information regarding the mean and standard deviation for each inclination in each zone is provided in Appendix C, in Tables 18, 19 and 20.
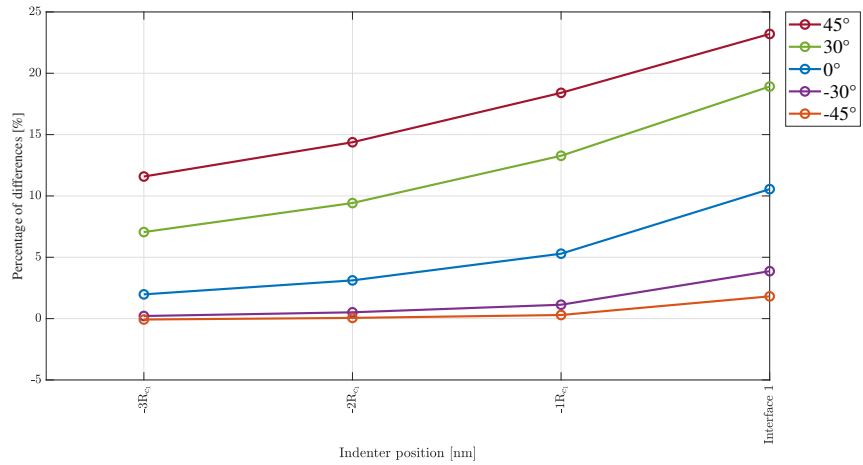
(a). Osteonal bone.
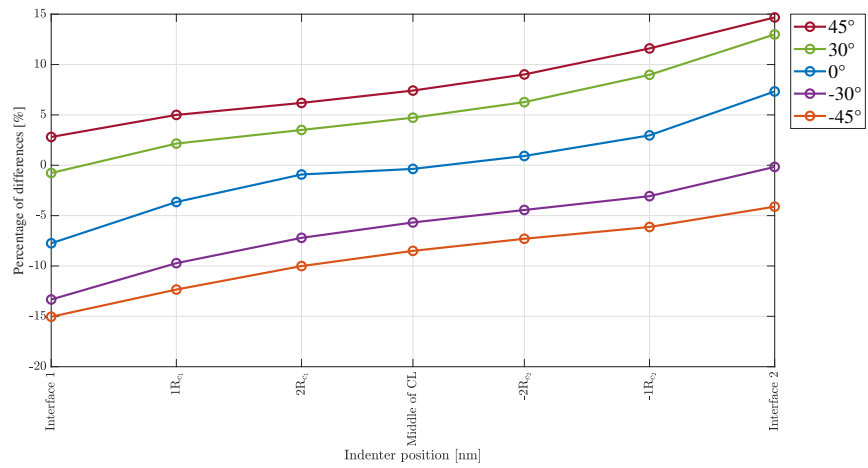


(b). Cement line.
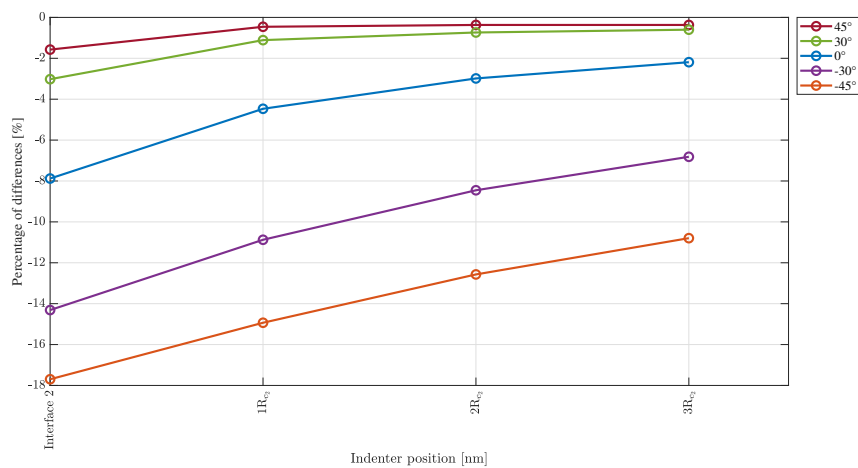


(c). Interstitial bone.

Figure 58: Comparison of the variation of the percentage differences in % as a function of the position of the indenter measured in $nm$ for a bone system for a single configuration of assignment of the elastic modulus for 2D simulations and five interface inclinations: -45°, -30°, 0°, 30°, and 45°.

| Inclinaison [°] | Percentage of differences [%] |
|:---:|:---:|
| **-45°** | -8.5 |
| **-30°** | -5.6 |
| **0°** | 0 |
| **30°** | 4.7 |
| **45°** | 7.4 |

Table 14: Comparison of the percentage differences in % as a function of the inclination of the interfaces (-45°, -30°, 0°, 30°, and 45°) when the indenter is positioned in the middle of the CL.



(a). Osteonal bone.

(b). Cement line.

(c). Interstitial bone.
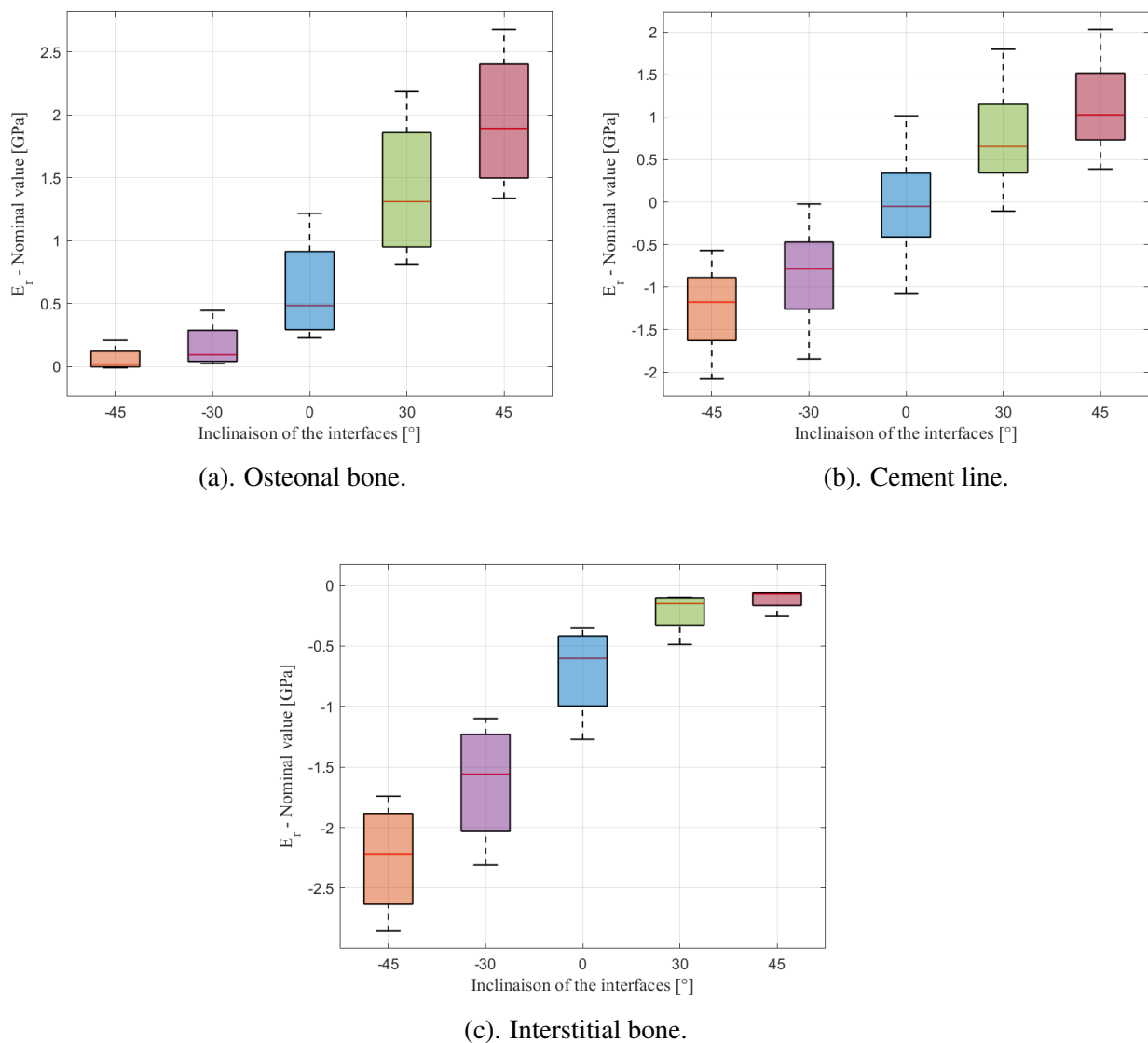
Figure 59: Boxplots representing the variability of the normalized Young's modulus for different inclinaisons of the interfaces in the different regions.

### 3.4.2 Qualitative analysis of Von Mises stress

Figure 60 shows images of the Von Mises stress distribution at 3 different indenter positions: at the interface between the osteonal bone and the CL, in the middle of the CL, and at the interface between the CL and the IB, for the 5 inclinations (-45°, -30°, 0°, 30°, 45°). The stress scale ranges from 0 to 6050 MPa.

A discontinuity in the stress distribution is observed at the interfaces for each configuration. The stress concentration near the indenter contact shows high values that increase as the indenter moves to the right, as well as the distance over which the stress propagates.

For the inclinations of -45° and -30°, when the indenter is placed in the middle of the CL, the stress propagation does not reach "interface 2". In contrast, for the configuration without inclination, the stress propagates both in the osteonal bone and in the IB when the indenter is placed in the middle of the CL.

For the inclinations of 30° and 45°, when the indenter is placed in the middle, the stress propagates only in the CL and in the IB.

The configuration with the interfaces inclined at 45°, with the indenter placed at the interface between the CL and the IB, shows the highest stress concentration, marked by a red color indicating a stress of approximately 6050 MPa. In contrast, the configuration with the interfaces inclined at -45°, with the indenter placed at the interface between the osteonal bone and the CL, shows a lower stress concentration near the contact, illustrated by a yellow-green color, indicating a stress value of approximately 4000 MPa.
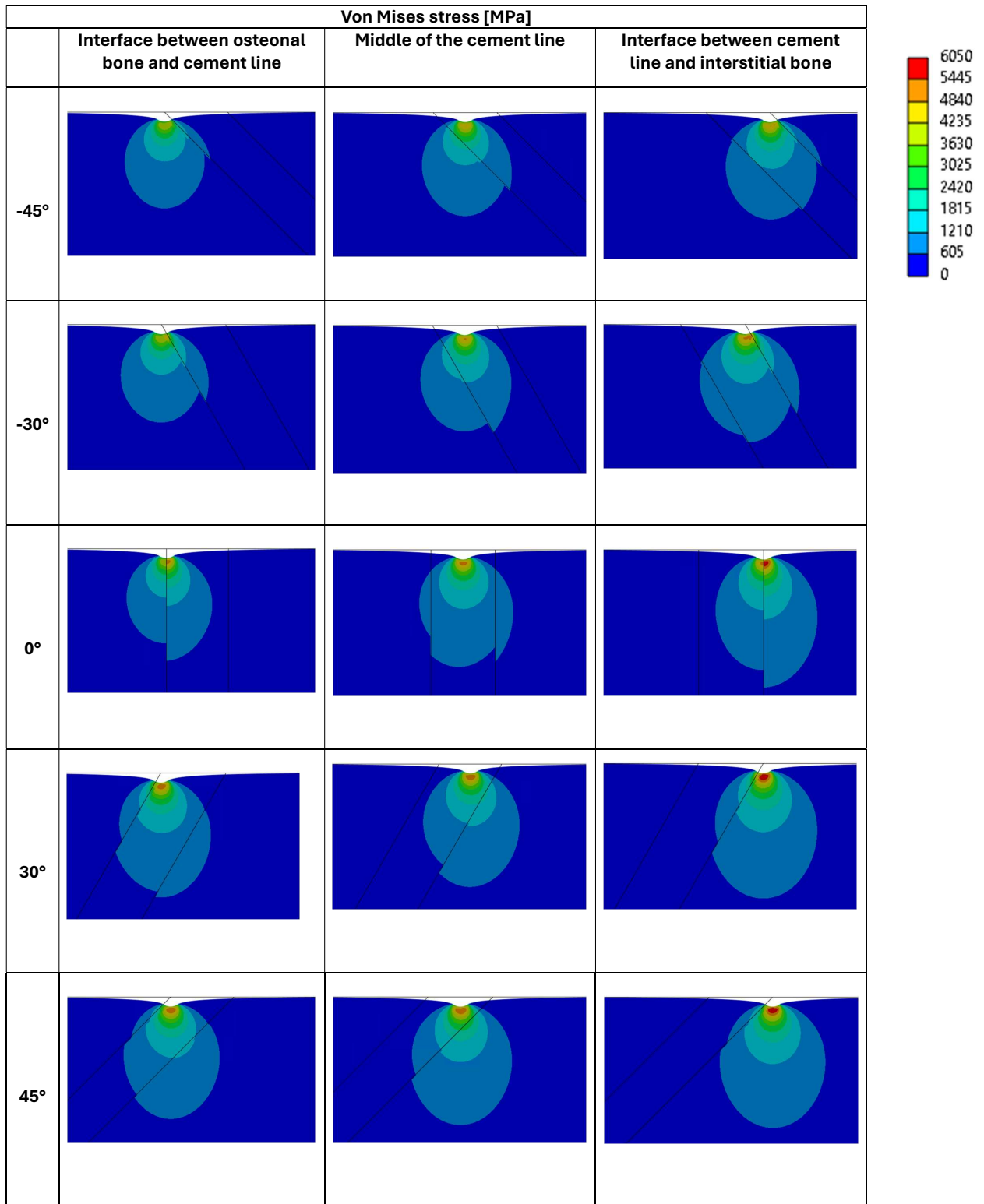
Figure 60: Comparison of the distribution of Von Mises stress in a bone system composed of an osteonal bone of $20$ GPa on the left, a CL of $24$ GPa in the middle, and an IB of $28$ GPa on the right for 2D simulations, with $5$ inclinations of the interfaces: -45°, -30°, 0°, 30°, and 45°. Von Mises stress is measured in MPa.
3 positions of the indenter are illustrated for each inclination.

# Chapter 4

# Discussion

This chapter aims to discuss the results obtained in the previous section in order to interpret the mechanical behavior of an inhomogeneous bone structure and explore the limitations of FEM simulations. It will also address strategies to improve the reliability of experimental results and suggest possibilities for future research.

## 4.1 Understimation in 2D simulations

The non-convergence of 3D simulations at a penetration depth of $150\ nm$ has limited the study of the full model. However, a smaller indentation, down to $5\ nm$ in 3D, is feasible as it generates less stress. Thus, a comparison between 2D plane strain and 3D simulations at this $5\ nm$ depth has been analyzed, revealing significant differences as well as similarities.

It has been demonstrated that $E_r$ is directly influenced by the characteristics of the CL. An increase in this modulus is observed when the CL has a higher elastic modulus, directly influencing the measured mechanical properties. The results have revealed that the presence of the CL is noticeable even when the indenter is placed $100\ nm$ approximately from the interface, corresponding to about $3$ times the contact radius. The observed trend between 2D and 3D simulations remains similar depending on the configurations used and their influence on the measurement of $E_r$ (see Figure 44).

The discrepancies observed in the values of the Young's modulus between 2D plane strain and 3D simulations can be explained by how the model deforms. This difference is analyzed based on the principle of volume conservation and the Poisson effect. Indeed, a material subjected to deformation tends to maintain its volume. Therefore, the compressive stress induced by the indentation in the $y$-direction causes the material to expand in the $x$ and $z$ directions to keep its volume constant. This phenomenon, where the material tends to expand or contract in directions perpendicular to the applied load, is described by the Poisson's ratio [100]. In 3D simulations, the model can undergo triaxial compression, meaning that the material can be compressed in all 3 axes. This 3D approach provides a faithful representation of the deformations and stresses generated in the material during indentations, as it is free to deform in all 3 directions. Therefore, the observed mechanical response is more comprehensive. This complexity in the interactions between the indenter and the material in 3 directions directly influences the measured stiffness, resulting in more accurate results [100]. In the case of a 2D plane strain model, deformation is considered null in the third direction, perpendicular to the plane. Only 2D are free to deform since the 2D plane strain modeling ignores the third dimension. The compressive stress in this third direction is generated solely by the need to maintain the material's volume. Indeed, compression within the plane implies that in the out-of-plane direction, the model must contract or expand based on the key principle of volume conservation. This additional constraint in the third direction, termed artificial, limits the actual deformation of the material, leading to an underestimation of $E_r$. Indeed, the out-of-plane stresses, which are due to volume conservation, reduce the overall effect of the stresses compared to the triaxial stress condition in 3D. This simplification results in a material appearing less rigid, as the complex stresses related to the third direction, which would increase stiffness, are not

fully captured. The stresses along the $x$-axis and $y$-axis adjust due to the non-deformation in the $z$-axis, but this adjustment does not allow for the real effect of the complex interaction of triaxial stresses as in 3D. Previous studies using the FEM have also shown that 2D plane strain models tend to underestimate mechanical properties compared to 3D models. The results of these studies have revealed that the hardness and stiffness measured in 2D simulations with a cylindrical indenter are lower than those obtained in 3D simulations with a spherical indenter [100][101][102] [103].

The Hertzian theoretical model, originally designed to analyze contact between 2 cylinders with parallel axes, is applicable for 3D simulations. The discrepancy observed between the reaction force obtained in 2D simulations and the prediction of the Hertz model can be explained by the inability of 2D modeling to accurately capture triaxial stresses.

The analysis of the underestimation of elastic moduli assigned to homogeneous materials is detailed in Section 3.3.1. The Young's moduli considered for the 2D simulations of homogeneous materials are $16, 20, 22, 24$, and $28$ GPa. The results obtained for all 2D simulations for these various configurations showed an approximate difference of $42\%$ between $E_r$ obtained and the Young's modulus initially attributed to the material.

## 4.2 Placement of the tip accross 3 different materials

The study focused on analyzing the variability of material properties. Material inhomogeneity was introduced to address experimentally observed limitations. The primary interest of this analysis stems from the experiments conducted by Astrid Cantamessa, during which the nanoindenter was used to make indentations at one-micrometer intervals. Given the very small size of the CL, which measures at least $1 \ \mu m$, positioning the indenter represents a major challenge. Despite the nanoscopic resolution of the technique used, the surface probed by the indenter often exceeds the size of the CL itself. Consequently, the measurements obtained are directly influenced by the adjacent bone tissues, such as osteonal bone or IB. This proximity can alter the measurements made in the CL. Through simulations based on the FEM, it is possible to better understand this influence. They also allow for a deeper exploration of how the variability of the measurements evolves depending on the position of the indenter for different configurations of the adjacent bones. In Section 3.3, the study of the variability of the measured Young's modulus is analyzed for 2 configurations: when the CL is surrounded only by osteonal bone, and when the CL is surrounded by both osteonal bone and IB.

In the configuration where osteons surround the CL, the results showed symmetry in the Young's modulus depicted on the curves, whether the CL is $20\%$ stiffer or $20\%$ softer than the osteonal bone (see Figure 47, 48, and 49). However, this symmetry can be misleading, as the configuration with a softer CL affects the obtained Young's modulus slightly more than the stiffer one, even at a distance of $-3R_{c_1}$ from the CL. It is important to note that both configurations also affect the Young's modulus at this distance; the effect is just more pronounced for the softer CL. This indicates that the material properties of the CL directly impact the mechanical behavior of the immediately adjacent bone region. Moreover, given the extremely fine size of the cementing line, it is actually the surrounding bones that influence the mechanical behavior of the CL, considering that the area affected by the indenter is larger than the size of the CL. Visually, the symmetry between the 2 configurations might suggest a proportional relationship between the stiffness of the CL and $E_r$ measured. However, the influence of the softest CL on mechanical properties suggests a nonlinear response of the bone structure. This indicates that

the bone structure remains more sensitive to a softer CL at a distance of $-3R_{c_1}$, compared to the effect of a stiffer CL at the same distance. It is therefore important to analyze the different configurations separately to avoid deducing the mechanical behavior of the bone structure based on a single configuration.

The study also conducted an analysis of the errors made in measuring Young's modulus in a heterogeneous material, highlighting that these errors, compared to the expected value, are primarily due to the positioning of the indenter. These percentages of differences are significant as they reveal the experimental limits during indentation tests in bone structures. It has been demonstrated that this limitation can lead to significant difference from the expected value depending on the configurations, which shows the need to be cautious about the reliability of experimental results. In particular, even when the indenter is located in the middle of the CL, about 3 times the contact radius from the interfaces, the deviation in measuring the Young's modulus can reach up to $10\%$ (see Figure 51(b)). This deviation is not negligible. FE simulations show that, to minimize error, it is preferable to position the indenter away from interfaces when indenting in the CL. Indeed, deviations can reach $17\%$ near the interfaces, while in the middle of the CL, the results have shown that a deviation of up to $9\%$ could be achieved, which is considerable, but still lower. These observations have underscored the importance of precise indenter placement and the assessment of the influence of adjacent materials.

It has been observed that the greater the difference in stiffness between the CL and the surrounding materials, the more significant the impact on the measurement of the Young's modulus, both within the CL and in the surrounding materials. This influence caused by the softer CL on the mechanical behavior results in a larger error. However, during experimental experiments, the transition between materials is generally more gradual, as shown by the measurements obtained by Astrid Cantamessa, with a modulus of 20 GPa for the osteonal bone, 24 GPa for the CL, and 28 GPa for the IB [104]. Simulations have shown that this configuration of elasticity moduli allows for more reliable measurements at certain positions. To measure the Young's modulus of the CL reliably, it is preferable to place the indenter in the middle of it, as at this position, the error made is close to $0\%$. For the osteonal bone and the IB, it is recommended placing the indenter more than 3 times the contact radius from the interface. The greater the difference in stiffness during the transition of interfaces, the greater the the deviation of the Young's modulus is in the middle of the CL. It is therefore important to consider the position of the indenter within a heterogeneous material. In conclusion, during nanoindentation measurements, it is suggested not to limit to indentations within the CL only, but also to indent in the osteonal bone and IB to better understand whether the measurements are underestimated or overestimated depending on the configuration of material properties.

## 4.3 Discontinuities in Von Mises stress

The distribution of Von Mises stress illustrates the influence of Young's moduli assigned to materials on the stress concentration under the indenter (see Figure 45). Indeed, when the indenter is placed in the CL, which has a Young's modulus $20\%$ higher than that of the surrounding osteonal bone, a higher stress concentration was observed, indicating that an increase in stiffness intensifies stress locally. Furthermore, in the configuration where IB is introduced, the stress propagates more extensively into the IB compared to the less rigid CL, thus showing that an increase in stiffness favors a deeper stress distribution in the bone structure. At an equivalent depth, an increase in the material's stiffness extends the distance of stress propagation. Finally, in a configuration where the CL has a Young's modulus reduced by $20\%$ and the IB is increased

by $40\%$ compared to the osteonal bone, a more marked discontinuity in stress distribution is observed, indicating a potential risk of failure due to this significant discontinuity.

In the stress distribution, a more rigid material leads to a higher stress concentration while also causing a reduction in the stress over a greater distance. Moreover, a significant transition in the stiffness difference between 2 materials accentuates the observed discontinuity, which directly impacts the distance over which the stress diminishes. Thus, in a less rigid region, the stress may be null at a certain depth, whereas in a more rigid region, high stresses still persist at the same depth (see Figure 53, 54 and 55).

## 4.4   Tilted cement line

The study then focused on the impact of the inclination of interfaces, a common morphological variability in experimental tests due to the sample sectioning process, which is often not perfectly straight. Various inclinations were studied, up to an extreme inclination.

The results showed that the inclination of the interfaces significantly influences the measured $E_r$. In configurations with a negative inclination, even when the indenter is placed far from the interface, the stiffness of the CL affects the measured modulus. When the indenter is at $1R_{c_2}$ from the interface, the distance separating the indenter when it penetrates $150\ nm$ from the CL interface is $23\ nm$ and $149\ nm$ (see Table 13) for inclinations of -45° and -30° respectively, bringing the measured $E_r$ closer to that of the CL rather than that of the IB. This sensitivity related to the vertical distance from the interface explains why errors can increase in some cases. For example, an inclination of 45° can lead to an error of $12\%$ at a distance $-3R_{c_1}$ from the interface (see Figure 58(a)), and $7.5\%$ in the middle of the CL (see Table 14). The inclinaison of -45° showed the highest deviation at the middle of the CL with -8.5%, highlighting the importance of the sample-sectioning process. The inclination of these interfaces can slighlty alter the reliability of the results. However, it must be kept in mind that this deviation is not very considerable compared, for example, to that of the -45° inclination, which is not very realistic. Ultimately, it has been demonstrated that inclination influences the results, but not as much as the positioning of the indenter. If the positioning is in the middle of the CL, the risk of obtaining a significant deviation is lower, even in extreme cases (-45° and 45°). However, in the context of this work, only one configuration ("Ref | Ref+20% | Ref+40%") was used for the different inclinations. Therefore, it would be more prudent to extend this study to other configurations that could potentially lead to more significant deviations.

In practice, as it is rare to obtain a perfect sample cut, this study has helped quantify the reliability of the results. As previously explained, the experimental measurements allowed for an indentation every $1\ \mu m$. In the extreme case where the CL measures $1\ \mu m$, it is important to position the indenter in the middle of the CL. Indeed, in the configuration where the interfaces are straight (0°), the measurement of $E_r$ in the middle of the CL is consistent with the expected value. However, as soon as the interfaces are inclined, the measurements deviate from the expected value. To correct the measurements, one option is to use the Focused Ion Beam (FIB) technique coupled with high-resolution Scanning Electron Microscopy (SEM). Initially, data are collected using nanoindentation, which can then be followed by FIB-SEM observation. This allows for obtaining high-quality, in-depth images of the material, but it destroys the analyzed surface. Thus, the technique is capable of recording a series of in-depth images that allow observing the brightness of the CL at different depths to determine the inclination. Another approach would be to use synchrotron tomography (SR-Micro CT), which would also

allow for analyzing the inclinations of the interfaces. Consequently, these imaging techniques can be avenues for analyzing and correcting deviations caused by inclinations in combination with simulations. Furthermore, it is also recommended to combine experimental nanoindentation with BEI to precisely assess the position of the penetrator within the bone structure. Indeed, the nanoindentation machine does not allow for accurate determination of the indenter's position relative to the CL, which leads to somewhat blind indentation. BEI imaging can then be performed after nanoindentation tests to determine the exact position of the imprint, whether it is centered or slightly deviated from the CL, in order to draw conclusions about the local mechanical properties of the material.

In the literature, bone has a compressive failure stress of 150 MPa (see Figure 8). However, the Von Mises stress values obtained can reach up to 6000 MPa. This results from the assumption of linear elasticity of the material. Indeed, at a depth of 150 $nm$, the bone develops complete plasticity.

## 4.5   Limitations

The study presents several limitations that pave the way for further research.

Firstly, a limitation of this study lies in the idealization of the values used, which do not reflect the variability in the mechanical properties of materials. Indeed, materials are not perfectly homogeneous. For example, it is rare that 2 osteons located on either side of the CL possess the same Young's modulus. Additionally, there is also significant variability within a single osteon or the IB in the Young's modulus.

Secondly, the assumption of a linear elastic behavior, where loading and unloading curves overlap, is a significant hypothesis. In reality, at a penetration depth of 150 $nm$, bone already enters plastic deformations. Thus, by assuming this linear elastic behavior, this simplification rules out the non-linear behaviour that can be observed at this depth.

Thirdly, although the study focused on isotropic materials, similar to work done by other authors, bone exhibits transverse isotropy. Therefore, it is appropriate to consider this characteristic for a better representation of the real behavior of the bone structure. It is important to note that several studies adopt this hypothesis of isotropic linear elasticity [105] [106] [107]. But this assumption can lead to an underestimation or overestimation of the mechanical properties of the bone.

Furthermore, an assumption regarding the homogeneity of each material was established. However, due to its complex microstructure, bone tissue is highly heterogenous.

Moreover, bone tissue has a viscoelastic response, which affects the results obtained. Indeed, the viscoelastic response of bone tissue implies that its mechanical properties are time-dependent. The mechanical response of the bone thus depends on the duration during which the nanoindentation test is performed. The simulations were conducted in a quasi-static manner, assuming that the imposed deformation rates are considered slow enough to neglect dynamic effects. This assumption leads to the analysis of only elastic properties, without considering dynamic responses related to the speed of the indenter's application. Consequently, this omits the real behavior of the material when it is subjected to cyclic or rapid loads [108] [109] [110].

In the model studied, frictionless contact was assumed. However, in reality, the presence of friction is logical. In the literature, the majority of studies have considered a frictionless contact.

Adam and Swain [111] studied the effect of friction during nanoindentation on bone tissue by considering a 2D axisymmetric model. Considering this friction can change the results as they observed that an increase in the coefficient from $0$ to $0.3$ can lead to a reduction in the maximum displacement of the indenter by $10\%$ to $20\%$. Therefore, the assumption of a frictionless contact can lead to an underestimation of the actual mechanical behavior.

It is also important to highlight the limitation associated with the use of 2D plane strain modeling in this study. While this approach facilitated the acquisition of results and the interpretation of the mechanical properties of bone interfaces, it does not allow for the capture of the complete behavior of materials. Indeed, this leads to underestimations compared to 3D modeling, which takes into account triaxial compression, as previously explained.

In the context of this work, a cylindrical indenter in 2D and a spherical indenter in 3D were used for the simulations due to their simplicity in geometric modeling. In reality, experimentally, a Berkovich type indenter, a $3$-sided pyramid, was used. However, Shelef and Bar-On [79] demonstrated in their research that using a spherical indenter ($R_{\text{tip}} = 100\ nm$) and a conical indenter ($\theta = 68°$) leads to similar results in terms of mechanical properties. But, it is worth noting that other geometries could also have been considered for use in the study. Therefore, exploring other indenter shapes could potentially yield similar results, which would enrich the methodology employed in the study.

## 4.6 Perspectives

In the context of this study, each material was considered non-porous and homogeneous. However, the analysis could be enriched by exploring heterogeneity in different ways, such as the influence of porosity, which clearly affects the measurements, or by modeling collagen fibers in various orientations within the osteonal bone [57]. Although the analysis was primarily focused on the CL in cortical bone, it should be noted that the cement itself is less porous than the osteon and the IB. Indeed, the osteocyte-lacuno-canalicular network is much less dense or even completely disrupted at the CL. Therefore, it would be interesting to study this porosity as it influences experimental measurements by causing a high contrast due to these pores which reduce the Young's modulus, while the CL and the osteon are close. Moreover, the effect of porosity, including osteocytes and canals, can be studied to understand how the Young's modulus behaves nearby and from what point the influence of these structures is felt [112] [113].

As previously highlighted, the overall mechanical response of bone structures cannot be predicted based on equivalent behavior relations. It is important to treat each configuration separately. The stiffness values chosen were relatively similar to the experiments, but these were somewhat idealized. For example, it is unlikely that $2$ osteons surrounding the cement would have the same Young's modulus, as some osteons may be more mineralized leading to higher stiffness. Within the time allocated by the thesis, it was not possible to test more configurations involving lower stiffness contrasts. Future research could explore a wider range of stiffness for various materials.

Further investigation could involve studying the transition of stiffness between materials. Indeed, the study featured a sudden shift from rigid to soft materials, with each material having a distinct Young's modulus. The stress distribution showed a discontinuity that could be much more pronounced in certain cases. A more gradual transition of stiffness could provide a finer analysis in characterizing these mechanical behaviors.

Moreover, it would be pertinent to analyze the effect of surface topography, given that polishing tends to remove more soft materials than stiff materials, resulting in a surface that is not perfectly flat, particularly at the interfaces which could have a significant impact on the measurements.

Initially, an analysis of the model length was conducted to assess the impact of the boundaries on the mechanical response. It was found that the maximum acceptable distance, to avoid a significant decrease in the measured Young's modulus, is $3.5\ \mu m$ for an indenter penetration of $150\ nm$. Consequently, the osteonal bone and IB were modeled with a length of $4\ \mu m$. However, the study of the tip position revealed that, in certain configurations, the CL influences the mechanical response of the surrounding materials even beyond $3$ times the contact radius, which is the accepted limit to avoid feeling the influence of the boundaries. For example, the convergence towards the Young's modulus of the osteonal bone is accelerated in the configuration where the CL is stiffer compared to configurations where the CL is softer. Therefore, for future studies, an enlarged model would be preferable to determine the distance from which the CL ceases to influence the mechanical response of the surrounding materials.

Resolving the non-convergence of 3D simulations would allow for a re-examination of material behavior and observation of effects in all directions. Ideally, the analyses should have focused on 3D, but within the context of a master's thesis, time constraints did not permit resolving these issues.

To enrich the study, the effect of the indenter's radius combined with different penetration depths can be analyzed. As part of their research, Paietta et al. [107] examined the role of penetration depth and indenter radius, exploring a wide range of radii from $5$ to $200\ nm$ and penetration depths from $100\ nm$ to $200\ nm$ to analyze the impact on the measured mechanical properties.

# Conclusion

The main objective of this study was to characterize the local mechanical properties of 3 bone regions of different mineral content and age, using nanoindentation performed with an indenter radius of $200 \ nm$ and an indentation depth of $150 \ nm$ along the bone interfaces. This analysis was conducted using the FEM, with particular attention to the CL, a thin interface measuring 1 to $5 \ \mu m$. The main motivation for this study stems from the experimental limitations observed, despite the nanoscopic resolution of the nanoindentation machine, whose probed surface often which may be larger than the size of the CL itself. Thus, this characterization using simulations not only evaluated the influence of these thin bone interfaces on the mechanical behavior, studied how the measurements deviated from the expected values with the position of the indenter, but also offered valuable suggestions for better interpretation of experimental results.

To achieve this objective, a series of pilot tests were initially carried out to design the most appropriate model for launching the study. Although the ideal choice is a 3D modeling to capture all the complexity, limitations due to non-convergence of calculations directed the decision towards a 2D model as the best compromise given the time constraints imposed by this thesis. This 2D approach allowed comparison of relative properties and not absolute values. All simulations were performed using the ANSYS Workbench software.

In the first part of the thesis, the study was deepened by using 3 materials with different material properties to understand their mutual influence depending on the position of the indenter. The material properties were assigned based on experimental results (Cantamessa A. ESB 2023), showing that the CL is stiffer than osteonal bone [104]. On this basis, different configurations were established. The results demonstrated a sensitivity of the Young's modulus measurement for a CL that was either stiffer or softer than adjacent materials even at a distance of 3 times the contact radius from the interface, with a slightly higher deviation for the softer CL. Moreover, this influence increased when approaching the interfaces with surrouding tissues. In the CL, near theses interfaces, deviations reaching $17\%$ in the most extreme yet realistic case were observed, and for indents in the middle, the deviation reached up to $9\%$, which remains significant despite being lower. The analysis concluded that in cortical bone, the position of the indenter within the CL is important for the reliability of experimental results.

In the second part of the study, a more detailed exploration focused on the impact of the inclinations of bone interfaces on local mechanical properties. Indeed, the experimental sectioning process can lead to inclinations of these interfaces, which can significantly affect the reliability of interpretations. In the extreme case, where the interfaces are inclined at -45°, the deviation measured in the middle of the CL reached $8.5\%$. The results confirmed that straight sections produce the most reliable results, with an error close to $0\%$ in the middle of the CL. These observations demonstrate the importance of precise indenter positioning in experiments, which can be analyzed using BEI techniques post-nanoindentation.

In conclusion, this work has highlighted the influence of bone interfaces on the measured exact mechanical properties. This study also opens up new research perspectives, including examining the influence of porosity, the direction of collagen fibers in osteonal bone, and the exploration of the effect of surface topography.

# Appendix A

# 3D simulations

## A.1 Comparison: Hertz and Oliver-Pharr
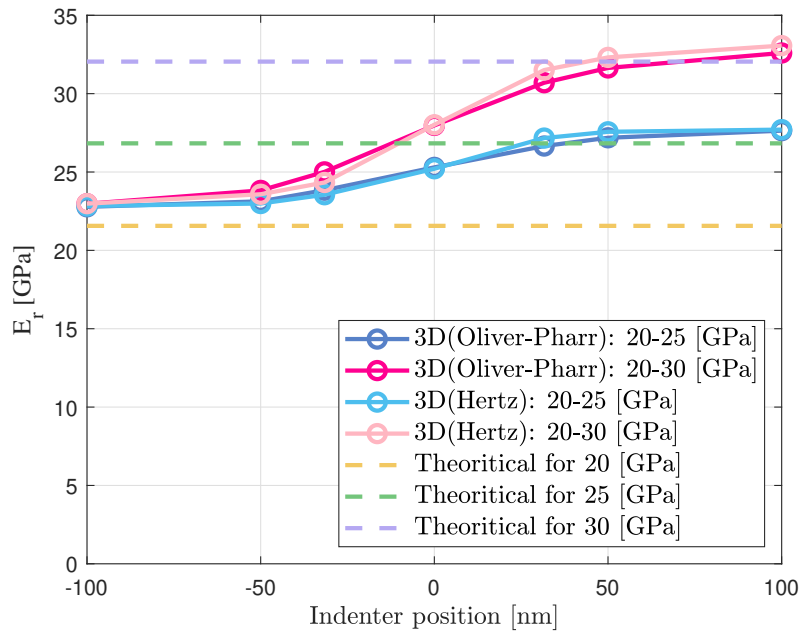


Figure 61: Comparison of the variation in $E_r$ measured in GPa as a function of indenter position measured in $nm$ for a bone system with an elastic modulus assignment of 20 GPa on the left and 25 or 30 GPa on the right for 3D simulations. In this graph, the Hertz model is compared with the Oliver and Pharr model to obtain Young's modulus. Indenter positions range from -100 $nm$ to 100 $nm$ relative to the interface between osteonal bone (left) and CL (right). The yellow, green and purple dotted lines correspond to the Young's modulus obtained for an interaction between a homogeneous material and a diamond. From bottom to top, these lines represent a homogeneous material of $20, 25$ and $30$ GPa.

# Appendix B

# Placement of the tip accros 3 different materials

## B.1 Mean and standard deviation

| Configuration | Ref \| Ref-20% \| Ref | Ref \| Ref+10% \| Ref | Ref \| Ref+20% \| Ref | Ref \| Ref-20% \| Ref+40% | Ref \| Ref+20% \| Ref+40% |
|---|---|---|---|---|---|
| Standard deviation | 0.3317 | 0.1765 | 0.3493 | 0.3062 | 0.4007 |
| Mean | 1.6909 | -0.8857 | -1.7596 | 1.7922 | -1.6301 |

Table 15: Mean and standard deviation of normalized Young's modulus measured in osteonal bone for $5$ material property configurations.

| Configuration | Ref \| Ref-20% \| Ref | Ref \| Ref+10% \| Ref | Ref \| Ref+20% \| Ref | Ref \| Ref-20% \| Ref+40% | Ref \| Ref+20% \| Ref+40% |
|---|---|---|---|---|---|
| Standard deviation | 0.3044 | 0.1505 | 0.2927 | 0.8933 | 0.6640 |
| Mean | 0.7692 | -0.4166 | -0.8366 | 1.3933 | -0.1190 |

Table 16: Mean and standard deviation of normalized Young's modulus measured in CL for $5$ material property configurations.

| Configuration | Ref \| Ref-20% \| Ref+40% | Ref \| Ref+20% \| Ref+40% |
|---|---|---|
| Standard deviation | 1.1004 | 0.4058 |
| Mean | -1.8717 | -0.7064 |

Table 17: Mean and standard deviation of normalized Young's modulus measured in IB for $5$ material property configurations.

# Appendix C

# Tilted cement line

## C.1 Trigonometry calculations
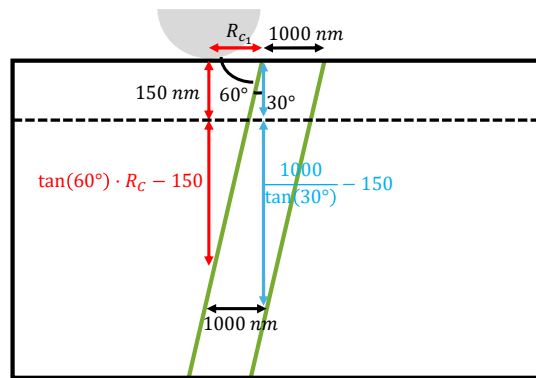


Figure 62: Schematic representation of the vertical distance calculated between the position of the indenter when it penetrated by $150\ nm$ and the first interface encountered for an interface inclination of $30°$.

## C.2 Percentage differences
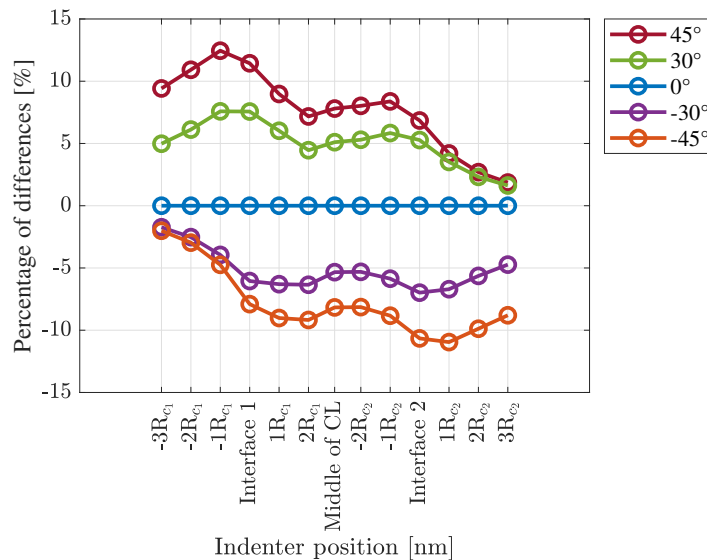


Figure 63: Comparison of the variation of the percentage differences in % compared to interfaces without inclines as a function of the position of the indenter measured in $nm$ for a bone system for a single configuration of assignment of the elastic modulus for 2D simulations.

## C.3 Mean and standard deviation

| Inclinaison [°] | -45 | -30 | 0 | 30 | 45 |
|---|---|---|---|---|---|
| Standard deviation | 0.1010 | 0.1926 | 0.4393 | 0.5981 | 0.5897 |
| Mean | 0.0605 | 0.1653 | 0.6046 | 1.4052 | 1.9508 |

Table 18: Mean and standard deviation of normalized Young's modulus measured in osteonal bone for 5 inclinations of the interfaces.

| Inclinaison [°] | -45 | -30 | 0 | 30 | 45 |
|---|---|---|---|---|---|
| Standard deviation | 0.5176 | 0.6027 | 0.6622 | 0.6287 | 0.5595 |
| Mean | -1.2540 | -0.8622 | -0.0288 | 0.7483 | 1.1211 |

Table 19: Mean and standard deviation of normalized Young's modulus measured in CL for 5 inclinations of the interfaces.

| Inclinaison [°] | -45 | -30 | 0 | 30 | 45 |
|---|---|---|---|---|---|
| Standard deviation | 0.4824 | 0.5253 | 0.4058 | 0.1812 | 0.0950 |
| Mean | -2.2575 | -1.6310 | -0.7064 | -0.2205 | -0.1116 |

Table 20: Mean and standard deviation of normalized Young's modulus measured in IB for 5 inclinations of the interfaces.

# References

[1] Meyers M. and Chen P. *Biological Materials Science: Biological Materials, Bioinspired Materials, and Biomaterials*. Cambridge University Press, 1 edition, 2014.

[2] Šromová V. et al. A brief review of bone cell function and importance. *Cells*, 12(21):2576, 2023.

[3] Rodriguez-Palomo A. et al. Bone hierarchical structure: Heterogeneity and uniformity. *Advanced Functional Materials*, 2023.

[4] Mirzaali M. J. et al. Mechanical properties of cortical bone and their relationships with age, gender, composition and microindentation properties in the elderly. *Bone*, 93:196–211, 2016.

[5] Davy D. Bartel D. and Keaveny. *Orthopaedic Biomechanics: Mechanics and Design in Musculoskeletal Systems*. Pearson, 1 edition, 2006.

[6] Ambrogini E. *Principles of Bone Biology*. Elsevier, 2020.

[7] Wagermaier W. et al. Fragility of bone material controlled by internal interfaces. *Calcified Tissue International*, 97(3):201–212, 2015.

[8] Milovanovic P. et al. Bone tissue aging affects mineralization of cement lines. *Bone*, 110:187–193, 2018.

[9] Gauthier R. et al. 3D analysis of the osteonal and interstitial tissue in human radii cortical bone. *Bone*, 127:526–536, 2019.

[10] Skedros J. G. et al. Cement lines of secondary osteons in human bone are not mineral-deficient: New data in a historical perspective. *The Anatomical Record Part A: Discoveries in Molecular, Cellular, and Evolutionary Biology*, 286A(1):781–803, 2005.

[11] Langer M. et al. X-ray phase nanotomography resolves the 3d human bone ultrastructure. *PLoS ONE*, 7(8):e35691, 2012.

[12] Nalla R. K. et al. Mechanistic aspects of fracture and r-curve behavior in human cortical bone. *Biomaterials*, 26(2):217–231, 2005.

[13] Mohsin S. et al. Osteonal crack barriers in ovine compact bone. *Journal of Anatomy*, 208(1):81–89, 2006.

[14] Koester K. J. et al. The true toughness of human cortical bone measured with realistically short cracks. *Nature Materials*, 7(8):672–677, 2008.

[15] García-Aznar J. M. et al. Multiscale modeling of bone tissue mechanobiology. *Bone*, 151:116032, 2021.

[16] Kenkre J. and Bassett J. The bone remodelling cycle. *Annals of Clinical Biochemistry: International Journal of Laboratory Medicine*, 55(3):308–327, 2018.

[17] Martin R. B. et al. *Skeletal Tissue Mechanics*. Springer New York edition, 2015.

[18] Les Laboratoires Servier. *SMART-Servier Medical ART. 2024* `https://smart.servier.com/` *Consulted on 26th February 2024*.

[19] Safadi F. et al. *Bone Pathology*. Humana Press, 1 edition, 2009.

[20] Burr D. B. Targeted and nontargeted remodeling. *Bone*, 30(1):2–4, 2002.

[21] Currey J. D. The many adaptations of bone. *Journal of Biomechanics*, 36(10):1487–1495, 2003.

[22] Ethier C. R. and Simmons A. S. *Introductory biomechanics: from cells to organisms*. Cambridge University Press, 3 edition, 2011.

[23] Kahla R. and Barkaoui A. *Bone Remodeling Process*. Elsevier edition, 2021.

[24] Clarke B. Normal bone anatomy and physiology. *Clinical Journal of the American Society of Nephrology*, 3(Supplement$_3$):S131–S139, 2008.

[25] An Y. and Robert A. D. *Mechanical Testing of Bone and the Bone–Implant Interface*. CRC Press, 2000.

[26] Miller S. C. Bone lining cells: Structure and function. *Scanning Microscopy*, 3(3):953–960, 1989.

[27] Hu L. et al. *Bone Cell Biomechanics, Mechanobiology and Bone Diseases*. Academic Press, 2023.

[28] Weiner S. and Wagner H. D. The material bone: Structure-mechanical function relations. *Annual Review of Materials Science*, 28(1):271–298, 1998.

[29] Novitskaya E. et al. Anisotropy in the compressive mechanical properties of bovine cortical bone and the mineral and protein constituents. *Acta Biomaterialia*, 7(8):3170–3177, 2011.

[30] Seeman E. et al. Bone quality — the material and structural basis of bone strength and fragility. *New England Journal of Medicine*, 354(21):2250–2261, 2006.

[31] Wawrzyniak A. and Balawender K. Structural and metabolic changes in bone. *Animals*, 12(15):1946, 2022.

[32] Rho J. et al. Mechanical properties and the hierarchical structure of bone. *Medical Engineering & Physics*, 20(2):92–102, 1998.

[33] Fan Z. et al. Three-dimensional finite element analysis of the effects of anisotropy on bone mechanical properties measured by nanoindentation. *Journal of Materials Research*, 19(1), 2004.

[34] Ruffoni D. GBIO0012-2 – Lectures. 2022.

[35] Dreamstime. *Collagen molecule. Structure of a collagen fibers. amino acids bound together to form a triple helix of elongated fibril* `https://www.dreamstime.com/collagen-molecule-structure-fibers-amino-acids-bound-together-to-for` *Consulted on 11th April 2024.*

[36] Blumer M. J. F. Bone tissue and histological and molecular events during development of the long bones. *Annals of Anatomy*, 235:151704, 2021.

[37] Cowin S. C. and Doty S. B. *Tissue mechanics*. Springer, 2007.

[38] Chang B. and Liu X. Osteon: Structure, turnover, and regeneration. *Tissue Engineering Part B: Reviews*, 28(2):261–278, 2022.

[39] Rho J. et al. Elastic properties of human cortical and trabecular lamellar bone measured by nanoindentation. *Biomaterials*, 18(20):1325–1330, 1997.

[40] Van Oers R. F. M. et al. A unified theory for osteonal and hemi-osteonal remodeling. *Bone*, 42(2):250–259, 2008.

[41] Van Oers R. F. M. et al. Relating osteon diameter to strain. *Bone*, 43(3):476–482, 2008.

[42] Parfitt A. M. Targeted and nontargeted bone remodeling: relationship to basic multicellular unit origination and progression. *Bone*, 30(12002):5–7, 2002.

[43] Lucas G. L. et al. *A Primer of Biomechanics*. Springer Science Business Media, 2011.

[44] Dong X. N. and Guo X. E. The dependence of transversely isotropic elasticity of human femoral cortical bone on porosity. *Journal of Biomechanics*, 37(8):1281–1287, 2004.

[45] Lassen N. E. et al. Coupling of bone resorption and formation in real time: New knowledge gained from human haversian bmus. *Journal of Bone and Mineral Research*, 32(7):1395–1405, 2017.

[46] Lamarche B. A. et al. 2D size of trabecular bone structure units (BSU) correlate more strongly with 3D architectural parameters than age in human vertebrae. *Bone*, 160:116399, 2022.

[47] Giner E. et al. Calculation of the critical energy release rate $G_c$ of the cement line in cortical bone combining experimental tests and finite element models. *Engineering Fracture Mechanics*, 184:168–182, 2017.

[48] Burr D. B. et al. Composition of the cement line and its possible mechanical role as a local interface in human compact bone. *Journal of Biomechanics*, 22(11):939–941, 1988.

[49] Qiu S. et al. The morphological association between microcracks and osteocyte lacunae in human cortical bone. *Bone*, 37(1):10–15, 2005.

[50] Nobakhti S. et al. Cement lines and interlamellar areas in compact bone as strain amplifiers – contributors to elasticity, fracture toughness and mechanotransduction. *Journal of the Mechanical Behavior of Biomedical Materials*, 29:235–251, 2014.

[51] Shahar R. and Weiner S. Open questions on the 3d structures of collagen containing vertebrate mineralized tissues: A perspective. *Journal of Structural Biology*, 201(3):187–198, 2018.

[52] Kastner M. J. et al. Elastic modulus mapping for bovine cortical bone from submillimeter- to submicron-scales using peakforce tapping atomic force microscopy. *Extreme Mechanics Letters*, 41:101031, 2020.

[53] Montalbano T. and Feng G. Nanoindentation characterization of the cement lines in ovine and bovine femurs. *Journal of Materials Research*, 26(8):1036–1041, 2011.

[54] Cantamessa A. et al. Abstract mineralization and mechanical insights of cement lines in human osteonal bone. *21st National Day of Biomedical Engineering 2023 Annual Meeting of the IEEE-EMBS Benelux Chapter*, 2023.

[55] Oliver W. C. and Pharr G. M. Nanoindentation in materials research: Past, present, and future. *MRS Bulletin*, 35(11):897–907, 2010.

[56] Armitage O. E. and Oyen M. L. Indentation across interfaces between stiff and compliant tissues. *Acta Biomaterialia*, 56:36–43, 2017.

[57] Cui L. et al. Effects of bone specimen internal defect on nanoindentation results: An investigation by finite element analysis. *Journal of Computational and Theoretical Nanoscience*, 12(10):3572–3577, 2015.

[58] Carnelli D. et al. A finite element model for direction-dependent mechanical response to nanoindentation of cortical bone allowing for anisotropic post-yield behavior of the tissue. *Journal of Biomechanical Engineering*, 132(8):081008, 2010.

[59] Pathak S. and Kalidindi S. R. Spherical nanoindentation stress–strain curves. *Materials Science and Engineering: R: Reports*, 91:1–36, 2015.

[60] Jonhson K. L. *Contact Mechanics*. Cambridge University Press, 1985.

[61] Tits A. A multimodal correlative investigation of the tendon-bone interface. PhD Thesis. University of Liège, 2023.

[62] Zlotnikov I. et al. In situ elastic modulus measurements of ultrathin protein-rich organic layers in biosilica: towards deeper understanding of superior resistance to fracture of biocomposites. *RSC Advances*, 3(17):5798, 2013.

[63] Guo W. On the influence of indenter tip geometry on the identification of material parameters in indentation testing. PhD Thesis. University of Liège, 2011.

[64] Antoon Paar. `https://www.anton-paar.com/fr-fr/produits/details/hit-300/` Consulted on 7th Mai 2024.

[65] Sakharova N. A. et al. Comparison between berkovich, vickers and conical indentation tests: A three-dimensional numerical simulation study. *International Journal of Solids and Structures*, 46(5):1095–1104, 2009.

[66] Sagadevan S. and Murugasen P. Novel analysis on the influence of tip radius and shape of the nanoindenter on the hardness of materials. *Procedia Materials Science*, 6:1871–1878, 2014.

[67] Fischer-Cripps A. C. *Nanoindentation*. New York: Springer, 2 edition, 2004.

[68] Ang S. et al. Determination of the elastic/plastic transition of human enamel by nanoindentation. *Dental Materials*, 25(11):1403–1410, 2009.

[69] O'Connor J. et al. Computational modeling of viscoplastic polymeric material response during micro-indentation tests. *Journal of the Brazilian Society of Mechanical Sciences and Engineering*, 42(8):438, 2020.

[70] Remache D. et al. Application of the Johnson-Cook plasticity model in the finite element simulations of the nanoindentation of the cortical bone. *Journal of the Mechanical Behavior of Biomedical Materials*, 101:1751–6161, 2020.

[71] Harding J. W. and Sneddon I. N. The elastic stresses produced by the indentation of the plane surface of a semi-infinite elastic solid by a rigid punch. *Mathematical Proceedings of the Cambridge Philosophical Society*, 41(1):16–26, 1945.

[72] Oliver W. C. and Pharr G. M. Measurement of hardness and elastic modulus by instrumented indentation: Advances in understanding and refinements to methodology. *Journal of Materials Research*, 19(1), 2004.

[73] Chen C. 2-D finite element modeling for nanoindentation and fracture stress analysis Master Thesis. University of south florida, 2009.

[74] Williams J. A. and Dwyer-Joyce R. S. Contact between solid surfaces. *Modern Tribology Handbook: Principles of Tribology*, 1:121–162, 2000.

[75] Zlotnikov I. et al. Mapping nanomechanical properties near internal interfaces in biological materials. *MRS Proceedings*, 1345, 2011.

[76] Hertz H. *On the contact of rigid elastic solids and on hardness.* Macmillan, 1896.

[77] Hertz H. On the contact of elastic solids. *Journal fur die reine und angewandte Mathematik*, 92:156–171, 1881.

[78] Popov V. L. *Contact Mechanics and Friction.* Springer Berlin Heidelberg, 2017.

[79] Shelef Y. and Bar on B. Interfacial indentations in biological composites. *Journal of the Mechanical Behavior of Biomedical Materials*, 114:1751–6161,, 2021.

[80] Carnelli D. et al. Nanoindentation testing and finite element simulations of cortical bone allowing for anisotropic elastic and inelastic mechanical response. 44(10):1852–1858, 2011.

[81] Learning Forum Ansys. *https://forum.ansys.com/forums/topic/ is-my-understanding-of-substeps-correct/* Consulted on 18th May 2024.

[82] Navin Baskar. *https://skill-lync.com/blogs/technical-blogs/ design-what-are-analysis-settings-in-ansys* Consulted on 11th May 2024.

[83] ANSYS. Lecture 2 - ANSYS Mechanical - Introduction to Structural Nonlinearities. 2013.

[84] ANSYS. Lecture 3 - ANSYS Mechanical - Introduction to Structural Nonlinearities. 2013.

[85] ANSYS. Lectures - Numerical Modeling of Contact – How is contact modeled? What are advantages and disadvantages different formulation? - Solid Mechanics II – Capturing Complex Response. 2020.

[86] González Merino A. et al. Sources of uncertainty in the seismic design of submerged free-standing racks. *Energy Procedia*, 127:310–319, 2017.

[87] Bressan J. D. et al. Modeling of nanoindentation of bulk and thin film by finite element method. *Wear*, 258(1-4):115–122, 2005.

[88] Hajali R. et al. Nonlinear constitutive models from nanoindentation tests using artificial neural networks. *International Journal of Plasticity*, 24(3):371–396, 2008.

[89] Gukop N. S. et al. Analysis of indentation test using solid works simulation. *Emerging Advances in Integrated Technology*, 1(1), 2020.

## Bibliography

[90] ÖZGÜN. *https://www.mechead.com/what-is-large-deflection-in-ansys Consulted on 11th May 2024.*

[91] ANSYS 2023 R2. Mechanical User's Guide ANSYS Inc. 2023.

[92] Meyers M. A. and Chawla K. K. *Mechanical Behavior of Materials*. Cambridge University Press, 2 edition, 2009.

[93] Xue H. et al. Approach for obtaining material mechanical properties in local region of structure based on accurate analysis of micro-indentation test. *Chinese Journal of Mechanical Engineering*, 34(1):130, 2021.

[94] Liang K. et al. The study on the substrate effect in the nanoindentation experiment of the hybrid material. *Advances in Civil Engineering*, pages 1–11, 2022.

[95] Elakkad A. et al. A mixed finite element method for elasticity problem. *International Journal of Advanced Computer Science and Applications*, 4(2), 2013.

[96] Reddy J. *An Introduction to the Finite Element Method*. McGraw-Hill Education, 2 edition, 1993.

[97] Cantamessa A. et al. Abstract 28th congress of european society of biomechanics. 2023.

[98] Zysset P. K. et al. Elastic modulus and hardness of cortical and trabecular bone lamellae measured by nanoindentation in the human femur. *Journal of Biomechanics*, 32(10):1005–1012, 1999.

[99] Faingold A. et al. Nanoindentation of osteonal bone lamellae. *Journal of the Mechanical Behavior of Biomedical Materials*, 9:198–206, 2012.

[100] Mani A. Z. et al. Molecular dynamics simulation of indentation on nanocoated surfaces: A comparison between 3d and 2d plane strain models. *Journal of Materials Research*, 36(15):3063–3073, 2021.

[101] Sankar B.V. and Sun C.T. Indentation of a beam by a rigid cylinder. *International Journal of Solids and Structures*, 19(4):293–303, 1983.

[102] Xu B.X. et al. Finite element analysis of the indentation stress characteristics of the thin film/substrate systems by flat cylindrical indenters. *Materials Science & Engineering Technology*, 37(8):681–686, 2006.

[103] Lu Y.C. et al. Finite element analysis of cylindrical indentation for determining plastic properties of materials in small volumes. *Journal of Physics D: Applied Physics*, 41(11):115415, 2008.

[104] Cantamessa A. et al. Abstract mineralization and mechanical insights of cement lines in human osteonal bone. *Abstract Annual Meeting of the American Society of Bone and Mineral Research*, 2023.

[105] Mullins L. P. et al. Calibration of a constitutive model for the post-yield behaviour of cortical bone. *Journal of the Mechanical Behavior of Biomedical Materials*, 2(5):460–470, 2009.

[106] Tai K. et al. Effect of mineral content on the nanoindentation properties and nanoscale deformation mechanisms of bovine tibial cortical bone. *Journal of Materials Science: Materials in Medicine*, 16(10):947–959, 2005.

[107] Paietta R. C. et al. Influences of spherical tip radius, contact depth, and contact area on nanoindentation properties of bone. *Journal of Biomechanics*, 44(2):285–290, 2011.

[108] Bekker A. et al. Introducing objective power law rate dependence into a visco-elastic material model of bovine cortical bone. *International Journal of Impact Engineering*, 66:28–36, 2014.

[109] Zhang J. et al. Mechanical property determination of bone through nano- and micro-indentation testing and finite element simulation. *Journal of Biomechanics*, 41(2):267–275, 2008.

[110] Olesiak S. E. et al. Viscous-elastic-plastic behavior of bone using berkovich nanoindentation. *Mechanics of Time-Dependent Materials*, 14(2):111–124, 2010.

[111] Adam C. J. and Swain M. V. The effect of friction on indenter force and pile-up in numerical simulations of bone nanoindentation. *Journal of the Mechanical Behavior of Biomedical Materials*, 4(7):1554–1558, 2011.

[112] Cantamessa A. et al. Abstract cement lines material properties and interplay with the lacun-canalicular network in human osteonal bone. *Abstract 29th Congress of the European Society of Biomechanics*, 2024.

[113] Kerschnitzki M. et al. The organization of the osteocyte network mirrors the extracellular matrix orientation in bone. *Journal of Structural Biology*, 173(2):303–311, 2011.